Oil & Natural Gas Technology

DOE Award No.: DE-FC26-04NT15535

Final Report

Improvement of Sweep Efficiency in Gasflooding

Submitted by:
Kishore K. Mohanty
University of Houston
4800 Calhoun Road
Houston, TX 77204-4004

Office of Fossil Energy

Disclaimer

This report was prepared as an account of work sponsored by an agency of the United States Government. Neither the United States Government nor any agency thereof, nor any of their employees, makes any warranty, express or implied, or assumes any legal liability or responsibility for the accuracy, completeness, or usefulness of any information, apparatus, or process disclosed, or represents that its use would not infringe privately owned rights. Reference herein to any specific commercial product, process, or service by trade name, trademark, manufacturer, or otherwise does not necessarily constitute or imply its endorsement, recommendation, or favoring by the United States Government or any agency thereof. The views and opinions of authors expressed herein do not necessarily state or reflect those of the United States Government or any agency thereof.

Abstract

Miscible and near-miscible gasflooding has proven to be one of the few cost effective enhance oil recovery techniques in the past twenty years. As the scope of gas flooding is being expanded to medium viscosity oils in shallow sands in Alaska and shallower reservoirs in the lower 48, there are questions about sweep efficiency in near-miscible regions. The goal of this research is to evaluate sweep efficiency of various gas flooding processes in a laboratory model and develop numerical tools to estimate their effectiveness in the field-scale. Quarter 5-spot experiments were conducted at reservoir pressure to evaluate the sweep efficiency of gas, WAG and foam floods. The quarter 5-spot model was used to model vapor extraction (VAPEX) experiments at the lab scale. A streamline-based compositional simulator and a commercial simulator (GEM) were used to model laboratory scale miscible floods and field-scale pattern floods.

An equimolar mixture of NGL and lean gas is multicontact miscible with oil A at 1500 psi; ethane is a multicontact miscible solvent for oil B at pressures higher than 607 psi. WAG improves the microscopic displacement efficiency over continuous gas injection followed by waterflood in corefloods. WAG improves the oil recovery in the quarter 5-spot over the continuous gas injection followed by waterflood. As the WAG ratio increases from 1:2 to 2:1, the sweep efficiency in the 5-spot increases, from 39.6% to 65.9%. A decrease in the solvent amount lowers the oil recovery in WAG floods, but significantly higher amount of oil can be recovered with just 0.1 PV solvent injection over just waterflood. Use of a horizontal production well lowers the oil recovery over the vertical production well during WAG injection phase in this homogeneous 5-spot model. Estimated sweep efficiency decreases from 61.5% to 50.5%. In foam floods, as surfactant

3

to gas slug size ratio increases from 1:10 to 1:1, oil recovery increases. In continuous gasflood VAPEX processes, as the distance between the injection well and production well decreases, the oil recovery and rate decreases in continuous gasflood VAPEX processes. Gravity override is observed for gas injection simulations in vertical (X-Z) cross-sections and 3-D quarter five spot patterns. Breakthrough recovery efficiency increases with the viscous-to-gravity ratio in the range of 1-100. The speed up for the streamline calculations alone is almost linear with the number of processors. The overall speed up factor is sub-linear because of the overhead time spent on the finite-difference calculation, inter-processor communication, and non-uniform processor load. Field-scale pattern simulations showed that recovery from gas and WAG floods depends on the vertical position of high permeability regions and k_v/k_h ratio. As the location of high permeability region moves down and k_v/k_h ratio decreases, oil recovery increases. There is less gravity override. The recovery from the field model is lower than that from the lab 5-spot model, but the effect of WAG ratio is similar.

TABLE OF CONTENTS

Page

Executive Summary

Miscible and near-miscible gasflooding has proven to be one of the few cost effective enhance oil recovery techniques in the past twenty years. As the scope of gas flooding is being expanded to medium viscosity oils in shallow sands in Alaska and shallower reservoirs in the lower 48, there are questions about sweep efficiency in near-miscible regions. The goal of this research is to evaluate sweep efficiency of various gas flooding processes in a laboratory model and develop numerical tools to estimate their effectiveness in the field-scale. Quarter 5-spot experiments were conducted at reservoir pressure to evaluate the sweep efficiency of gas, WAG and foam floods. The quarter 5-spot model was used to model vapor extraction (VAPEX) experiments at the lab scale. A streamline-based compositional simulator and a commercial simulator (GEM) were used to model laboratory scale miscible floods and field-scale pattern floods.

An equimolar mixture of NGL and lean gas is multicontact miscible with oil A at 1500 psi; ethane is a multicontact miscible solvent for oil B at pressures higher than 607 psi. WAG improves the microscopic displacement efficiency over continuous gas injection followed by waterflood in corefloods. WAG improves the oil recovery in the quarter 5-spot over the continuous gas injection followed by waterflood. As the WAG ratio increases from 1:2 to 2:1, the sweep efficiency in the 5-spot increases, from 39.6% to 65.9%. A decrease in the solvent amount lowers the oil recovery in WAG floods, but significantly higher amount of oil can be recovered with just 0.1 PV solvent injection over just waterflood. Use of a horizontal production well lowers the oil recovery over the vertical production well during WAG injection phase in this homogeneous 5-spot model. Estimated sweep efficiency decreases from 61.5% to 50.5%. In foam floods, as surfactant

to gas slug size ratio increases from 1:10 to 1:1, oil recovery increases. In continuous gasflood VAPEX processes, as the distance between the injection well and production well decreases, the oil recovery and rate decreases in continuous gasflood VAPEX processes. Gravity override is observed for gas injection simulations in vertical (X-Z) cross-sections and 3-D quarter five spot patterns. Breakthrough recovery efficiency increases with the viscous-to-gravity ratio in the range of 1-100. The speed up for the streamline calculations alone is almost linear with the number of processors. The overall speed up factor is sub-linear because of the overhead time spent on the finite-difference calculation, inter-processor communication, and non-uniform processor load. Field-scale pattern simulations showed that recovery from gas and WAG floods depends on the vertical position of high permeability regions and k_v/k_h ratio. As the location of high permeability region moves down and k_v/k_h ratio decreases, oil recovery increases. There is less gravity override. The recovery from the field model is lower than that from the lab 5-spot model, but the effect of WAG ratio is similar.

Introduction

Miscible gas flooding has been proven to be a cost-effective enhanced oil recovery technique. There are about 80 gasflooding projects (CO_2, flue gas and hydrocarbon gas) in US and about 300,000 b/d is produced from gas flooding, mostly from light oil reservoirs.[1] The recovery efficiency (10-20% OOIP) and solvent utilization (3-12 MCF/bbl) need to be improved. The application of miscible and immiscible gas flooding needs to be extended to medium viscosity reservoirs.

McGuire et al.[2] have proposed an immiscible water-alternating-gas flooding process, called VR-WAG (viscosity reduction water alternating gas) for North Slope medium visocisty oils. Many of these oils are depleted in their light end hydrocarbons C7-C13. When a mixture of methane and NGL (natural gas liquid) is injected, the C2+ components condense into the oil and decrease the viscosity of oil making it easier for the water to displace the oil. From reservoir simulation, this process is estimated to enhance oil recovery over waterflood from 19% to 22% of the OOIP, which still leaves behind nearly 78% of the OOIP. Thus further research should be directed at improving the recovery efficiency of these processes for viscous oil reservoirs.

Recovery efficiency depends on microscopic displacement efficiency and sweep efficiency. Microscopic displacement efficiency depends on pressure, [3,4] composition of the solvent and oil[5,6] and small (core) scale heterogeneity.[7,8] Sweep efficiency of a miscible flood depends on mobility ratio,[9-12] viscous-to-gravity ratio,[13-15] transverse Peclet number, [16] well configuration, and reservoir heterogeneity,[17-18] in general. The effect of reservoir heterogeneity is difficult to study at the laboratory-scale and is addressed mostly by simulation.[19-20] Most of the laboratory sweep efficiency studies[9,10,20,21] have been conducted with first-contact fluids or immiscible fluids at

ambient pressure / temperature and may not be able to respresent the displacement physics of multicontact fluids at reservoir conditions.

In fact, there are four proposed methods for sweep improvement in gas flooding: water-alternating-gas,[22] foams,[23] direct thickeners,[24] and dynamic profile control in wells.[25] To evaluate any sweep improvement methods, one needs controlled field-testing. Field-tests are expensive and not very controlled; two different tests cannot be performed starting with identical initial states and thus results are often inconclusive. Field-scale modeling of compositionally complex processes can be unreliable due to inadequate representation of heterogeneity and process complexity in existing numerical simulators. There is a need to conduct laboratory sweep efficiency studies with the multicontact miscible fluids at reservoir conditions to evaluate various sweep improvement techniques. Reservoir condition laboratory tests can be used to calibrate numerical simulators and evaluate qualitative changes in sweep efficiency. We have built a high-pressure quarter five-spot model where reservoir condition multicontact WAG floods can be conducted and evaluated.[26] The purpose of this work is to evaluate sweep efficiency of various miscible flooding processes in a laboratory model, develop numerical tools to estimate sweep efficiency in the field-scale and identify solvent composition, mobility control method and well architecture that improve sweep efficiency. The three tasks for the project are: (1) Solvent composition, (2) Sweep efficiency, and (3) Numerical model. The experimental and computational methods are described next followed by results and discussions.

Experimental Methods

Oil

Two crude oils are used in this work: Oil A and Oil B. Oil A was prepared in our laboratory by adding methane to a dead reservoir oil for a live oil viscosity of about 50 cp. It was used for corefloods. Oil B was a dead reservoir oil of viscosity 78 cp. This oil is used for slim tube and 5-spot studies because of unavailability of oil A. The two reservoirs are close to each other.

Component	Mol %
CO2	6.09
C1	38.29
C2	3.12
C3	3.76
C4	22.24
C5	12.88
C6	3.10
C7	3.10
C8	3.71
C10	3.71

Table 1 – Composition of solvent 1

Solvent

Two solvents were used in this work. Solvent 1 was prepared in such a way that its composition is the same as an equimolar mixture of an NGL (natural gas liquid) and a lean gas (LG). The composition of the solvent is shown in Table 1. It is multicontact miscible with oil A at the reservoir pressure and temperature from a previous study. Solvent 2 was pure ethane. It is multicontact miscible with oil B at the operating conditions of the 5-spot experiments.

Slim Tube

A slim tube, 20 feet long (609.6 cm) and 3/8 in OD, is packed with 20-100 mesh Ottawa sand and coiled to a circular shape of about 2 feet in diameter. The characteristics of the slim tube are listed in Table 2.

Slim Tube			
D (cm)	0.704	A (cm^2)	0.389
L (cm)	609.6	V (cm^3)	237.01
K (d)	25.0	V$_p$ (cm^3)	77.30
		ϕ	32.61

Table 2 - Characteristics of slim tube

0: Pumping Liquid
1: Oil
2: Solvent
3: 3-Way Valve
4: Slim Tube
5: Pressure Regulator
6: Collecting Tube
7: Pressure Transducer
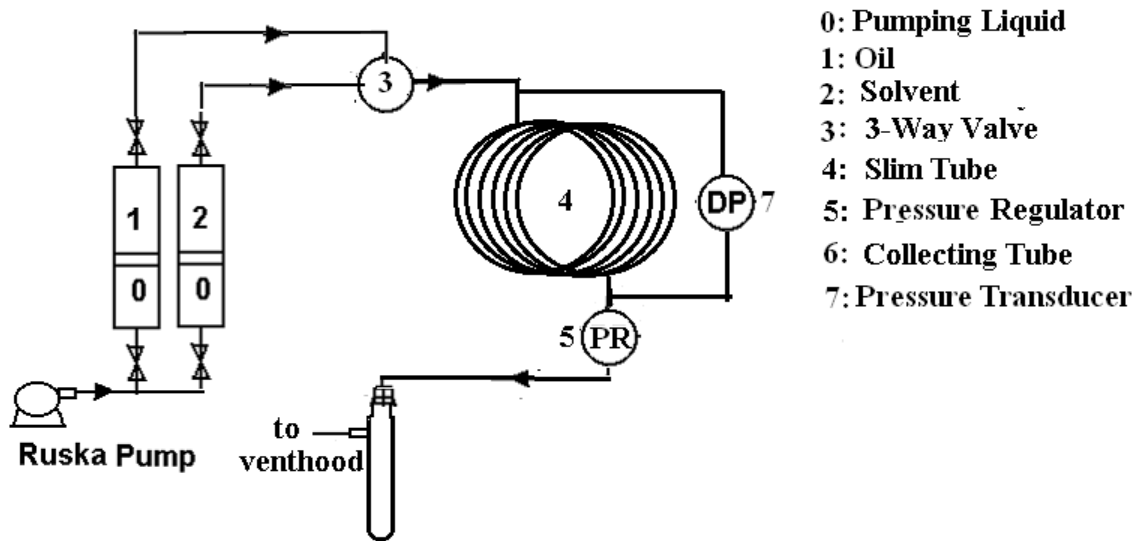
Fig. 1 - Flow loop for slim tube experiments

Fig. 1 shows the schematic diagram of the slim tube flow loop. A Ruska pump injects an oil into one of the two transfer cylinders. The transfer cylinder contains fluids to be injected to the slim tube, e.g., reservoir oil or miscible injectant. The back pressure regulator downstream of the slim tube controls the working pressure in the slim tube. The slim tube (after any previous run) is washed with at least 3 pore volumes of toluene.

11

High-pressure air and the nitrogen are used to flush out most of the toluene from the slim tube. The slim tube is put under vacuum for about 5 hours to evaporate the remaining toluene. The slim tube after cleaning is injected with more than 2 pore volumes of reservoir oil before adjusting the flow rate to 4.51 mL/hr. The flow is allowed to reach steady state after half a day of continuous pumping at the same rate. The outlet oil is collected using an auto sampler. The cumulative volume of effluent oil and pressure drop are monitored throughout the solvent injection.

Core Floods

A Berea core is used to perform linear gas and WAG floods. The core has a porosity of about 18% and a permeability of about 116 mD. The core properties are shown in Table 3.

Core				
	D (cm)	5.050	A (cm^2)	20.03
	L (cm)	25.100	V (cm^3)	502.74
N2	K (md)	386.59	V$_p$ (cm^3)	91.00
Brine	K (md)	116.34	ϕ	18.10

Table 3 – Properties of the Berea core.

The Berea core had a residual water saturation of 28.6%. It is flooded with a reservoir oil at a constant flow rate of 0.15 mL/min until reaching steady state. The gaseous solvent or water-alternating gas slugs were then injected into the core at the same rate. Pressure drop and effluent composition were monitored. The experimental apparatus is shown in **Fig. 2**.
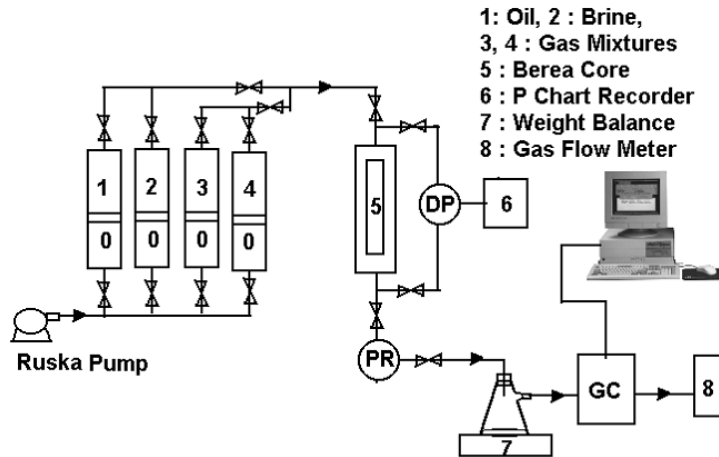
Fig. 2 – Experimental apparatus used in WAG floods

Quarter 5-Spot Model. The quarter 5-spot high-pressure cell consists of three stainless steel circular plates put together by several bolts. **Fig. 3** shows the front view of the 5-spot high-pressure cell. The top and bottom plates are identical. Each has a cut-in section for the overburden liquid. The middle plate has a cut-off section of 0.254m x 0.254m x 0.025m (10" x 10" x 1") at the center for the porous medium. Two circular sheets of rubber are used to sandwich the packing and prevent bypassing when liquid is flowing through the medium. The other side of the rubber faces the overburden liquid when the three plates are put together; an overburden pressure of > 17.232 MPa (2500 psi) is applied. The packing medium consisted of 58-149 micron (100-250 mesh) sand. Porosity and permeability were measured in separate tests by packing a steel tube with the same sand. The porosity is 30.5%; the oil permeability is about 5 darcy at the connate water saturation. It is assumed that vertical and horizontal permeability are approximately equal in this unconsolidated sand pack. Changes in porosity and permeability due to applied overburden pressure in the high-pressure cell are assumed to be small. Initial water saturation in the model after oil injection was determined by material balance.

13

Fig. 3 - Front view of the quarter 5-spot high-pressure cell

There are 12 ports in the model for various well configurations. There are 5 ports each on two opposite sides (A1-A5 and B1-B5) and two ports at the other two corners. For vertical well configuration, the solvent is injected at port A1 and the production is collected at port B1 while other ports are shut. For vertical injection and horizontal production wells, the fluid is injected at port A1 and the production is collected at ports B1 - B5. The maximum safe operating pressure for the porous section is about 13.790 MPa (2000 psi) while the overburden pressure is maintained at 17.237 MPa (2500 psi). The cell is connected to the flow loop shown in **Fig. 4**; part number 5 is the 5-spot model for WAG floods instead of a core.

14
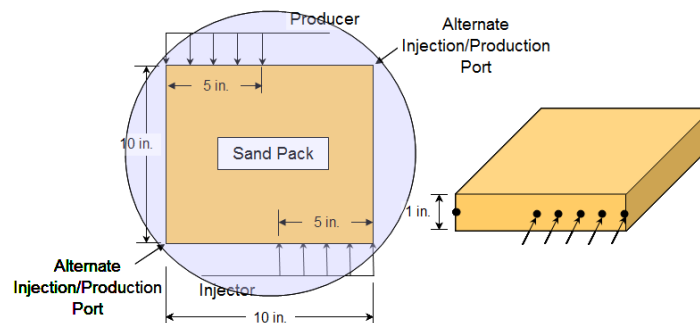
Fig. 4 – Quarter 5-spot cell used in WAG floods

The quarter 5-spot model was initially saturated with water and then oil was injected to displace the water. Positioning the cell vertically and injecting in various ports allowed for a stable displacement of water by the more viscous oil. The residual water saturation was determined to be ~9 % in this cell, by material balance. This was the intended initial condition for all floods.

Before each experiment, the quarter 5-spot model was flooded with oil to bring it back to the residual water saturation (of about 9%). All of the solvent dissolved in the oil was removed from the sand during the oil flood by tilting the cell into a vertical position and injecting several pore volumes of water into various ports, taking advantage of gravity stabilization and maintaining pressure with a BPR. This process removes the majority of the oil/solvent mixture. Then fresh oil, also at high pressure, was injected at the top to displace the water and dissolve the remaining oil and solvent. Between some experiments, the 5-spot model was depressurized and opened up. The sand was imaged and removed. The model was repacked and resaturated. The flow rate was maintained at 22.5 ml/hr during gas, water, and WAG floods. The BPR (back pressure regulator) pressure was kept constant during each experiment.

Inverse 9-spot pattern is often used with viscous oils, because it provides more production wells per pattern compared to a 5-spot pattern. A quarter of an inverse 9-spot pattern was created in our model by using all four corner wells. Solvent and water were injected in one corner and fluids were produced from the other three corners. The closer two wells are refered to here as the "side wells"; the opposite well is called the "diagonal well". Two separate BPR's were used to maintain constant pressure. One BPR controlled pressure for both side producers and the other BPR controlled the diagonal outlet

15

pressure. 0.5 PV of solvent is injected followed by 1.5 PV of water in this inverse 9-spot, just like the base case 5-spot model discussed above.

VAPEX Experiments

The vapor extraction (VAPEX) process has been proposed as a novel method to recover very viscous oil and bitumen. In essence VAPEX involves injection of hydrocarbon and/or CO_2 mixtures using horizontal well pairs situated vertically. Solvent diffusion into bitumen phase results in drastic viscosity reduction, allowing the otherwise immobile bitumen to flow by gravity forces into a horizontal producer well. Field tests have been limited to small pilot operations but extensive lab work has proven the process to be effective.

This study investigated the effectiveness of VAPEX on a medium viscosity dead oil (~78cP) using solvents that are only partially miscible at the operating pressure (~200 psi) and temperature (~77°F). Effect of spacing between the horizontal injector and producer wells, solvent composition, and flow rate on oil recovery rate and cumulative oil recovery were examined. Simulation of the experiments provided insight into the in-situ saturations, location of solvent/oil phase boundary and phase compositions.

A high pressure cell encasing a 10 in. x 10 in.x 1 in. sand pack was used in all VAPEX runs. The sand was an approximately even distribution of ~58-149 micron (100-250 mesh) Ottowa sand particles. Sand was wet packed with water by hand into the cell. Overburden pressure of 2500 psi was applied to the top and bottom faces of the pack. Gravity stable displacement of water by oil was done to estimate pore volume (500±10 cm^3) and porosity (30.5%). Separate 1D tests and supporting simulation showed that permeability to water was ~3.5 darcy and water residual to oil flood was ~9% PV (~45

16

cm^3) . It is assumed that the sand is mostly water wet although no wettability tests had been performed to confirm.

Controlling the well rates proved to be difficult at these conditions (200 psi, 77°F) using a BPR because of the large differences in oil and solvent density and viscosity. An ISCO model 500D syringe pump was used to pump a lubricating fluid (Soltrol-130) into a TEMCO piston accumulator. The piston pressurizes the solvent (C1, C2, or mixture of the two) previously charged to the accumulator and delivers it to the inlet port of the high pressure cell. Fluid was collected from a production port at the bottom of the cell and directed through either a TEMCO model BPR-50-1 back pressure regulator of a steel cylinder used for separation and collection of oil and gas. Using the BPR for upstream pressure maintenance resulted in frequent depressurization of the cell and the solvent source cylinder. When the collection cylinder was used, an ISCO 500D syringe pump maintained the pressure inside the cylinder at 200 psi. This allowed for a partial PID control of the pressure and greatly improved management of the outlet flow. A Mettler balance was used to estimate the mass of fluid collected. In order to estimate the produced oil volume, an average oil density (measured after the experiment) was assumed and mass was divided by this value. Small errors are introduced if produced oil density is not constant, but numerical simulation results show that oil density should not change drastically and error in produced oil volume estimation is expected to be within the experimental error.

Each experiment began by first injecting oil into the cell at the prescribed constant volumetric flow rate of the experiment (25 cc/h for most expts.) and maintaining the upstream pressure with the TEMCO BPR-50-1. This was accomplished by using an ISCO 500D pump to pump Soltrol-130 into a TEMCO piston accumulator containing the dead

oil. Because the oil is single phase, the BPR could maintain the pressure. Solvent was charged to another TEMCO piston accumulator and a separate ISCO 500D pump delivered Soltrol-130 to that accumulator. Once a steady pressure drop was established during oil injection, the pressure at the inlet was matched to that of the solvent cylinder as closely as possible. A three-way valve was used to switch immediately to solvent injection without stopping flow.

Foam Flooding Experiments

Foam flooding experiments were conducted in a 1-D sand pack first before doing it in quarter 5-spot model. The 1-D sand pack consisted of a steel tube of dimensions 1.71 cm I.D. and 91.44 cm long. The sand we used for packing this tube has mesh size ranging from 50 to 200. The pore volume was measured to be 73 cm^3. The porosity is 34.76 %.

The surfactant we used to create foam is Bioterge AS 40. The purpose of our work is to generate foam inside the sand pack by injecting surfactant alternate gas. Depending on the slug size and the velocity of gas and surfactant solution (1% Bioterge), the quality of foam can be weak or strong. Strong foam helps to control the mobility of gas while travelling in porous media. We carried several experiments to test the quality of foam in the sand pack. In these experiments, the 1-D sand pack tube was in horizontal orientation. The absolute permeability of the sand pack tube was measured to be 9.75 darcy with water. The separation cylinder and back pressure regulators were removed from the outlet port for easy observation.

In the foam flooding of the quarter 5-spot, the 1-D sand pack and a visual cell were placed before the inlet of the 5-spot in most experiments. The 5-spot was first filled with brine and driven to connate water by oil injection. Then slugs of solvent (ethane) and surfactant solution were injected at 22 ml/hr with a back pressure of 1350 psi. In these

experiments, the foam was generated in the sand pack and injected into the 5-spot. In a few experiments, the sand pack and the visual cell were not used; in such cases the foam was generated inside the 5-spot model itself. The results of these experiments can be compared with the WAG experiments conducted earlier.

<div align="center">**Computational Methods**</div>

Streamline Methodology

In this work, a compositional streamline module is developed and integrated with a finite-difference simulator. The streamline methodology is based on an IMPES formulation where pressure is solved implicitly and compositions/saturations are updated using an explicit method. The pressure equation is solved on the finite-difference grid. The velocity field is generated from the pressure field using Darcy's law as given by the equation,

$$u_j = -\frac{\vec{\vec{K}} k_{rj}}{\mu_j} \cdot \left(\nabla P_j + \rho_j g \nabla D \right) \quad . \tag{1}$$

Once the velocity field is generated, streamlines are traced based on the total velocity field. Streamlines are traced by using the analytical Pollock method[27]. The underlying assumption is that velocity changes linearly in each grid block in each coordinate direction. Streamlines are traced from injectors to producers and streamline path intersects with the underlying finite difference cells. These intersection points are the streamline nodes and time of flight information is recorded for each streamline point for all the streamlines in the simulation domain. Note,

$$\tau(s) = \int_0^s \frac{\phi(x)}{|u_t(x)|} dx, \tag{2}$$

where τ is the time of flight, and u_t is the total velocity.

Information is mapped from the original finite-difference grid to the streamline grid Three-dimensional material balance equation in the finite difference form is transformed *approximately* to one dimensional equation along the streamline coordinates

in terms of time of flight. Decoupling of flow from the underlying finite difference grid allows us to take large time steps while updating compositions along the streamlines. Fluxes are calculated for all the components and concentrations are updated along each streamline using a 1-D solver. Flux estimation at the streamline nodes is the most time consuming task due to repeated flash calculation procedures that are performed to determine the component distribution in hydrocarbon phases. The combination of accelerated successive substitution (ACSS) method with the Gibbs-free-energy minimization method is used for flash calculations.[28] Steps involved in computing fluxes at each local time step of simulation are described in Fig. 5. Flash is performed and phase densities and saturations are computed using updated values of phase mole fractions. Hydrocarbon phase viscosity is estimated using Lohrenz correlation.[29] Relative permeability and fractional flow of each phase is calculated based on the updated phase saturation and viscosity. We have also incorporated a four-phase (three hydrocarbon phases and water) relative permeability model[30] to handle four phase flow. Component fluxes are evaluated using updated values of phase densities, fractional flows, and mole fractions. Overall compositions are updated along the streamlines and this procedure is repeated for every local time step of simulation.

Flash Calculations

Update Phase Densities

Update Phase Saturations

Update Phase Viscosities

Calculate New Relative Permeability

Estimate Fractional Flow

Evaluate Component Fluxes

Update Compositions (1-D Solver)
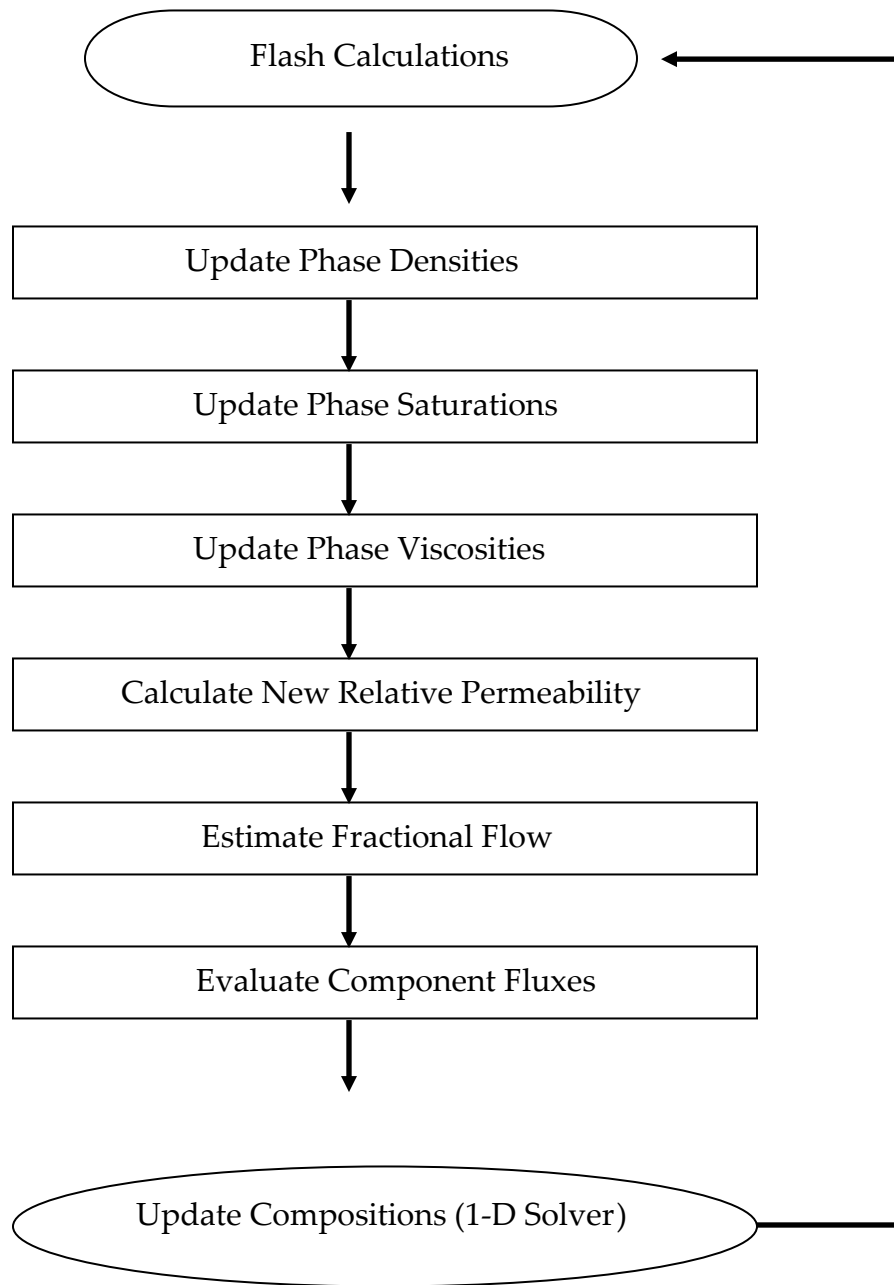
Fig. 5 - Procedure to estimate component fluxes at the streamline points

All the updated information is mapped back to the underlying finite difference grid. Saturations are calculated in the finite difference grid before the pressure field is updated. Based on the new pressure field, streamlines are recalculated. The transverse flux terms due to changing streamlines and transverse dispersion etc. can be incorporated in the future by operator splitting methods.

Mathematical Streamline Formulation

The mass balance equation for the multiphase fluid flow for a multi-component system can be written as

$$\phi \frac{\partial}{\partial t}\left[\sum_{j=1}^{n_p} x_{ij}\rho_j S_j\right] + \nabla\left[\sum_{j=1}^{n_p} x_{ij}\rho_j u_j\right] = 0 \ , \qquad i=1,n_c \tag{3}$$

where x_{ij} is the mole fraction of component i in phase j, ρ_j is the density of phase j, S_j is the saturation of phase j, ϕ is the porosity, and u_j is the darcy velocity given by Eq. (1). This equation can be written in terms of total velocity, mole fraction, molar densities, component concentrations, and fluxes, i.e.,

$$\phi \frac{\partial C_i}{\partial t} + \vec{u}_t . \nabla F_i \approx 0 \qquad , \tag{4}$$

where C_i and F_i are overall composition and fluxes of component i.

$$C_i = \sum_{j=1}^{n_p} x_{ij}\rho_j S_j \qquad , \tag{5}$$

$$F_i = \sum_{j=1}^{n_p} x_{ij} f_j \rho_j \qquad . \tag{6}$$

f_j is the fractional flow of phase j given by

$$f_j = \frac{k_{rj}/\mu_j}{\sum_{k=1}^{n_p} k_{rk}/\mu_k} \qquad , \tag{7}$$

where k_{rj} is the relative permeability of phase j, and μ_j is the viscosity of phase j. Eq. (4) is derived under the assumption of negligible capillary, diffusive, and gravity forces. Effect of these terms can be added by using operator splitting approximation, shown later.

Streamline Coordinates

Three-dimensional material balance Eq. (4) is transformed to streamline coordinates in terms of time of flight, $\tau(s)$. All the information regarding porosity, permeability, and mobility effects are incorporated in the time of flight coordinate along streamlines. Eq. (2) can be rewritten as

$$\vec{u}_t . \nabla = \phi \frac{\partial}{\partial \tau} \qquad . \tag{8}$$

Substituting Eq. (8) into Eq. (4) gives

$$\frac{\partial C_i}{\partial t} + \frac{\partial F_i}{\partial \tau} = 0 , \quad i = 1, n_c \qquad . \tag{9}$$

Eq. (9) is solved along the streamline and compositions are updated. A 1-D finite-difference compositional solver is developed to solve this transport equation along the streamlines. Different numerical schemes are incorporated to construct the numerical solution of Eq. (9). Implementation of higher order numerical schemes is described in a later section.

Inclusion of Gravitational Effect in Streamline Formulation

Gravity plays an important role in predicting the performance of field scale gas injection processes. Vertical sweep in gas injection processes is primarily governed by

heterogeneities and gravity segregation. Due to the density difference between the reservoir oil and the injected solvent (hydrocarbon gases, carbon dioxide, nitrogen, flue gases), gases have the tendency to rise up in the reservoir resulting in gravity override. This leads to the formation of a gravity tongue at the top of the reservoir which results in early breakthrough and low sweep. Therefore, it is imperative to account for the gravity effects in compositional simulations to accurately model gas floods in oil reservoirs.

Gravity override is governed by the ratio of gravity to viscous forces, called the gravity number, N_g. The relative magnitude of gravity and viscous forces in the reservoir is characterized by the time required to move the fluids in the vertical direction versus the time required to transport fluids in the horizontal direction. Gravity number is defined as

$$N_g = \frac{K_v \Delta \rho g L^2}{K_h (\Delta P_h) H} \qquad , \qquad (10)$$

where K_v is the vertical permeability, K_h is the horizontal permeability, $\Delta \rho$ is the density difference between the fluids, L is the distance between the wells, H is the reservoir thickness, and ΔP_h is the pressure drop in the horizontal direction. A rough guideline can be used to decide if the process is dominated by viscous forces or gravity forces as shown below:

$N_g < 0.1$ Viscous force dominated displacement

$0.1 < N_g < 10$ Transition zone between viscous and gravity dominated

$N_g > 10$ Gravity dominated displacement

The viscous-to-gravity ratio, R_{vg} is approximately the inverse of the gravity number (up to a constant). It is defined as

$$R_{vg} = \frac{2v\Delta\mu H}{\Delta\rho g K_v L} \qquad (11)$$

for constant injection rate processes[31] and is often correlated with gravity override.[5]

In compositional streamline simulation, streamline trajectories are traced on thebasis of the total velocity field which is seldom aligned with the gravity vector in gas floods. In general, phase velocities can have different directions (or vertical component) due to the density difference. Therefore, conventional streamline methods do not explicitly account for gravity while transporting fluids along the streamlines. One of the alternatives, as proposed by Blunt et al.,[32] is to trace phase specific streamlines. Another possibility is to incorporate gravity flux by using operator splitting approximation, as discussed by various authors.[33] Pressure field is solved in the finite difference grid using the finite difference simulator which itself incorporates gravity effects. Gravity term is added in the material balance equation by decomposing the flux term in the transport Eq. (9) to convective and gravity flux terms as discussed by Jessen et al.,[33] i.e.,

$$\frac{\partial C_i}{\partial t} + \frac{\partial F_i}{\partial \tau} + \frac{1}{\phi}\frac{\partial G_i}{\partial z} = 0 \qquad , \qquad (12)$$

$$G_i = K_v \sum_{j=1}^{n_p} x_{ij}\rho_j\lambda_j\left(\frac{\lambda_g}{\lambda_t} - g\rho_{mj}\right)\frac{\partial D}{\partial z} \quad , \qquad (13)$$

where G_i is the gravity flux of component i, λ_g and λ_t are the total mobility and total gravity mobility is given by

$$\lambda_t = \sum_{j=1}^{n_p}\frac{k_{rj}}{\mu_j} \qquad , \qquad (14)$$

$$\lambda_g = g\sum_{j=1}^{n_p}\lambda_j\rho_{mj} \qquad . \qquad (15)$$

26

Convective and gravity steps are treated independently for a global time step of the simulation. Convective step is performed by solving Eq. (9) along the streamlines for a global time step. Compositions are updated and mapped back to the underlying finite difference grid. Updated compositions now act as initial conditions for the gravity step which is performed in the finite difference grid. Gravity fluxes are computed in each grid block and the gravity step is performed to account for the gravity segregation according to:

$$\phi \frac{\partial C_i}{\partial t} + \frac{\partial G_i}{\partial z} = 0 \qquad . \qquad (16)$$

There are certain drawbacks associated with this method particularly in compositional simulations where flash calculations consume a large part of the CPU time. The stability of the gravity step limits the global time step size. Flash calculations are done in every gravity time step which reduces the computational efficiency of the simulation. Another shortcoming of this method is the path dependence of solution as explained by Jessen et al.[33] If the injected gas has a very high solubility in the oil, considerable portion of the gas will be dissolved while transporting fluids along the streamlines during the convective step. Small amount of the original gas will be left to segregate while performing the gravity time step of the simulation. This will lead to inaccurate prediction of displacement efficiency especially in miscible/near miscible problems. To overcome this problem, another method is implemented as proposed by Jessen et al. [33] to include the effect of gravity in compositional streamline simulation.

A pseudo immiscible approach is followed in which saturations are updated while performing the gravity step in the finite difference grid. After the convective time step, updated compositions are mapped back to the underlying finite difference grid. Phase

equilibrium calculations are performed and all the grid blocks are flashed to determine the new molar compositions, molar densities, and phase saturations. Relative permeabilities and densities of all the phases are estimated and gravity flux is computed. The pseudo immiscible gravity step is performed by solving the material balance equation in z direction given by

$$\phi \frac{\partial S_j}{\partial t} + \frac{\partial G}{\partial z} = 0 \qquad , \qquad (17)$$

where G is the gravity flux due to gas liquid segregation given by

$$G = \frac{K_{v,k+1}k_{rg,k+1}K_{v,k}k_{ro,k}(\rho_{mo} - \rho_{mg})g}{\mu_o K_{v,k+1}k_{rg,k+1} + \mu_g K_{v,k}k_{ro,k}} \qquad , \qquad (18)$$

where ρ_{mo} and ρ_{mg} are the mass densities of oil and gas phase respectively, and g is the acceleration due to gravity.

Small time steps are taken limited by the CFL constraint and saturations of all the phases are updated. After each little gravity time step, new gravity fluxes are computed based on new phase saturations, and relative permeabilites without performing any flash calculations. At the end of all gravity steps, overall compositions and mole fractions are evaluated in each grid block as follows

$$C_{i,k} = \sum_{j=1}^{n_p} x_{i,j,k}\rho_j S_j \qquad , \qquad (19)$$

where i is the component index, j is the phase index, and k is the grid block index. The advantage of this approach is that flash calculations are not needed at every local time step of gravity step. Flash is done only at the beginning of the gravity time step to compute phase properties.

Numerical Schemes

28

Several researchers have investigated the impact of numerical dispersion associated with the use of lower order schemes to construct numerical solution of transport equations in reservoir simulation. Single point upstream weighting is by far the most widely used scheme to approximate the numerical solution in black oil and compositional models. These lower order schemes suffer from excessive numerical dispersion which is unacceptable in miscible flow problems that are strongly coupled to the phase behavior. Truncation error introduced due to lower order approximations feeds into the phase behavior calculations and alters the composition path resulting in inaccurate solution. This numerical dispersion not only smoothes the shocks near displacement fronts but also results in unrealistic prediction of local displacement efficiency. To overcome these problems higher order schemes are developed to reduce the impact of numerical dispersion and improve the quality of solution. Straight forward use of higher order (two point upstream, midpoint) schemes in convection dominated hyperbolic equations results in spurious oscillations which is highly undesirable. In this section, we investigated different numerical schemes and demonstrated the application of higher order schemes. One dimensional solver is developed by incorporating different schemes to solve the transport Eq. (10) along streamlines. Single point upstream weighting scheme and different forms of higher order total variation diminishing (TVD) schemes are implemented to discretize the convection terms of multi component mass conservation equation.

Finite Difference Discretization

Finite difference form of Eq. (10) is given by

$$C_{i,k}{}^{n+1} = C_{i,k}{}^{n} + \frac{\Delta t}{\Delta \tau}\left[F_{i,k-1/2}{}^{n} - F_{i,k+1/2}{}^{n}\right] \quad , \tag{20}$$

where n is the time step level, k is the node counter of discretized streamline, i is the ith component. Fluxes are constructed at the cell faces (k+1/2) and (k-1/2) using different numerical approximations. Three different schemes are incorporated in the compositional streamline simulator to approximate the fluxes at the cell boundary.

Single Point Upstream Weighting

In the single point upstream weighting scheme the cell face flux is approximated by the flux value at the upstream point

$$F_{i,k+1/2} = F_{i,k} \ ,$$

$$F_{i,k-1/2} = F_{i,k-1}.$$

Eq. (19) reduces to

$$C_{i,k}{}^{n+1} = C_{i,k}{}^{n} + \frac{\Delta t}{\Delta \tau} \left[F_{i,k-1}{}^{n} - F_{i,k}{}^{n} \right] \ . \tag{21}$$

Total Variation Diminishing Scheme (Flux Limiting)

Spatially accurate TVD schemes are developed to eliminate spurious numerical oscillations while retaining higher order accuracy in the smooth regions. A finite difference TVD scheme is constructed in such a way that total variation of solution does not increase with time. If we define total variation in concentration as

$$TV(C^{n}) = \sum_{k=1}^{NS} \left| C_{k+1}{}^{n} - C_{k}{}^{n} \right| \ , \tag{22}$$

where *NS* is the number of points/nodes on any streamline. A scheme is said to be TVD if the total variation at a time step n+1 is less than or equal to the total variation at time n, i.e.,

$$TV(C^{n+1}) \leq TV(C^{n}) \ . \tag{23}$$

Flux is approximated at the cell interface by adding an appropriate amount of anti-diffusive term to the single point upstream weighted flux. TVD property of the scheme is achieved by applying this higher order flux correction term. To eliminate all the unphysical oscillations, a limiter function is employed that ensures that the scheme remains total variation diminishing. Higher order flux at the interface is given by

$$F_{i,k+1/2} = F_{i,k} + \frac{\phi(r)}{2}\left(F_{i,k+1} - F_{i,k}\right) , \tag{24}$$

where $\phi(r)$ is the flux limiter function that varies with the smoothness of data. Measure of smoothness of solution is obtained by the ratio of successive gradients,

$$r = \frac{F_{i,k} - F_{i,k-1}}{F_{i,k+1} - F_{i,k}} . \tag{25}$$

Different limiter functions are constructed by various authors. We have used three different types of flux limiters in our numerical schemes.

Van Leer Limiter $\qquad \phi(r) = \dfrac{|r| + r}{1 + |r|}$ $\qquad\qquad$ (26)

Minmod Limiter $\qquad\qquad \phi(r) = \max\left[o, \min(1, r)\right]$ $\qquad\qquad$ (27)

Fromm Limiter $\qquad\qquad \phi(r) = \max\left[0, \min\left(2, 2r, \dfrac{1+r}{2}\right)\right]$ $\qquad$ (28)

Total Variation Diminishing Scheme (Variables of Flux)

Instead of limiting the flux, higher order values of phase densities, fractional flows, and mole fractions are constructed at the cell interface.

$$\rho_{j,k+1/2} = \rho_{j,k} + \frac{\phi(r)}{2}\left(\rho_{j,k+1} - \rho_{j,k}\right) \tag{29}$$

31

$$r(\rho) = \frac{\rho_{j,k} - \rho_{j,k-1}}{\rho_{j,k+1} - \rho_{j,k}} \tag{30}$$

$$f_{j,k+1/2} = f_{j,k} + \frac{\phi(r)}{2}\left(f_{j,k+1} - f_{j,k}\right) \tag{31}$$

$$r(f) = \frac{f_{j,k} - f_{j,k-1}}{f_{j,k+1} - f_{j,k}} \tag{32}$$

$$x_{i,j,k+1/2} = x_{i,j,k} + \frac{\phi(r)}{2}\left(x_{i,j,k+1} - x_{i,j,k}\right) \tag{33}$$

$$r(x_{i,j}) = \frac{x_{i,j,k} - x_{i,j,k-1}}{x_{i,j,k+1} - x_{i,j,k}} \tag{34}$$

Fluxes are computed at the interface by using higher order densities, fractional flow, and mole fractions, i.e.,

$$F_{i,k+1/2} = \sum_{j=1}^{np} x_{i,j,k+1/2}\,\rho_{j,k+1/2}\,f_{j,k+1/2} \tag{35}$$

Parallelization

Finite difference part of the streamline simulator is performed in a sequential manner. Pressure solution and velocity field are computed in the finite difference grid on a single processor. Streamline module is parallelized using domain decomposition approach in which streamline domain is divided into sub domains. Fig. 6 shows a schematic flowchart of the parallel streamline framework used in this work. Streamlines are launched and distributed among different processors. The operations performed along any streamline do not require any information about neighboring streamlines. Streamlines are traced on individual processors and information on the underlying finite-difference grid is assigned to each streamline point. Streamline steps including streamline tracing, mappings, flux calculation, and 1-D solver are performed on different processors. All the processors execute streamline computations in parallel, each processing its assigned set of streamlines. The most time consuming flux calculation task is performed by multiple processors thereby reducing the computation time. No transfer of data across the streamlines is required while calculating fluxes and updating compositions along the streamlines.

Updated compositions of all the components along the streamline points are scattered on different processors. Although each processor operates on its own local set of streamlines independently, communication between all the processors is required to update the compositions in the finite difference grid. All the streamlines are gathered on a single processor before this updated information is mapped to the underlying finite difference grid. This communication (gathering) across the streamlines or processors is achieved by using message passing interface (MPI). MPI Gather function gathers all the information from streamlines that is processed on different nodes. This communication

time in gathering all the compositions from different processors adds to the total execution time.

```
┌─────────────────────────┐
│        Pressure         │◄─────────────────────┐
└─────────────────────────┘                      │
            │                                     │
            ▼                                     │
┌─────────────────────────┐                      │
│        Velocity         │                      │
└─────────────────────────┘                      │
            │                                     │
            ▼                                     │
┌─────────────────────────┐                      │
│    Launch Streamlines   │                      │
└─────────────────────────┘                      │
                                                  │
   ┌──────┬──────┬──────┐                         │
   ▼      ▼      ▼      ▼                          │
┌──────┐┌──────┐┌──────┐┌──────┐                  │
│Trace ││Trace ││Trace ││Trace │                  │
│Stream││Stream││Stream││Stream│                  │
│lines ││lines ││lines ││lines │                  │
└──────┘└──────┘└──────┘└──────┘                  │
┌──────┐┌──────┐┌──────┐┌──────┐                  │
│Mapp- ││Mapp- ││Mapp- ││Mapp- │                  │
│ings  ││ings  ││ings  ││ings  │                  │
└──────┘└──────┘└──────┘└──────┘                  │
┌──────┐┌──────┐┌──────┐┌──────┐                  │
│Flux  ││Flux  ││Flux  ││Flux  │                  │
│Eval  ││Eval  ││Eval  ││Eval  │                  │
└──────┘└──────┘└──────┘└──────┘                  │
┌──────┐┌──────┐┌──────┐┌──────┐                  │
│1-D   ││1-D   ││1-D   ││1-D   │                  │
│Solver││Solver││Solver││Solver│                  │
└──────┘└──────┘└──────┘└──────┘                  │
   └──────┴───┬──┴──────┘                         │
              ▼                                   │
┌─────────────────────────┐                       │
│    Gather Streamlines   │                       │
└─────────────────────────┘                       │
            │                                      │
            ▼                                      │
┌─────────────────────────┐                        │
│      Map to FD Grid     │                        │
└─────────────────────────┘                        │
            │                                       │
            ▼                                       │
┌─────────────────────────┐                         │
│    Finite Difference    │────────────────────────┘
└─────────────────────────┘
```
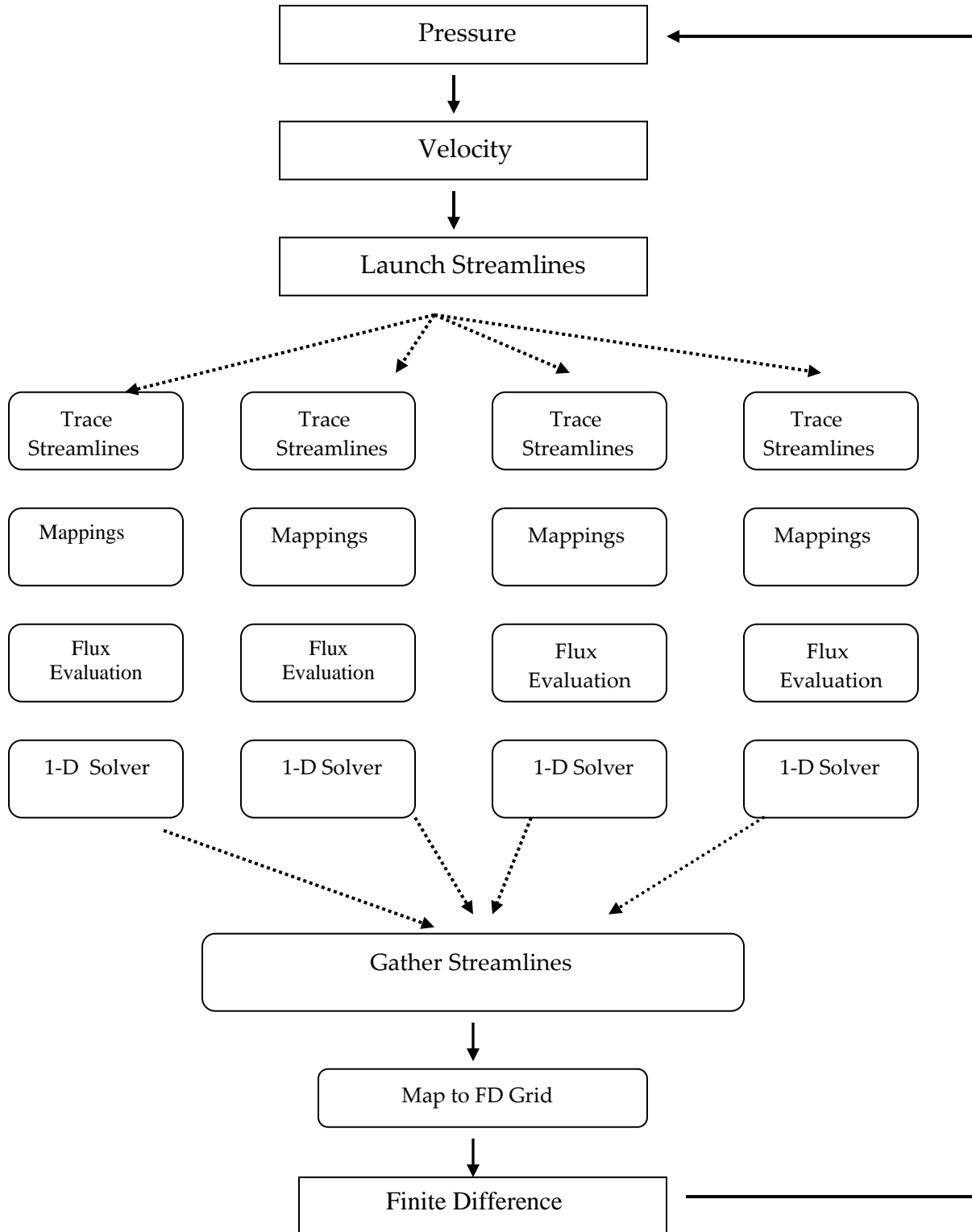
Fig. 6 - Framework for parallel streamline simulation

Modeling of Vapex

A numerical model was designed to simulate VAPEX experiments using CMG's fully compositional GEM software. The fluid model was derived from a PVT report of experiments performed on an oil from the same reservoir as the test oil. A two-region grid was developed to better simulate the flow of solvent into the cell during gas injection. Region 1 was intended to represent the solvent cylinder, initially filled with solvent at 200 psi. A porosity of 99% and permeability of 1E+6 md were assigned to this region that was divided into 11 grids. Initial solvent composition was 91%, or 100%-9% (S_{wc}). A non-zero connate water saturation was needed for numerical stability and so the value of 9% was used. Relative permeability was calculated using Corey type functions for the oil/water and oil/gas flows. Stone's First model was used to calculate relative permeability between water/gas flow. Region 2 represented the porous media and for some cases was 60 x 1 x 60 grids in i, j, and k directions, respectively; other cases contained 40 x 40 x 1 grids in the i, j, and k directions, respectively. A narrow strip of blocks connected the two regions in such a way that solvent injection occurs at the position corresponding to the experiment. To emulate a piston cylinder, water was injected into the bottom block of Region 1, displacing the solvent through the top to the strip of connecting blocks. Another very thin strip of blocks connected the producer well block to the bottom of Region 2, where effluent was collected in the experiment. Fig. 7 shows the grid and a schematic of the high pressure cell.

Fig. 7 – Simulation grid and sand pack schematic
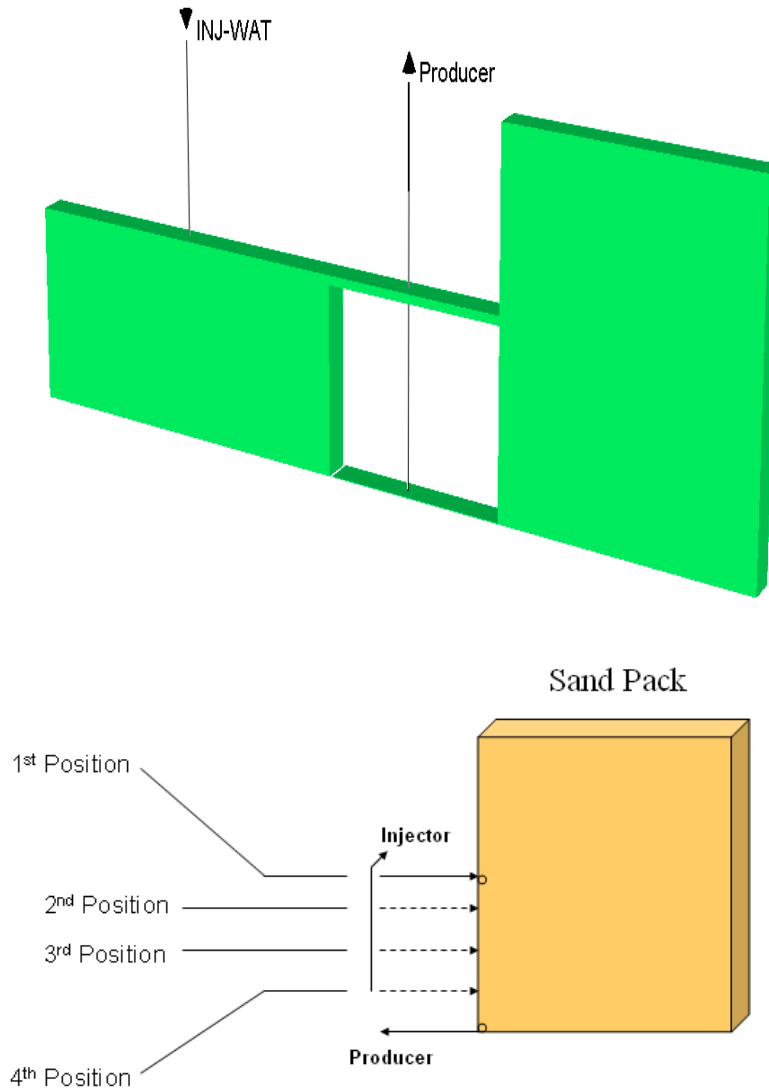
Initial pressure in the simulation was designed to match that of the experiment, with the pressure in Region 1 being the solvent source cylinder pressure and pressure in Region 2 was assigned the oil inlet pressure prior to solvent injection. Solvent injection pressure and flow rate into the porous media was not controlled but was allowed to vary as was in the experiment. A constant bottom hole pressure was assigned the producer well to imitate that observed in each experiment, typically in the range of 195-198 psi.

Results and Discussion

Slimtube

The slimtube was charged with the oil and displaced with the solvent (ethane) at various pressures. The oil recovery at 1.2 PV injection is shown in **Fig. 8**. The recovery increases with pressure. Above 6.895 MPa (1000 psi) recovery is above 95%. Although experimental slim tube data does not suffice to accurately determine MMP for ethane and this oil, numerical simulation supported the test results and helped to estimate an MMP. **Fig. 9** shows the simulated recovery generated from a 1D model representing the slim tube that was developed using GEM simulator of CMG. Fluid model parameters were taken from an equation of state model developed for this oil. The recovery curves for pressures above 600 psi coincide with each other. The recovery is much smaller for lower pressures. In **Fig. 10**, recovery at 1.2 PVI was plotted against the corresponding pressure for that run.
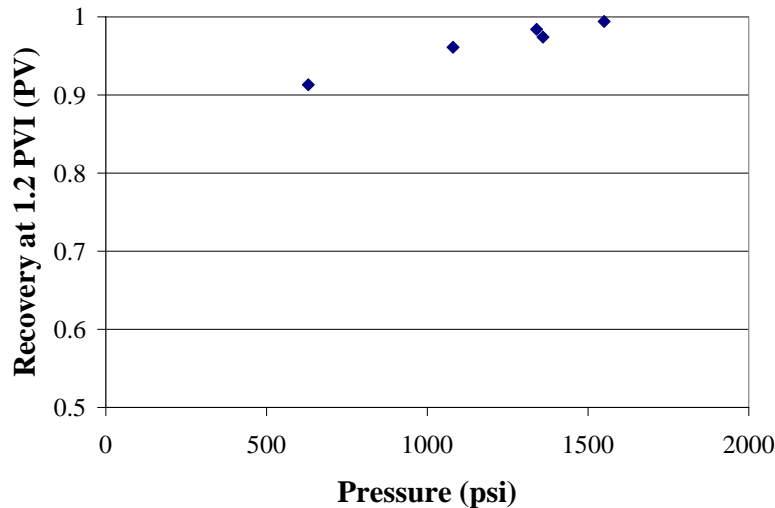
Fig. 8 – Slimtube rcovery at 1.2 PV solvent injection
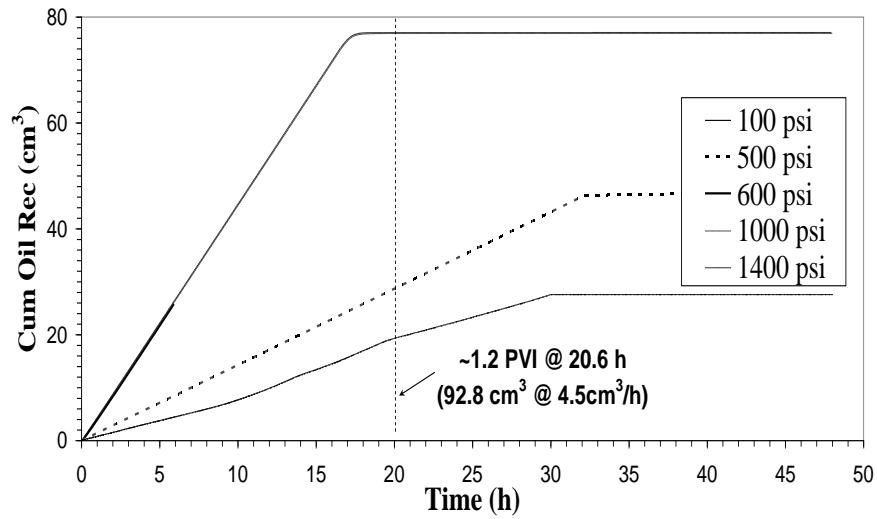
Fig. 9 – Cumulative oil recovery slimtube simulation
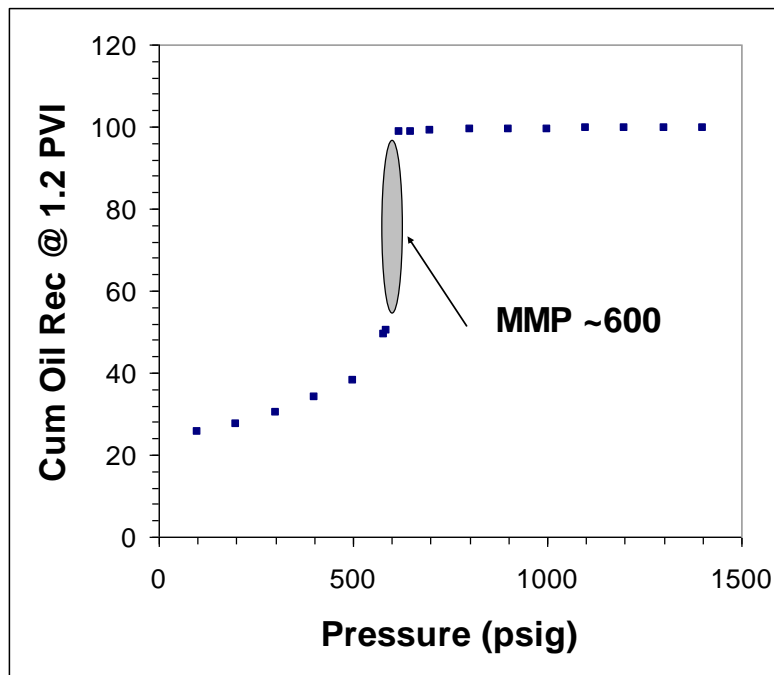
Fig. 10 – Simulated oil recovery at 1.2PVI

Simulation indicates that MMP for C2 and the dead oil is ~4.137 MPa (600 psi).

Coincidentally, vapor pressure of C2 at 77°F is 4.185MPa (607 psi). Numerical

instabilities resulted near the phase transition pressure, making it difficult to simulate slim tube runs near ~4.137 MPa (600 psi). More experimental points at lower pressures would help to confirm the numerical results. The effluent from the slimtube before the BPR was found to be two-phases in a visual cell at 9.239 MPa (1340 psi), indicating that ethane is multiconact miscible, not first contact miscible.

Corefloods

The Berea core was flooded with oil A at a steady flow of 9 ml/hr. Then gas (solvent 1) was injected into the core at the same rate after oil injection. 0.6 PV of solvent 1 was injected followed by water. The composition of the injection solvent is listed in Table 1; it is an equimolar mixture of NGL and LG. This solvent is multicontact miscible at the core pressure according to previous slimtube studies. The pressure drop across the core as the function of gas injection is shown in **Fig. 11**. Pressure drop decreases sharply as the gas breaks through the core. The final pressure drop is very small indicating that there is no injectivity problem associated with the solvent injection.
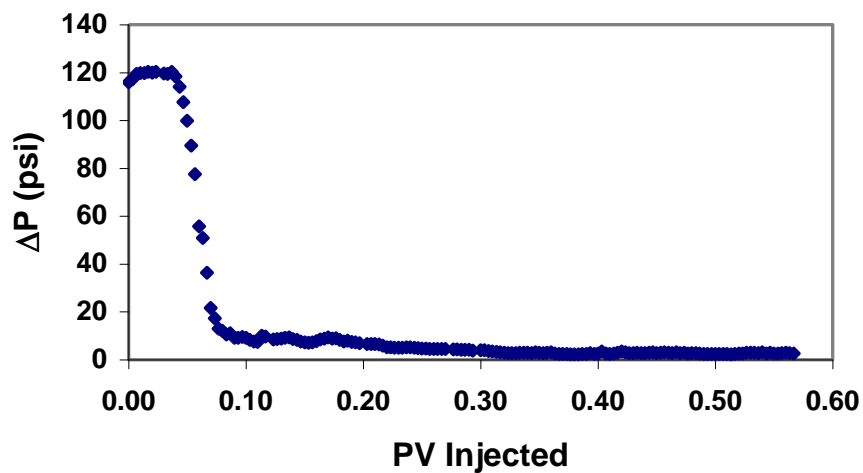
Fig. 11 – Pressure drop in coreflood during gas injection

The cumulative oil production as a function of gas injection is shown in **Fig. 12** (along with the results from WAG injections). Oil production rate falls after about 0.25 PV injection of solvent indicating breakthrough of solvent. The cumulative production of oil at the end of solvent injection is about 45% of the original oil. Water injection was continued for another 1.4 PV and the final recovery is about 67% OOIP.
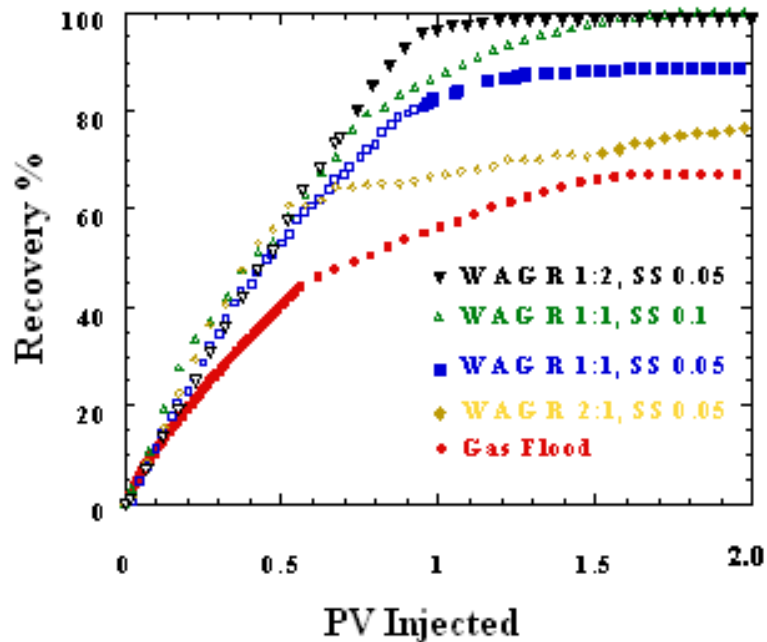
Fig. 12 – Cumulative oil production vs. PV gas injection

In 1D (slimtube) displacement of oil by this multicontact miscible solvent, the recovery is often greater than 95%. The existence of a residual oil of 33% in the coreflood implies bypassing in the core leading to immiscibility development and residual oil trapping. This miscible flood in the core is not hydrodynamically stable because of adverse mobility ratio. This adverse mobility and core-scale heterogeneity lead to bypassing. Bypassing can lead to immiscibility development and residual oil trapping. In

addition, the waterflood after the gasflood displaces the gas from the gasflooded region; a part of the originally bypassed region never contacts the solvent. Thus the oil recovery is low. Water-alternating-gas slugs were injected in the following experiments to minimize bypassing.
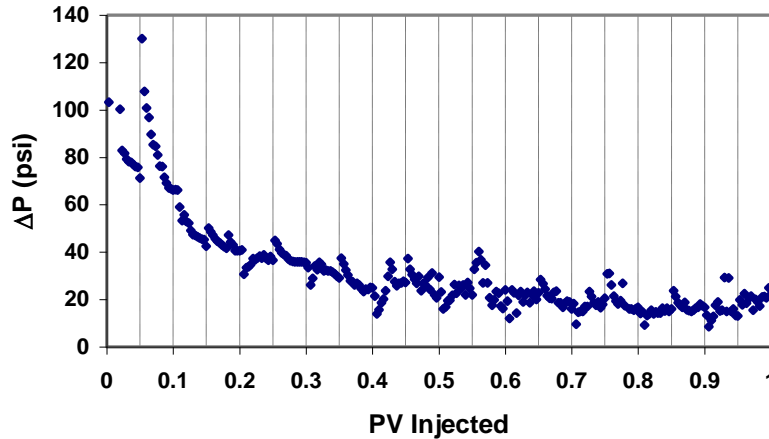
Fig. 13 – Pressure drop for WAG ratio =1 flood, slug size = 0.05 PV

The WAG ratio of 1 with the slug size of 0.05 PV was used in the second experiment. About 0.5 PV of total solvent was injected. About 0.5 PV of brine was injected alternating with the gas slugs followed by another 1 PV of water. The pressure drop versus cumulative injection is shown in **Fig. 13**. Every time a gas slug is injected, the pressure drop decreases because gas is less viscous than oil or water. Every time a brine slug is injected, the pressure drop first increases and then decreases because of relative permeability effects.

The cumulative oil production is shown in Fig. 12. The oil production rate is about constant until about 0.35 PV injection. The oil production rate falls after 0.35 PV injection, but not as much as in the gas flood. Water production increases after 0.35 PV injection. With the WAG ratio 1:1, about 80% of oil was recovered by the end of the end

of the WAG injection (i.e., 1 PV). By the end of the follow-up water injection (2 PV total injection), the oil recovery was 88%. This experiment shows that WAG injection stabilizes the displacement at the core-scale and gives recovery similar to 1D slimtube floods.

WAG ratio of 1 with the slug size of 0.1 PV was used in the next experiment. After 0.1 PV gas injection, 0.1 PV of brine was injected at the same flow rate. The procedure was repeated with gas and brine injection until a total 0.5 pore volume of gas was injected into the core. This was followed up with a brine injection for a total of 2 PV of gas and brine injection. The oil recovery is almost 100% OOIP in this experiment.

WAG ratio of 2 with the slug size of 0.05 pore volume was used in the following experiment. The experiment started with 0.05 PV of gas injection followed by 0.1 PV of brine. The total of 0.5 PV of gas mixture was injected into the core in this experiment. The oil recovery is about 77% OOIP.

An additional linear WAG flood with a slug size of 0.05 PV and a WAG ratio of 0.5 was conducted. The oil recovery is about 100% in this WAG flood. Fig. 12 shows the comparison in percentage oil recovery for gasflood with different WAG floods. As the WAG ratio increases, the oil recovery increases for WAG ratio 0 to 0.5, but then decreases from 0.5 to 2. Thus, the optimum WAG ratio for this core is about 0.5 in this linear core geometry. The oil recovery increases with the slug size at a constant WAG ratio.

Quarter 5-Spot Waterflood

In the waterflood, water was injected at a flow rate of 22.5 ml/hr. This same flow rate was also used for subsequent gas and WAG floods. Vertical injection and production wells were used in this waterflood. The cumulative oil production is shown in **Fig. 14** and

it is compared with oil production from another quarter 5-spot reported in the literature[27] at different viscosity ratios (VR). The literature data shows that at a VR=0.083, the displacement is stable with water breakthrough at 0.78 PVI and very little oil production after breakthrough. The breakthrough pore volume and recovery at 2 PVI decrease as viscosity ratio increases. The viscosity ratio for our waterflood is 78. Our experimental data falls in between those of VR= 8.08 and 141 from the literature. Breakthrough is at ~0.21 PVI and oil recovery is 0.48 PV at 2 PVI. This consistency with the literature data validates our 5-spot packing.
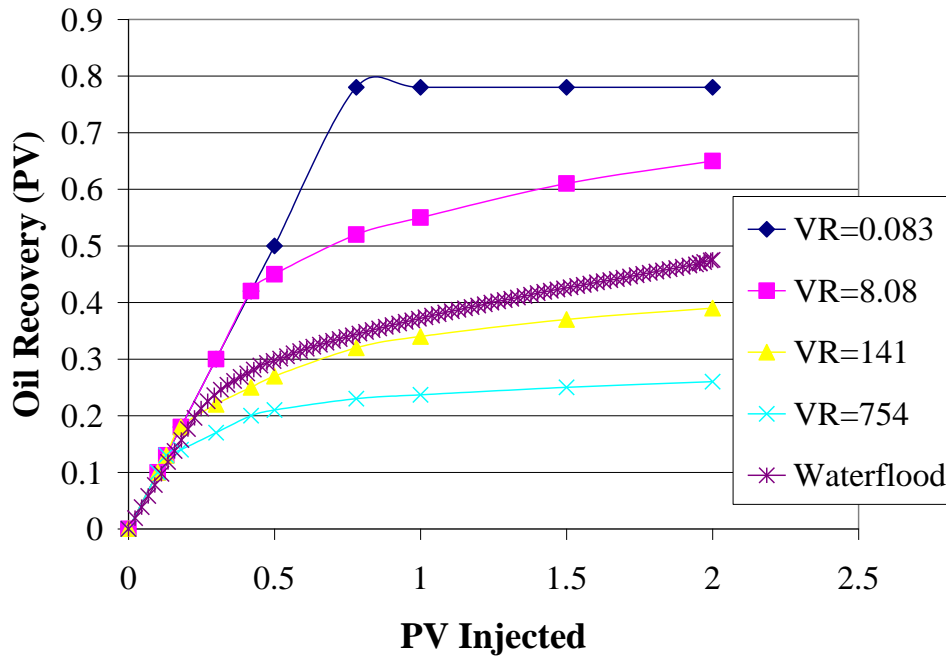
Fig. 14 – Comparison of waterflood recovery in 5-spots with literature data[34]

Quarter 5-Spot Gasflood

The gasfloods were started with an initial water saturation of ~9% in the quarter 5-spot cell. These are all secondary gasfloods. 0.5 PV of ethane was injected followed by

1.5 PV of water. The injection flow rate was 22.5 ml/hr for solvent and water. The back pressure regulator pressure was set at 9.515 MPa (1380 psi). Vertical injection and production wells were used in this experiment. **Fig. 15** shows the oil recovery for this gasflood and compares it with the waterflood. Solvent breakthrough occurs at ~7% PVI for the solvent compared to the 21% PVI for the waterflood. Oil recovery at the end of solvent injection (0.5 PVI) is ~19% PV compared to ~30% PV for the waterflood. Gasflood recovery is lower because of lower sweep due to higher viscosity ratio between oil and solvent. Water was injected after 0.5 PV of solvent injection. Its effect on recovery is felt at about 0.66 PV of total (solvent and water) injection when the oil recovery rate increases. The water actually breaks through at about 0.83 PV injected. The higher oil production rate persists until about 1 PVI, when the recovery rate starts decreasing. The overall oil recovery at 2 PVI is 55% compared to 48% for the waterflood (without any solvent injection). Some of the solvent condenses into the oil, reduces its viscosity and improves (reduces) mobility ratio between water and the oil. This results in better displacement of reduced viscosity oil by water. The viscosity of the separator oil (after the BPR) was analyzed; viscosity decreases after breakthrough and then increases indicating a multicontact displacement (not first contact miscibility).
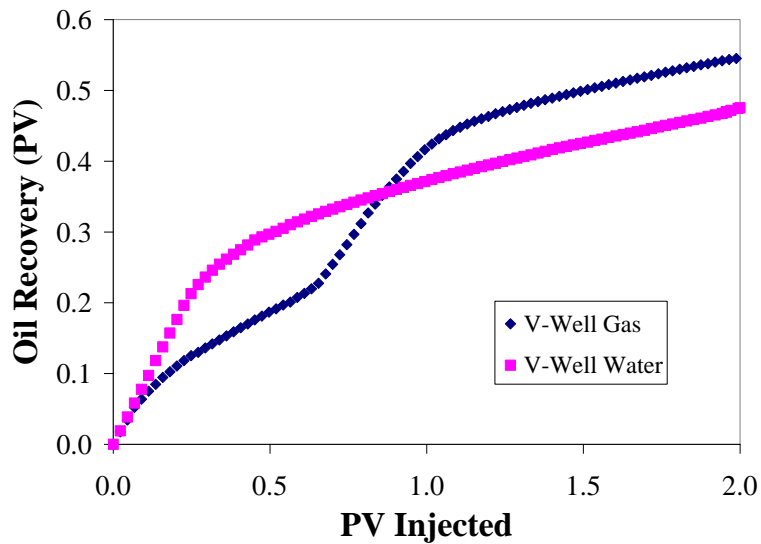
Fig. 15 – Oil production in the 5-spot model

The quarter 5-spot model is supposed to represent a quarter 5-spot in the field. The distances and the residence time for the solvent are, of course, much shorter in this model than in the field. We wanted to verify whether there is enough contact to establish miscibility in this short model. We added an oil-filled slimtube upstream of the model in one gas flood experiment. The pore volume of the slimtube was about 0.15 of the 5-spot model pore volume. We injected ethane for about 0.5 PV of this combined system. **Fig. 16** shows the oil recovery; the gas breaks through at about 0.2 PVI of the overall system. The slimtube behaves like a one-dimensional system; the solvent breaks through from the slimtube at about 0.13 PVI of the overall system and takes an additional 0.07 PVI to break through at the 5-spot production well. Oil production rate beyond solvent breakthrough is similar to that of the 5-spot without the slimtube.
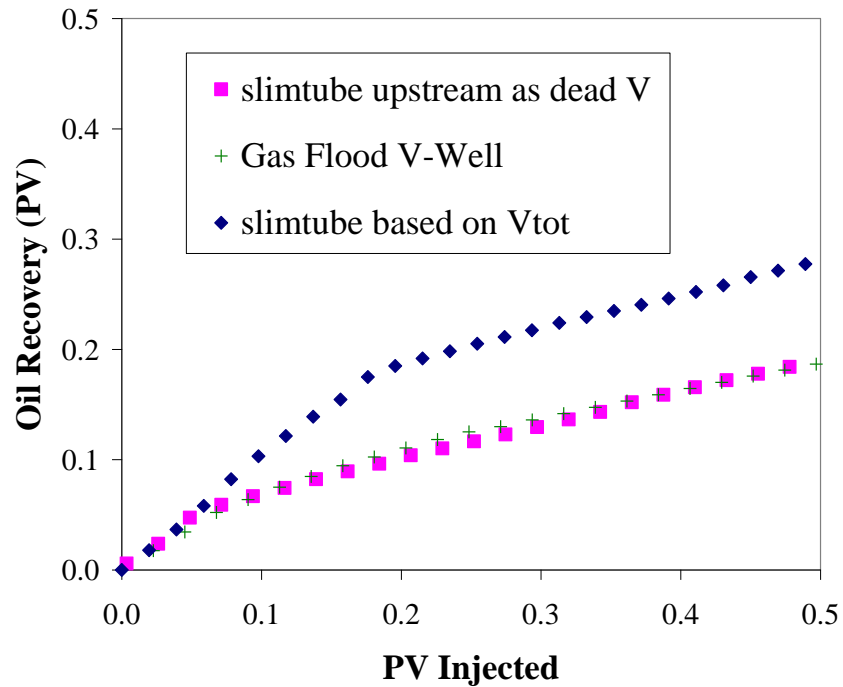
Fig. 16 – Comparison of gasfloods with and without an upstream slimtube

We considered the slimtube as a dead volume, subtracted the slimtube oil both from the recovery and pore volume, and replotted the data. That data is also shown in Fig. 16 and compared with the 5-spot gasflood recovery data without any slimtube. These two data sets look very similar indicating that the gasflood inside the 5-spot model behaved similarly with and without the upstream slimtube. There are enough contacts between the oil and solvent at the entrance of the 5-spot model and the length for miscibility development is not an issue. All the other experiments are conducted without an upstream slimtube.

Pressure is an important parameter in all gasfloods. Slim tube simulation along with supporting experimental data showed that MMP between C2 and the dead oil is ~4.137 MPa (600 psi). Several gasfloods followed by waterflood experiments were

conducted at different pressures. The volume of solvent injected was always 0.5 PV, but at the corresponding pressures. The volume of subsequent water injected was 1.5 PV. The oil recovery is shown in **Fig. 17**. The solvent breakthrough varies from $7 - 9\%$ PVI as the pressure falls. The oil recovery in the gasflood phase (<0.5 PVI) does not decrease with pressure; in fact, it increases slightly as the pressure decreases. The subsequent waterflood recovers almost the same amount of oil leading the cumulative recovery to be higher at lower pressures, i.e., 55% at 1380 psi, 59% at 950 psi and 62% at 660 psi. Water breakthrough varied from 82% to 87%.

Numerical simulation of these five-spot experiments was conducted to discern the trend in oil recovery with pressure. CMG GEM software was used to model the process. A two-region grid (as shown in the inset of **Fig. 18**) was used to emulate the porous sand pack connected to the solvent cylinder (the volume change of the fluid in the cylinder due to pressure fluctuations was considered important). The solvent cylinder was modeled by a region of 11x1x1 grids of 99% porosity and 1E+6 md permeability. The porous medium was modeled by 21x21x10 grids oriented along the diagonal of the five-spot (as shown in **Fig. 19**). Fig. 18 shows the simulated oil recovery for the 9.514 MPa (1380 psi), 6.550 MPa (950 psi) and 4.550 MPa (660 psi) runs, as well as the experimental data for the 9.514 MPa case. Simulated oil recovery is almost independent of pressure in this pressure range. It does not decrease with decrease in pressure, even though less solvent is injected (in terms of moles) at low pressure. Simulated recovery approximately matches the experimental recovery at 9.514 MPa (1380 psi).
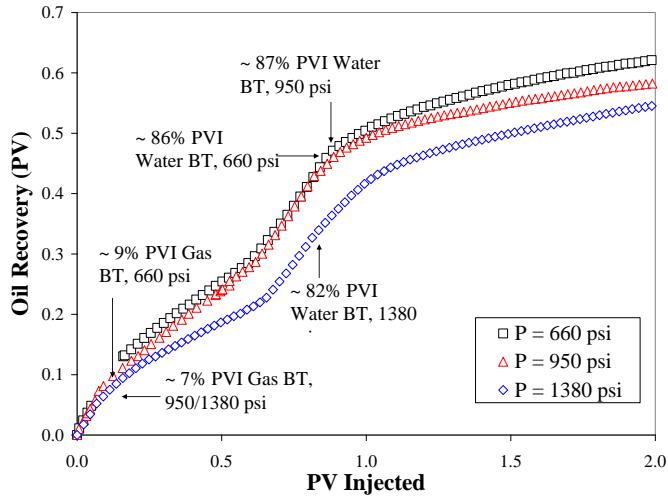
Fig. 17 – Effect of BPR pressure on gasflood oil recovery in the 5-spot model
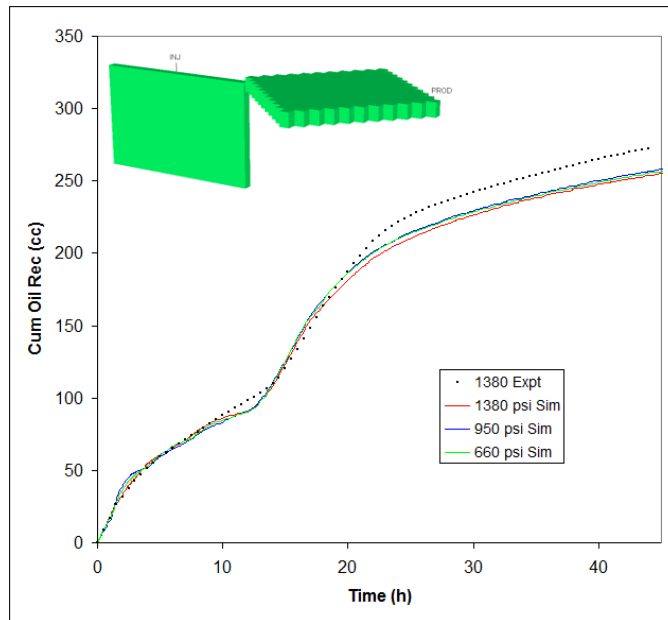
Fig. 18 – Comparison of experimental recovery with simulation

In-situ oil saturation and composition were analyzed to understand the sweep efficiency in these runs. **Fig. 19** shows areal plots of oil saturation in the top four layers of the model (there were no differences in lower layers at different pressures). This was

at the end of the gas flood (0.5 PVI). The gravity override is very obvious. The injected solvent sweeps only the top three layers; the nonproducing corners are also bypassed. At the higher pressure, oil saturation is lower (more green) in layers 2-4. Thus displacement efficiency increases with pressure. But the overall recovery is almost independent of pressure in the studied range, as shown in Fig. 18. This implies that the sweep efficiency decreases with the increase in pressure.
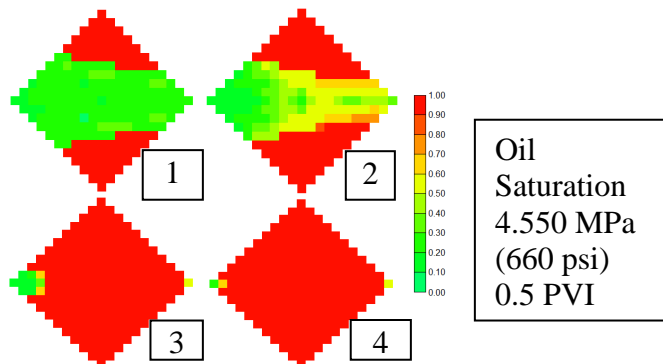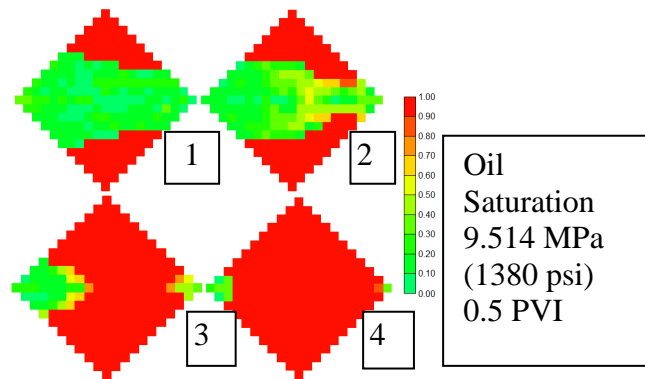
Fig. 19 – Oil saturation first 4 layers in 5-spot

Inverse 9-Spot Gasflood

Fig. 20 shows oil production from both the inverse 9-spot and the 5-spot model gasflood experiments. The cumulative oil production from the diagonal well, side wells

and the total are plotted. Oil is produced primarily from the side wells first; diagonal well oil production picks up after about 0.8 PVI. The total production is very similar to that of the 5-spot, only slightly higher. The final pressure drop is slightly smaller for the inverse 9-spot (0.003 MPa (0.5 psi)) than the 5-spot (0.004 MPa (0.6 psi)).
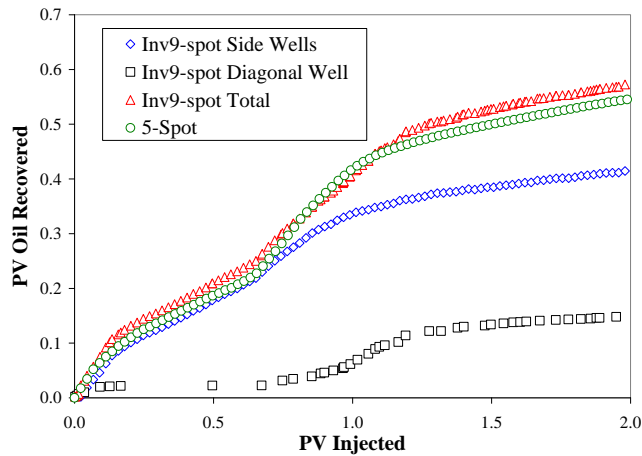
Fig. 20 – Comparison of oil recovery between an inverse 9-spot and 5-spot models

5-Spot WAG Flood

In the gasflood experiments, solvent breaks through by about 7% PVI because of viscous fingering and thus is not utilized sufficiently in solubilizing and displacing the oil. Injection of small slugs of solvent and water in WAG injections minimizes this problem. Vertical injection and production wells were used in most of the WAG floods. At the beginning of the WAG experiments slugs of solvent and water were injected alternately until 0.5 PV of solvent was injected, after which water was injected continuously until a total injection of 2 PV. All these floods are secondary WAG; thus the first slug was always solvent. The injection flow rate was 22.5 ml/hr for solvent and water. The back pressure regulator pressure was set at 9.308 MPa (1350 psi). We have

50

shown before that oil recovery increases as the solvent slug size decreases.[26] The solvent

slug size was kept constant at 1% PV in this set of experiments.
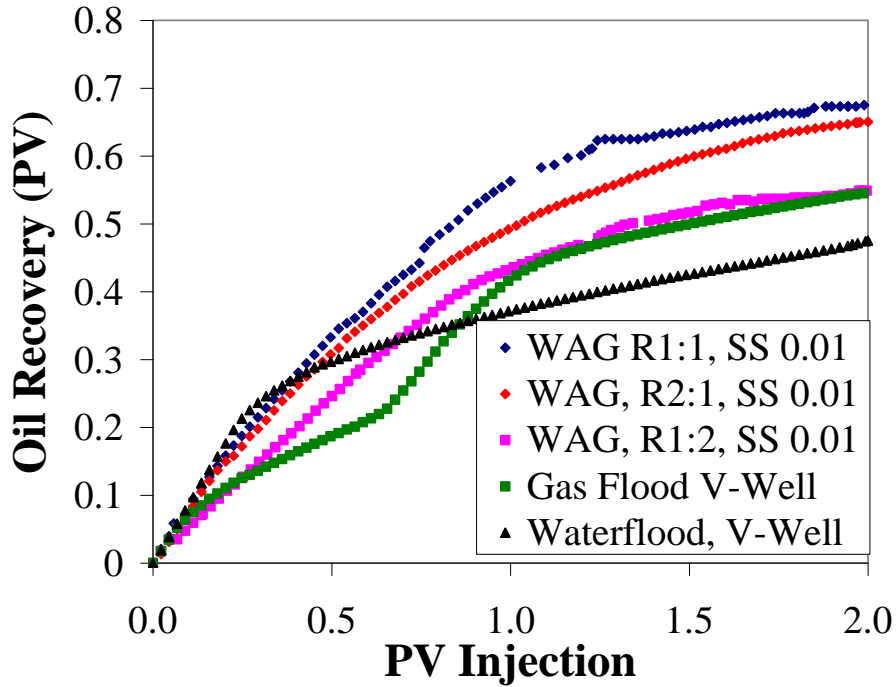
Fig. 21 – Effect of WAG ratio in the quarter 5-spot model

Fig. 21 shows the effect of WAG ratio on oil production. The waterflood (WAG

ratio = ∞) and gasflood (WAG ratio = 0) data are also included for comparison. Tabulated

data on break through times and oil recovery are given in Table 4.   For the WAG

injection with the WAG ratio of 1 and slug size (SS) of 0.01 PV, the oil recovery is about

0.68 PV. Oil recovery is much higher than the waterflood (0.48 PV) and gasflood (0.55

PVI). Gas breakthrough occurs at about 12% PVI and water breakthrough at about 52%

PVI. About 0.56 PV of oil is produced during the WAG portion of the experiment, which

corresponds to a total fluid injection of 1 PV. After the water injection, the oil production

rate decreases, but oil continues to be produced even at the 2 PV total injection point

when the experiment is stopped. The total oil recovery is 68% PV (75% OOIP). This high

recovery is possible because the medium is almost homogeneous, ethane is a MCM solvent and it reduces the oil viscosity substantially.

WAG Ratio	Slug Size (% PV)	Gas B.T. (% PV)	Water B.T. (% PV)	Oil Rec. at 2.0 PVI (%PV)
∞	N/A	N/A	22	48
0	N/A	7%	83	55
0.5	1	9	80	55
1	1	12	52	68
1	5	10	56	60
2	1	8	40	65

Table 4 - Experimental parameters, break through times and recovery

As the WAG ratio is decreased to 1:2, the oil recovery falls substantially to about 0.55 PV. About 0.36 PV of oil is produced during the WAG injection, which corresponds to a total fluid injection of 0.75 PV. About 0.19 PV of oil is produced during the post-WAG water injection. The gas breaks through early about 9% PVI and the water breaks through at 80% PVI. As the WAG ratio is increased to 2, the oil recovery falls slightly (from the WAG ratio =1 case) to about 0.65 PV. Alternating gas and water injection continues to 1.5 PVI in this case, followed by additional 0.5 PV of continuous water injection. The gas broke through at about 0.08 PVI and the water broke through at 0.4

PVI. As the WAG ratio is increased, the recovery increases and after an optimum value (close to 1 or 2) it decreases. More experiments should be run at higher WAG ratios to identify this optimum.
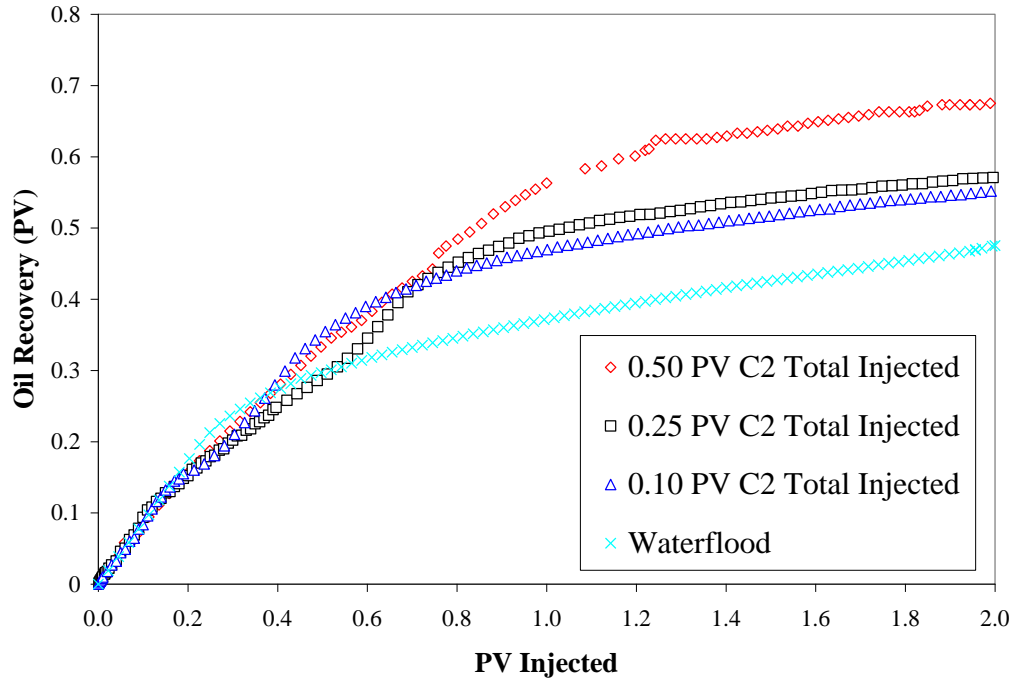
Fig. 22 – Effect of solvent amount in WAG injection in the quarter 5-spot model

The solvent amount of 0.5 PV may be expensive to inject under certain price scenarios.[35] Therefore, we investigated the effect of solvent amount on oil recovery. In this set of experiments, the WAG ratio was fixed at 1 and the slug size at 1% PV. The solvent amount was varied from 10% to 50% PV. The WAG injection was followed by continuous water injection up to a total injection of 2 PV. **Fig. 22** shows the oil recovery for solvent amount varying from 0.5 PV to 0 PV (waterflood). Oil recovery decreases from 0.68 PV for 0.5 PV solvent to 0.57 PV for 0.25 PV, to 0.55 PV for 0.1 PV to 0.48

PV for no solvent. The amount of oil recovery increase is 14% for a 0.1 PV solvent over that of waterflood. This amount is significant and the kind of increase McGuire et al.[2] have seen in VR-WAG. The final pressure drop increases as the solvent amount decreases (0.002 MPa to 0.007 MPa (0.3 psi to 1 psi)) indicating more remaining oil and gas.
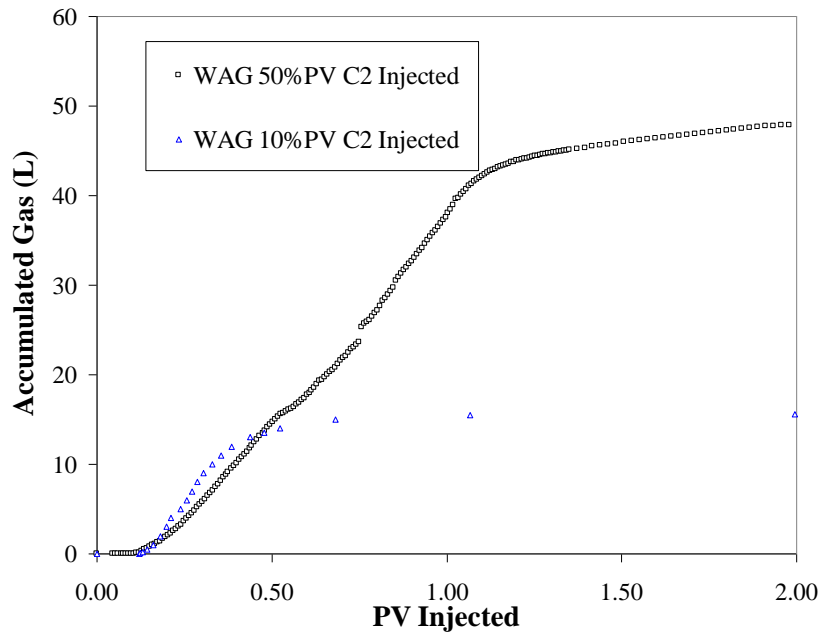
Fig. 23 - Gas production during WAG injection in the quarter 5-spot model

Fig. 23 shows the gas production during these WAG floods. The WAG ratio is 1 and the slug size of 0.01 PV for both these floods. Less gas is produced with less solvent injection, but the gas produced in the higher solvent injection case is less than 5 times the other case. Amount of gas left behind in cell is very little for 10% C2 injection and significant for 50% C2 injection. Most of the solvent probably is solubilized into the oil phase and is produced as the solution gas in the 10% C2 injection case. Thus gas utilization is higher in this case.
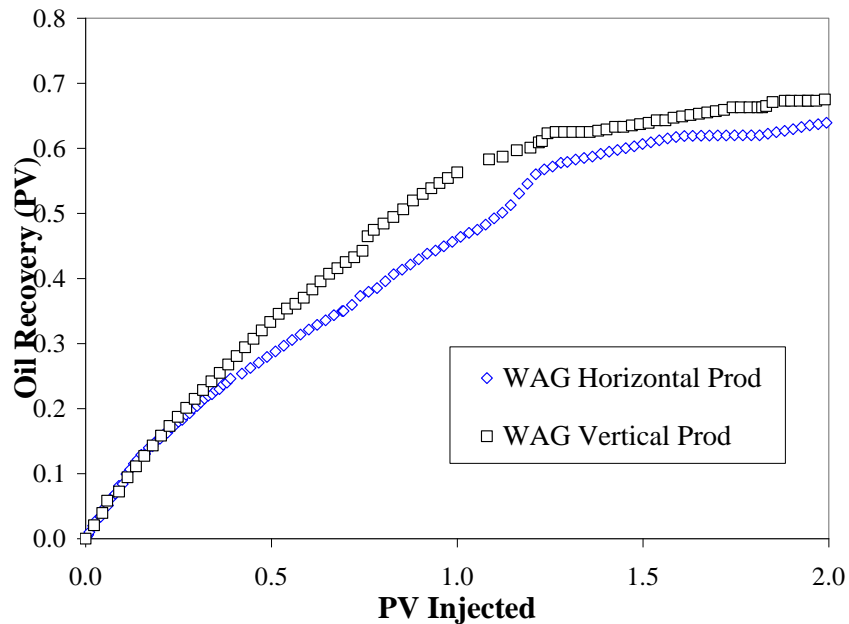
Fig. 24 – Effect of horizontal production well in WAG injection in the quarter 5-spot

model

Most of the flow resistance is around production wells in viscous oil reservoirs. Horizontal production wells are used in viscous oil reservoirs to increase well productivity. One WAG experiment was conducted with a vertical injection well and a horizontal production well. The production well length was half the width of the quarter 5-spot pattern. WAG ratio was 1 and slug size was 1% PV. The oil recovery from this experiment is plotted in **Fig. 24** and compared with that from a similar experiment with a vertical production well. The gas breakthrough time is very similar, but the production in the horizontal well case is significantly smaller during the WAG phase (46% vs. 56%). After the subsequent waterflood, the difference in oil recovery decreases (64% vs. 68%). The tip of the horizontal well is closer to the injection well than the vertical production well. Thus, solvent and water slugs tend to bypass some oil on the other side of the 5-spot lowering the sweep efficiency.

Approximate Sweep Efficiency

Sweep efficiency is not measured directly in these experiments. Modeling these experiments with a compositional simulator can lead to accurate estimates of sweep efficiency. Here we make an approximate estimate of sweep efficiency by assuming that gas or WAG floods leave no oil residual ($S_{org} = 0$) and waterflood leaves 30% oil residual ($S_{orw} = 0.3$). Table 5 shows these estimates for each flood. Each flood has two stages, gas/WAG flood and then subsequent waterflood. The recovery from the two stages are called x and y in the table, respectively. x and y can be identified from the recovery curves. The sweep at the end of stage 1 is called S1 in the table and is computed by x/(1-Swi). The additional sweep in the second stage is called S2 in the table and is computed by y/(1-Swi-Sor). The total sweep is the sum of (S1+ S2). These estimates are only approximate for gasfloods and perhaps lower bounds for WAG floods.

As shown in Table 5, waterflood has a sweep of about 79%. Continuous gas injection at 9.515 MPa (1380 psi) has a sweep of about 20.5%, not very different from that of an attached upstream slimtube. However, subsequent waterflood after the gasflood brings the total sweep to about 79.6%, similar to that of the waterflood. In the following, the sweep efficiencies (S1) during the gas floods and WAG floods are compared. Decreasing the injection pressure during these gasfloods improves the sweep to about 27.6% (from 20.5%). Gasflood in an inverted 9-spot has a sweep of about 23.1%, slightly higher than that of the 5-spot (20.5%). WAG injection improves the sweep to about 61.5% for WAG ratio of 1:1. A similar WAG flood with a horizontal production well decreases the sweep to 50.5%. As the WAG ratio increases from 1:2 to 2:1, the sweep efficiency increases, from 39.6% to 65.9%. Actually, these estimates are lower bounds of

sweep for WAG floods, because the assumption of $S_{org} = 0$ is incorrect for the swept region during the WAG phase.

Experiment	x	y	Total Recovery	S1	S2	Total Sweep
Water Flood V-Well	0.000	0.480	0.480	0.000	0.787	78.7%
Slim Tube + Five-Spot (V-Well)	0.191		0.191	0.210		21.0%
Cont. Gas Flood V-Well 1380 psi	0.187	0.360	0.547	0.205	0.590	79.6%
Cont. Gas Flood V-Well 950 psi	0.240	0.342	0.582	0.264	0.561	82.4%
Cont. Gas Flood V-Well 660 psi	0.251	0.370	0.621	0.276	0.607	88.2%
Inverted Nine-Spot	0.210	0.363	0.573	0.231	0.595	82.6%
WAG 1:1, 1%SS 50%PV C2 Injected	0.560	0.120	0.680	0.615	0.197	81.2%
WAG 1:1, 1%SS 25%PV C2 Injected	0.290	0.280	0.570	0.319	0.459	77.8%
WAG 1:1, 1%SS 10%PV C2 Injected	0.160	0.390	0.550	0.176	0.639	81.5%
WAG 2:1, 1%SS 50%PV C2 Injected	0.600	0.050	0.650	0.659	0.082	74.1%
WAG 1:2, 1%SS 50%PV C2 Injected	0.360	0.190	0.550	0.396	0.311	70.7%
WAG 1:1, 1%SS 50%PV C2 Injected Horiz. Prod. Well	0.460	0.180	0.640	0.505	0.295	80.1%

Table 5 – Estimated sweep efficiency based on oil recovery

Foam Flooding

We have performed foam floods with the surfactant to gas ratios of 1:1, 1:5 and 1:10 in the quarter 5-spot model. The 5-spot was at connate water saturation before the foam flood. The surfactant slug size in each case was 5cc. The gas slug size was 5cc, 25cc or 50cc of gas in depending on the surfactant to gas ratio 1:1, 1:5 and 1:10, respectively. The total amount of gas injection was 250cc (0.5PV) in all of the cases and thereafter we only water was injected up to a total injection of 2PV. In the first three experiments, a sand pack was present before the quarter 5 spot and when we observed the foam through the visual cell (after the sand pack and before the 5-spot), we started to inject the foam into the quarter 5 spot. In the last experiment, there was no sand pack; surfactant and gas were injected directly into the quarter 5-spot. This experiment is referred to as 1:1 in situ foam experiment.

Fig. 25 shows the oil recovery in foam flooding experiments. In the 1:10 SAG ratio experiment, gas breaks through at about 0.8 PV throughput, very similar to the case of gasflood. Oil recovery rate falls after the gas breakthough. At about 0.55 PV throughput, foam injection ceases and only water is injected continuously. The oil production rate increases for some time after continuous water injection starts indicating that the bottom part of the cell is not swept by gas and responds to water injection, similar to the case of gasflood. The oil recovery at the end of 2 PV throughput is 0.52 PV, again similar to the case of gas injection followed by waterflood. At low SAG ratio (1:10), foam is not very effective; it behave almost like a gasflood.
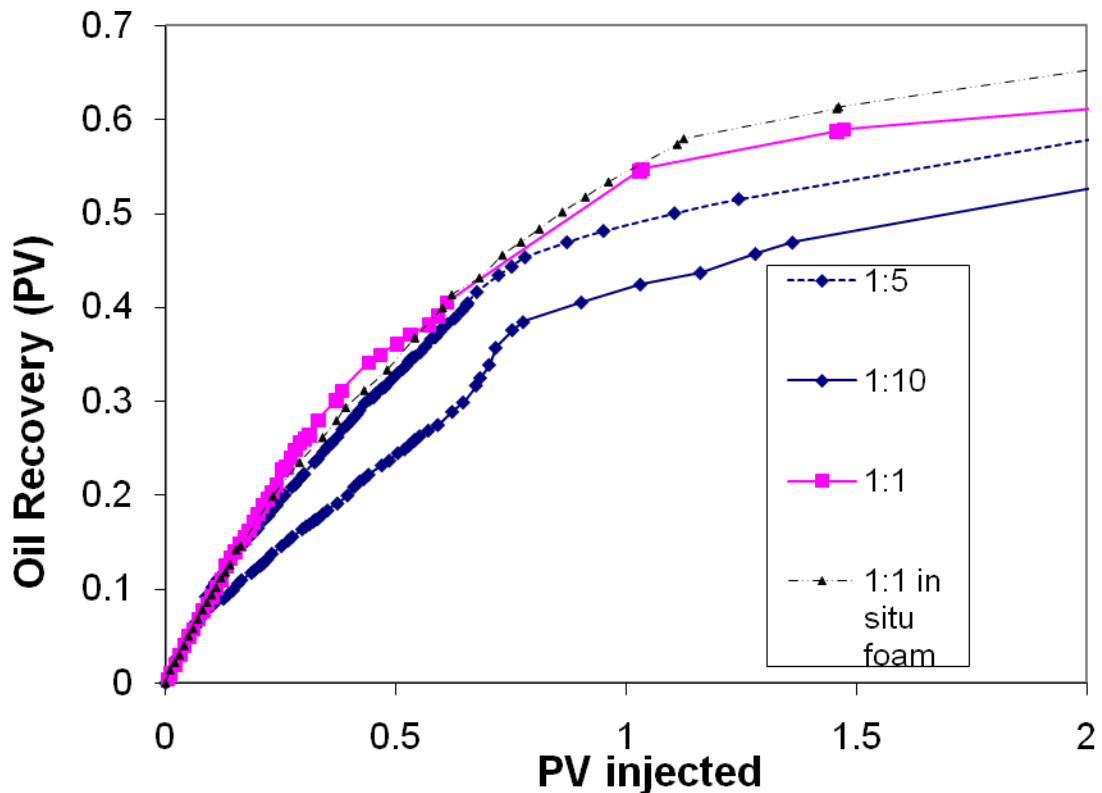
Fig. 25 – Oil recovery in foam flooding experiments in the quarter 5-spot

As the SAG ratio increases, oil recovery increases. For a SAG ratio of 1:5, breakthrough is at about 0.15 PV and the recovery at 2 PV injection is 0.58 PV. In this case, water injection starts at 0.6 PV throughput. For a SAG ratio of 1:1, breakthrough is at about 0.16 PV and the recovery at 2 PV injection is 0.61 PV. In this case, water injection starts at 1 PV throughput. This experiment was repeated without the sand pack before the 5-spot, the so called 1:1 in situ foam experiment. In this experiment, The recovery was slightly higher, 0.65 PV at the end of 2 PV throughput. Thus, pregeneration of foam did not help increase the recovery.

Fig. 26 shows the gas produced in the above four foam injection experiments. The gas volume is reported at the atmospheric conditions. As the SAG ratio increases, the gas

60

production decreases. This is because foam is more effective at the higher SAG ratio and it sweeps more of the cell. More gas is present inside the 5-spot cell at the end of the floods for higher SAG ratio; thus less gas is produced. In the case of in situ foam, the surfactant and gas slugs are injected directly into the cell; thus more gas is produced than in the case of 1:1 SAG ratio with a sand pack.
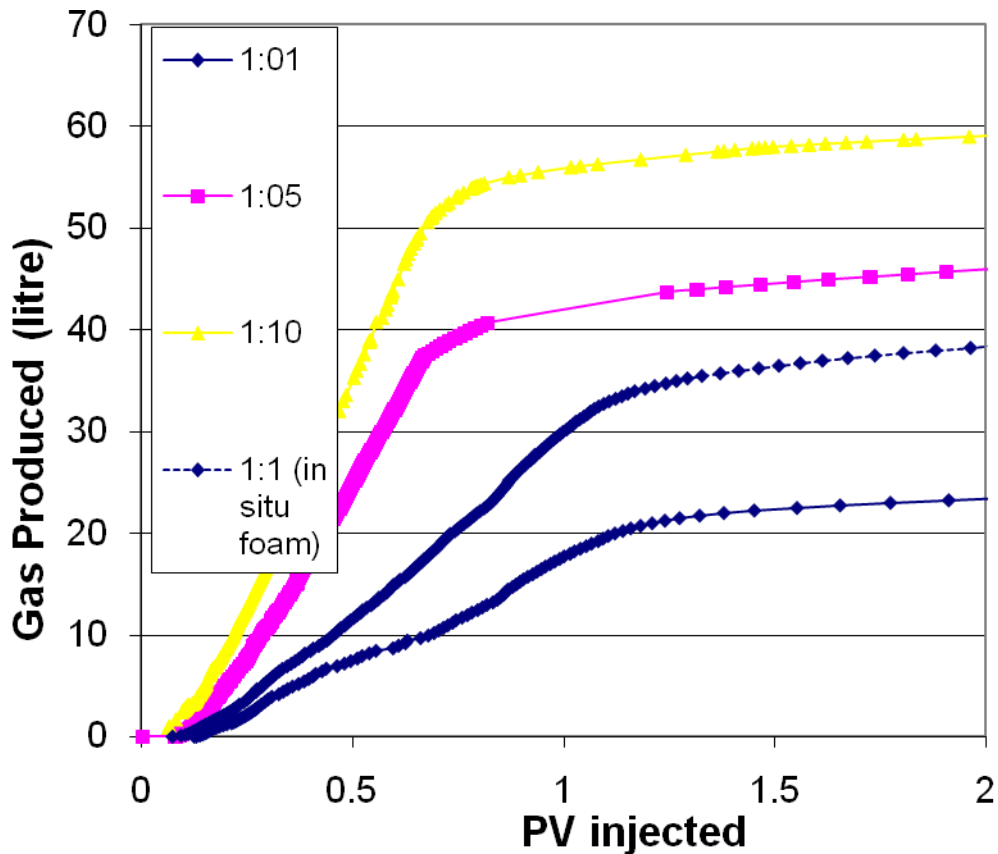
Fig. 26 – Oil recovery in foam flooding experiments in the quarter 5-spot

Vapex Experiments

Effect of Well Spacing

Vertical spacing between the injector (higher elevation) and producer (lower elevation) wells was varied in three separate experiments to study the effect on oil recovery. **Fig. 27**

shows oil recovery for three different runs in which the well spacing was 5 in., 3.75 in., and 2.5 in. It appears that varying the distance between the wells in this range (2.5 – 5 in.) did not have a profound effect on cumulative oil recovery. In each of these experiments the back pressure regulator (TEMCO BPR-50-1) was used to maintain the outlet pressure. As is also evident from these curves, it was difficult to manage the oil/gas effluent flow rates using the BPR and pressure at the outlet varied greatly.
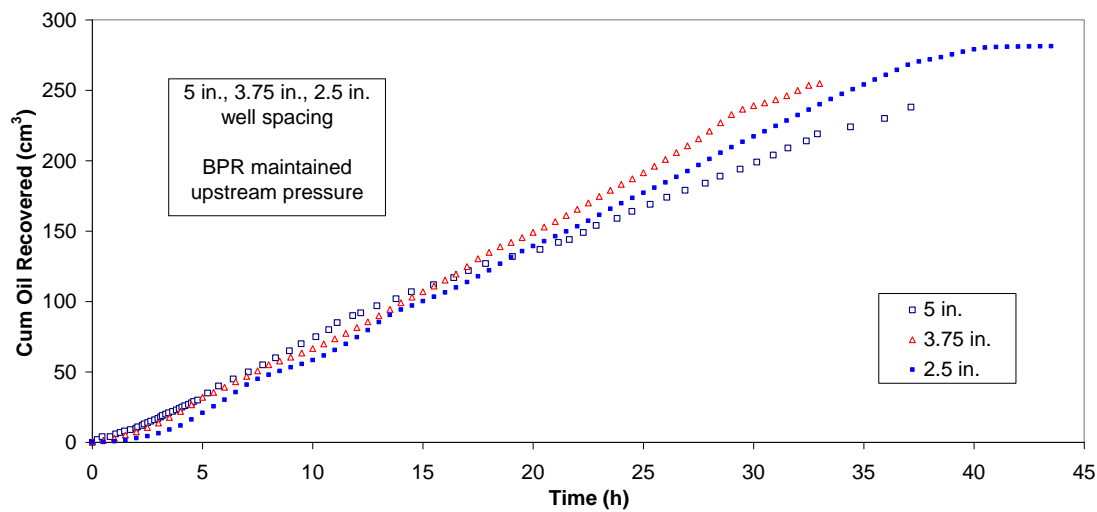
Fig. 27 – Effect of well spacing on oil recovery in VAPEX experiments

Two separate tests were conducted in which the wells were spaced 5 and 10 inches apart using the steel cylinder and ISCO 500D pump for collection in lieu of the BPR (**Fig. 28**). Oil recovery was higher for the 10 in. spacing (~232 cm^3) than the 5 in. spacing (~208 cm^3). The apparent "stepping' trend in the data is a result of the ISCO pump maintaining the upstream pressure by withdrawing small volumes periodically.
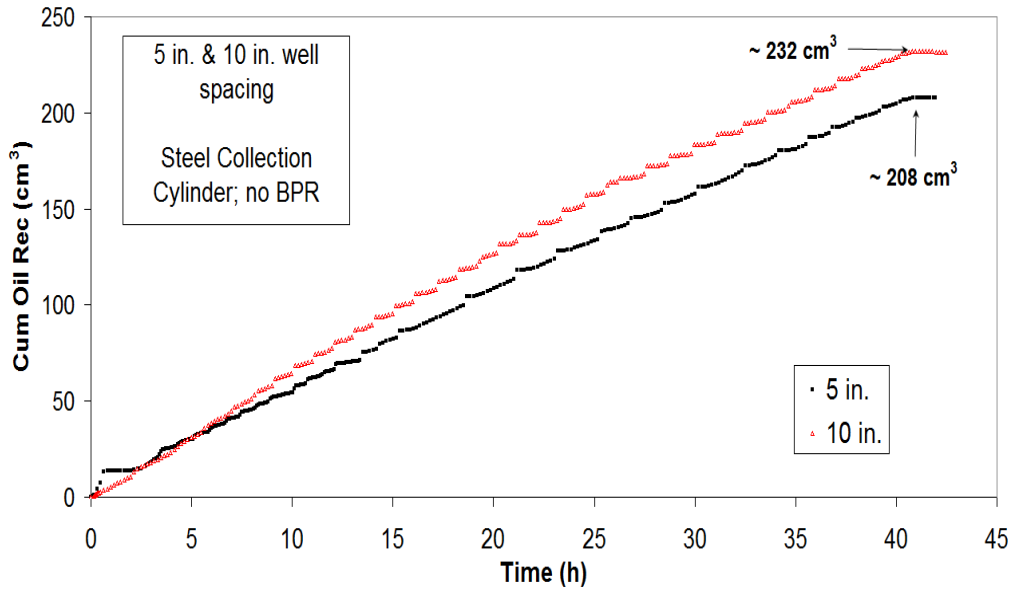
Fig. 28 – 5 in. vs. 10 in. spaced wells in VAPEX

Simulated oil recovery for the 5 in. and 10 in. case produced with the numerical model supports the experimental results, as shown in **Fig. 29**. Because oil production rate is a strong function of pressure in these runs, any difference in pressures between simulation and experiment would result in a significant difference in oil recovery between the two. The overall match is reasonable and so in-situ saturations and concentrations estimated by numerical calculation are thought to be accurate. One obvious difference is that the oil rate seems to decrease towards the end of the simulation in both cases, while the experimental oil rates seem to be relatively constant for the same times. This is because the simulated solution could not entirely capture the flowing/shutting-down action of the experimental collection system. Pressure drop at the end of the experiment are higher than those predicted by the numerical solution after ~25hrs. As the solvent front approaches the producer in the simulation, pressure drop decreases and the oil rate begins to drop off.
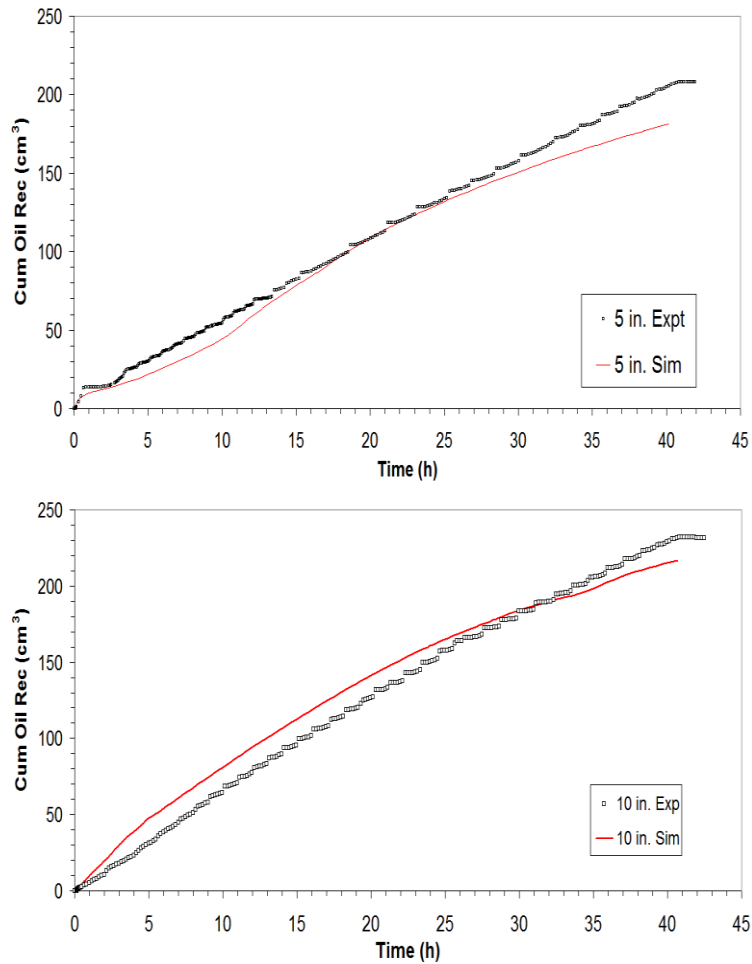
Fig. 29 – Simulated vs. experimental oil recovery in VAPEX

Fig. 30 shows the simulated solution of oil saturation and solvent mole fraction in the oil

phase at ~0.50 pore volumes injected for the 10 in. and 5 in. cases. These results indicate

that oil saturation and solvent mole fraction in the oil phase is higher for the 10 in. case.

This is partially due to a larger volume of oil between the injector and producer when the

wells are spaced further apart. A larger pressure drop, which was also observed in the

experiments, is responsible for a larger oil rate when comparing the two cases. Solvent

mole fraction reaches a value of ~35mol% in grids where the gas saturation is > 50% and

drops off quickly moving in the direction of increasing oil saturation. If this solution is

close to the real solution (i.e. experiment) then dispersion effects are very small and the gradient between solvent and oil phase is quite sharp.
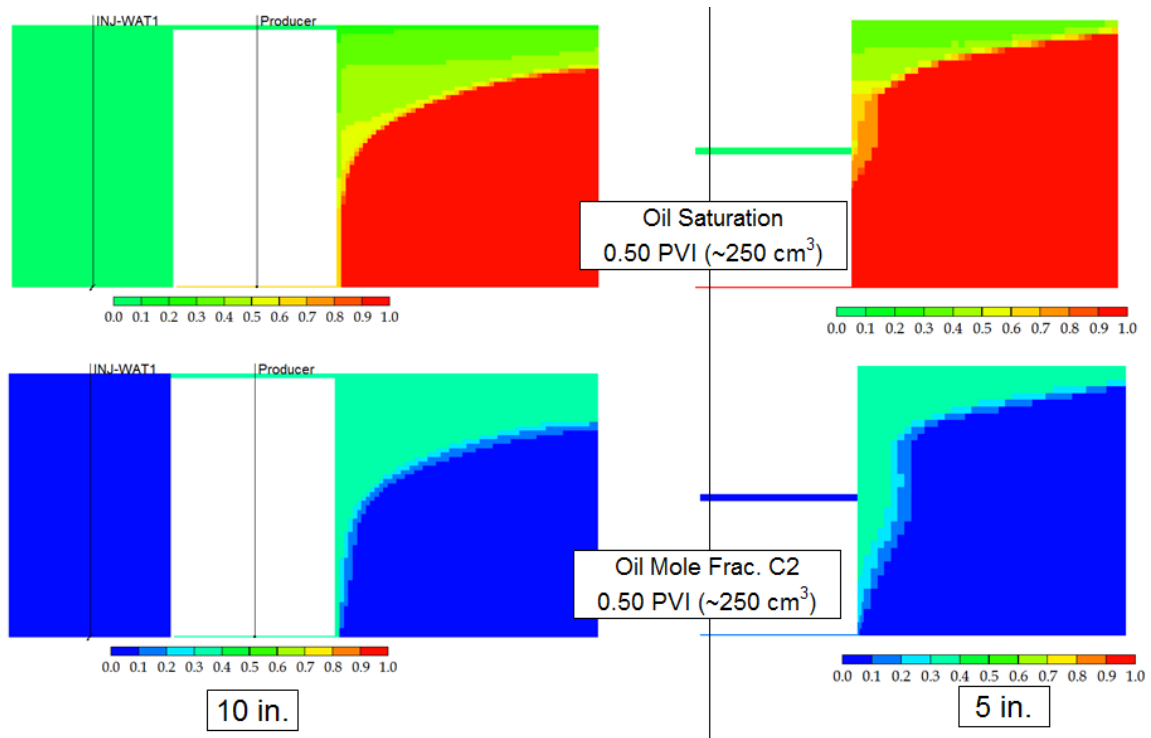
Fig. 30 – In-situ oil saturation; solvent mole fraction in oil in VAPEX

Fig. 31 shows how the inlet and differential pressures varied during the 10 in. VAPEX experiment. The up and down behaviour was influenced by the pressure maintenance pump (ISCO 500D) as it adjusted to maintain the upstream pressure.
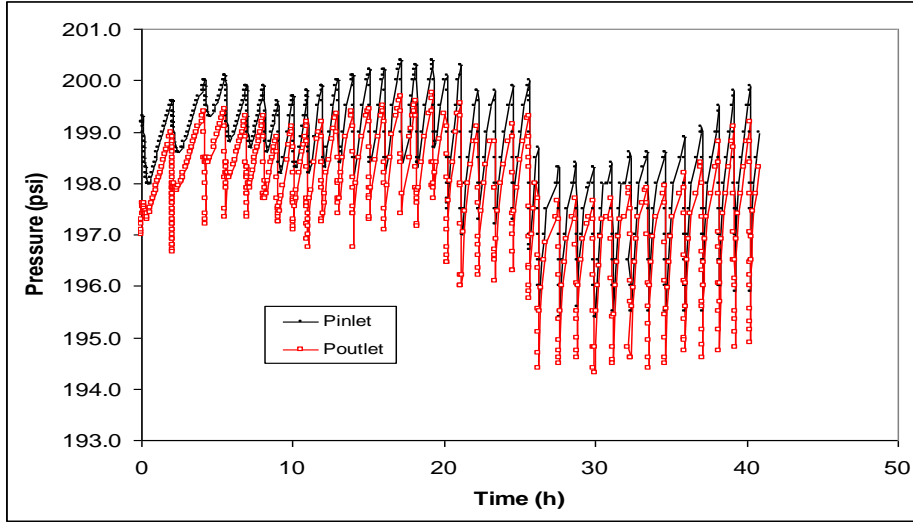
Fig. 31 – Injector and producer pressures in VAPEX: 10 in. run

Effect of Injected Solvent Composition

Effect of injected solvent composition was tested by injecting pure C1, pure C2 and a

50/50 mixture (by volume) of C1 and C2. The C1 injection run was conducted using the

BPR; C2 and C1/C2 runs were performed using the steel collection cylinder. As

mentioned above, the BPR could not maintain pressure as well as the steel cylinder and

so the oil rate at the producer was not as steady for the C1 run. **Fig. 32** shows the oil

recovery for the three cases. The C2 run is the same as the one shown in Fig. 29 as black

squares. Oil production rate in C1 run (red squares) was nearly identical to the other two

runs for about 30 mins, but remained high after the rates for C2 and C1/C2 mixture

dropped off. This is because the BPR could not restrict flow as the solvent phase reached

the outlet of the cell and oil and gas were produced at a high rate until about 1 hour. The

solvent cylinder is directly connected to the BPR at this point and steadily depressurizes.

Eventually, inlet pressure and pressure drop are low enough for oil to move into the flow

66

path between injector and producer and cuts-off the free-flowing gas. Production rate decreases, as shown in Fig. 32 while oil is flowing and solvent pressure at the inlet increases as the piston compresses the gas in the piston cylinder. This cycle of depressurization and repressurization occurs about once per hour for the remainder of the experiment, resulting in a fairly steady overall oil rate. Because the solvent front repeatedly reaches the producer, it is thought that pressure drop becomes lower towards the middle of the run (i.e. ~22hrs) and so oil rate begins to decrease. From about 32 hours to 41 hrs, only about 10 cm^3 of oil was produced in the C1 run. Overall, oil recovery seemed to be more sensitive to the pressure gradient and outlet pressure than the composition of the injected solvent.
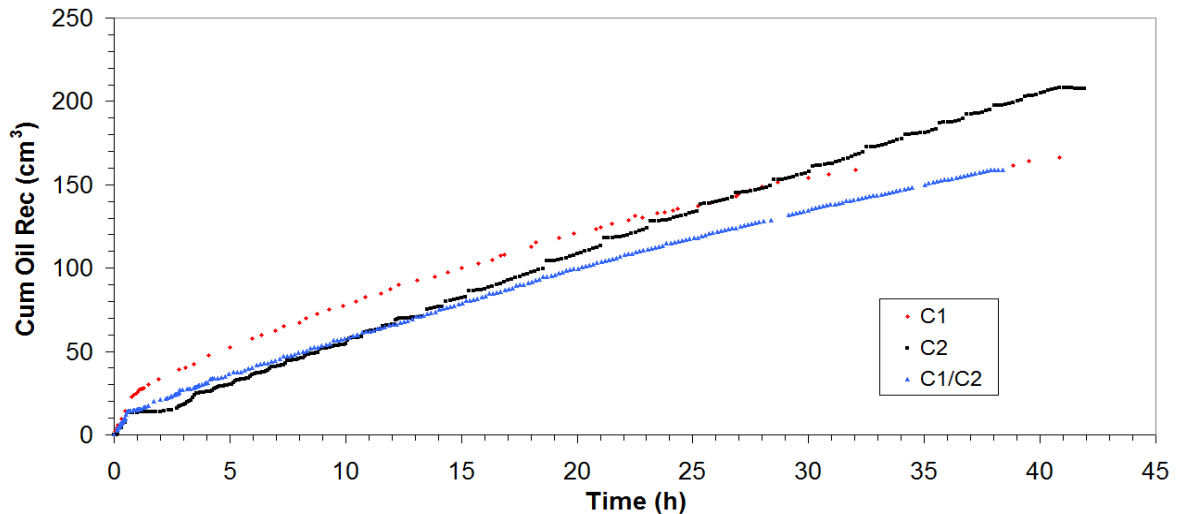
Fig. 32 – Effect of injected solvent composition in VAPEX

These data (**Fig. 32**) have been verified with a numerical model. Runs in which C1 and a 50/50 C1/C2 molar mixture are injected were conducted. **Fig. 33** shows the results of

those runs. Simulated oil recovery in the C1 injection case matches the experimental oil production rate fairly well for the majority of the run. The high experimental oil rate in the beginning of the test (up to ~2 hrs) is due to poor management by the BPR, which made simulating the outlet boundary condition problematic. So less oil production is predicted by the simulator up to this point. From then on, the slope of oil recovery with time or oil rate, are very similar for experiment and simulation. The second plot in **Fig. 33** compares the numerically predicted oil recovery with experimental. Because the outlet boundary condition (BHP) was better managed with the collection cylinder during the test, it was easier to simulate the outlet pressure in this simulation run. Oil recovery seemed to match more closely here. Simulation results for the C2 injection experiment are still pending.
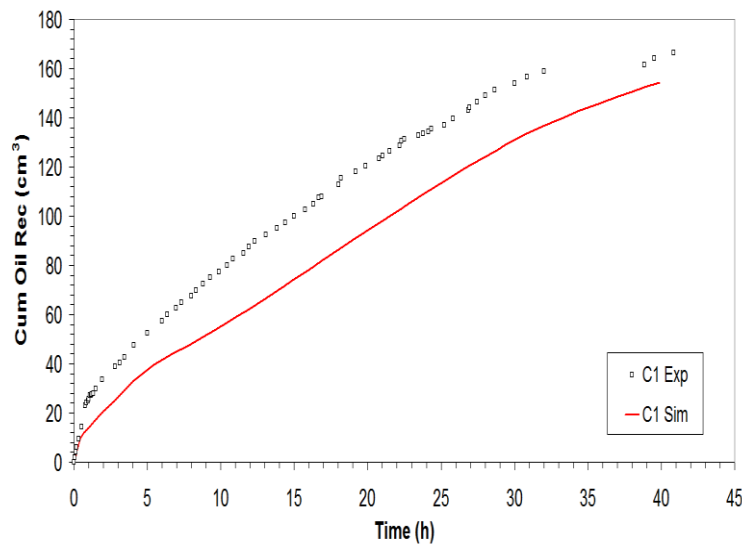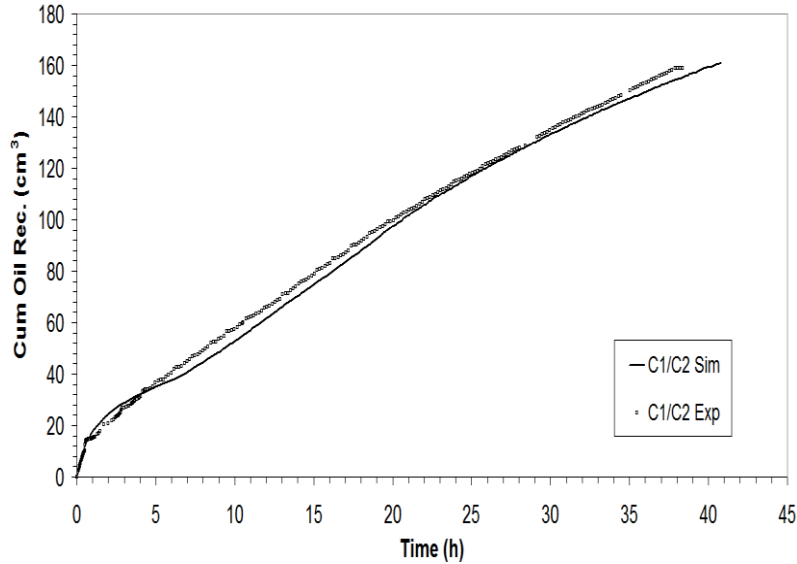
Fig. 33 – Simulated vs. experimental recovery in VAPEX: C1 and C1/C2 injection

Field-Scale Gas Injection Simulation by Streamline Simulator

Gas injection is simulated on a quarter of a five spot pattern and vertical (X-Z) cross-sections. Both homogeneous and heterogeneous permeability fields are generated for the purpose of simulation. The permeability is 300 md in the homogeneous permeability field used in the simulations. Heterogeneous permeability fields are generated by unconditional Gaussian simulation using GSLIB. The X-Y heterogeneous permeability field is shown in **Fig. 34** and referred to as Perm1. Permeability values vary from 20 md to 2000 md with a mean of 844 md and standard deviation of 52 md. The X-Z heterogeneous permeability field is shown in **Fig. 35** and referred to as Perm2. Permeability variation is from 10 md to 998 md with a mean of 165 md and standard deviation of 44 md. Injector and producer bottom hole pressures are kept constant in these simulations.

69
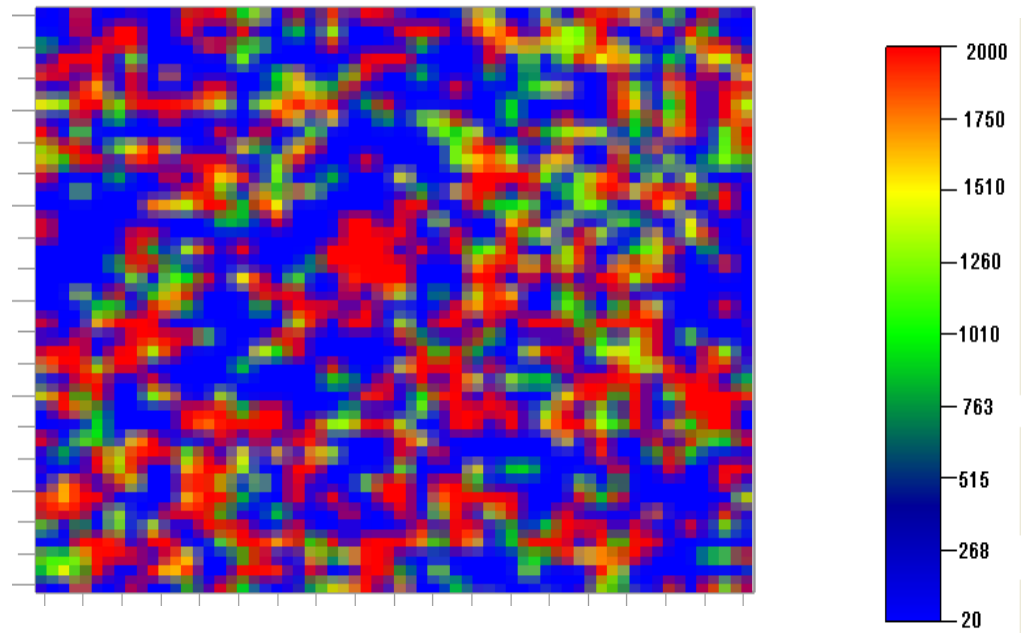
Fig. 34 - Heterogeneous permeability field (X-Y): Perm1
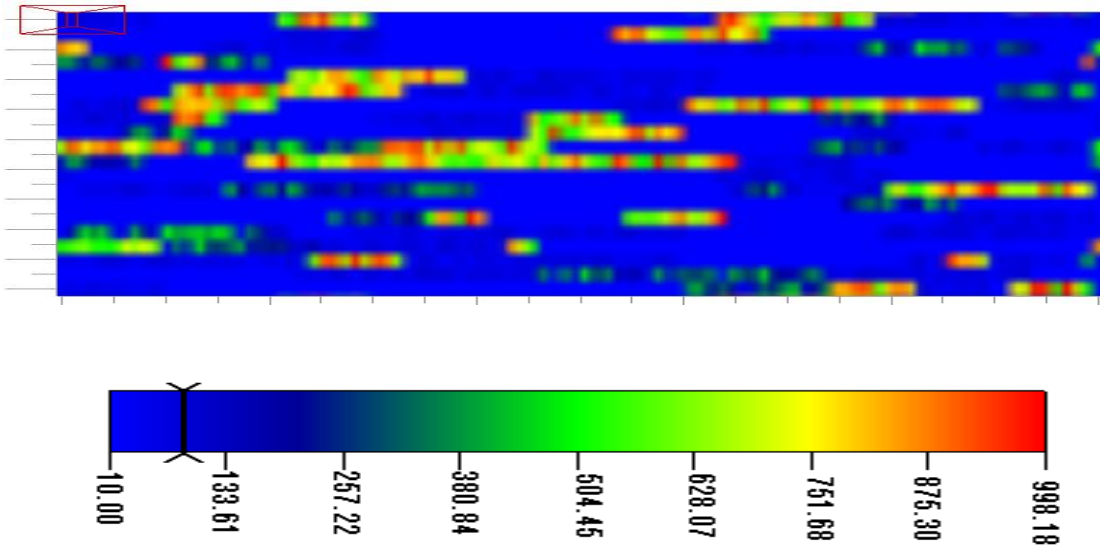
Fig. 35 - Heterogeneous Permeability field (X-Z): Perm2

Oil and solvent compositions are chosen to illustrate two-hydrocarbon and three-hydrocarbon phase behaviors. Simulations with two-hydrocarbon phase behavior are performed with a reservoir oil (called Oil 1) described in Table 6. Component properties used in the simulation are listed in Table 7. Four pseudo-components are used to represent the oil with a viscosity of 1 cp by a Peng-Robinson equation of state. It mainly consists of hexane and C14+ components. Critical volumes of a few components are adjusted to attain the desired oil viscosity. Two solvents have been used. Solvent I is 90:10 mixture of methane and propane (immiscible solvent) and solvent II is 52:48 mixture of methane and propane (multicontact miscible solvent).

Component Name	Mole Fraction
Methane	0.199
Propane	0.001
Hexane	0.40
C14- C19	0.40

Table 6 - Compositional description of Oil 1 used in two HC phase simulations

Component Name	P_c (psi)	T_c (R)	V_c (ft^3/lbmol)	MW	ω (accentric)
Methane	667.80	343.37	1.66	16.04	0.01150
Propane	616.30	666.01	3.35	44.10	0.1524
Hexane	438.77	913.33	5.29	86.00	0.3013
C14- C19	203.91	1346.89	20.94	223.51	0.5768

Table 7 - Component properties used for fluid description of Oil 1

For three hydrocarbon phase simulations, oil composition is approximated by twelve pseudo-components, called the Oil 2. The composition of Oil 2 is shown in Table 8; it consists of mainly methane, and C9+ fractions. Table 9 lists properties of all the components used in simulation. The oil viscosity is set to 1 cp by adjusting critical volumes. Two different solvents: solvent III (100 % CO_2) and solvent IV (75 % CO_2 – 25 % NGL) are used in these simulations. The composition of NGL is listed in Table 10.

Component Name	Mole Fraction
Carbon Dioxide (CO$_2$)	0.000436
Methane (C1)	0.272148997
Ethane (C2)	0.004128
Propane (C3)	0.010484
Butane (C4)	0.021229999
Pentane (C5)	0.020020001
Hexane (C6)	0.022566
C7-C9	0.098746002
C10-C13	0.100533001
C14-C19	0.145137995
C20-C35	0.164159
C36 +	0.140411005

Table 8 - Compositional description of Oil 2 used in three HC phase simulations

Component Name	P_c (psi)	T_c (R)	V_c (ft3/lbmol)	MW	ω
CO_2	1071.60	547.57	0.416	44.01	0.2250
C1	667.80	343.04	1.602	16.04	0.0130
C2	707.80	549.76	2.451	30.07	0.0986
C3	616.30	665.68	3.300	44.10	0.1524
C4	550.70	765.32	4.088	58.12	0.2010
C5	488.60	845.37	4.946	72.15	0.2539
C6	483.77	923.00	5.296	84.00	0.2583
C7-C9	415.41	1040.29	8.551	145.16	0.3165
C10-C13	255.39	1199.64	13.115	223.26	0.4255
C14-C19	203.91	1346.56	23.070	353.51	0.5768
C20-C35	158.03	1532.74	33.256	554.55	0.7659
C36 +	94.80	1967.34	44.579	1052.00	1.1313

Table 9 - Component properties used for fluid description of Oil 2.

Component Name	Composition
Propane (C3)	0.0439
Butane (C4)	0.4337
Pentane (C5)	0.2543
Hexane (C6)	0.1198
C7-C9	0.1483

Table 10 - Composition of NGL (Natural Gas Liquid)

Two Hydrocarbon phase system

1- D Gas Injection

One-dimensional simulations are performed with 100 grid blocks in the x-direction to investigate the phase behavior of solvents with reservoir oil 1 and determine the

minimum miscibility enrichment (MME) of methane with propane. Solvent composition is varied and recovery at 1.2 PV is plotted, as shown in Fig. 36. Below 40 % propane in the solvent, the oil recovery falls sharply as the propane enrichment is reduced, as shown in Fig. 4. The minimum miscibility enrichment (MME) of methane with propane is ~40 %. In situ oil saturation distribution is shown in Fig. 37 for two solvents. Note that immobile water saturation of 0.2 is present in all grid blocks. Fig. 37 indicates that 90 % C1-10 % C3 is immiscible and 52 % C1-48 % C3 is multi-contact miscible with the reservoir oil 1.
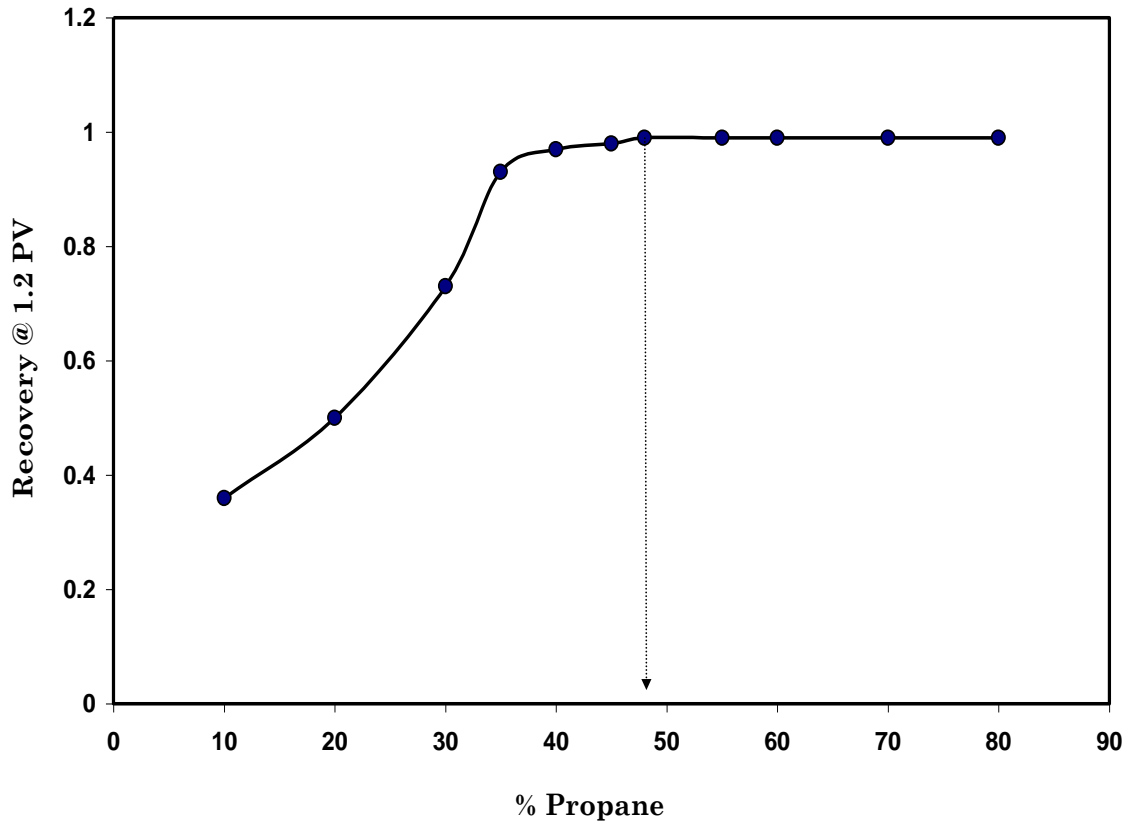
Fig. 36 - Minimum miscibility enrichment (MME) of methane with propane (Oil 1)
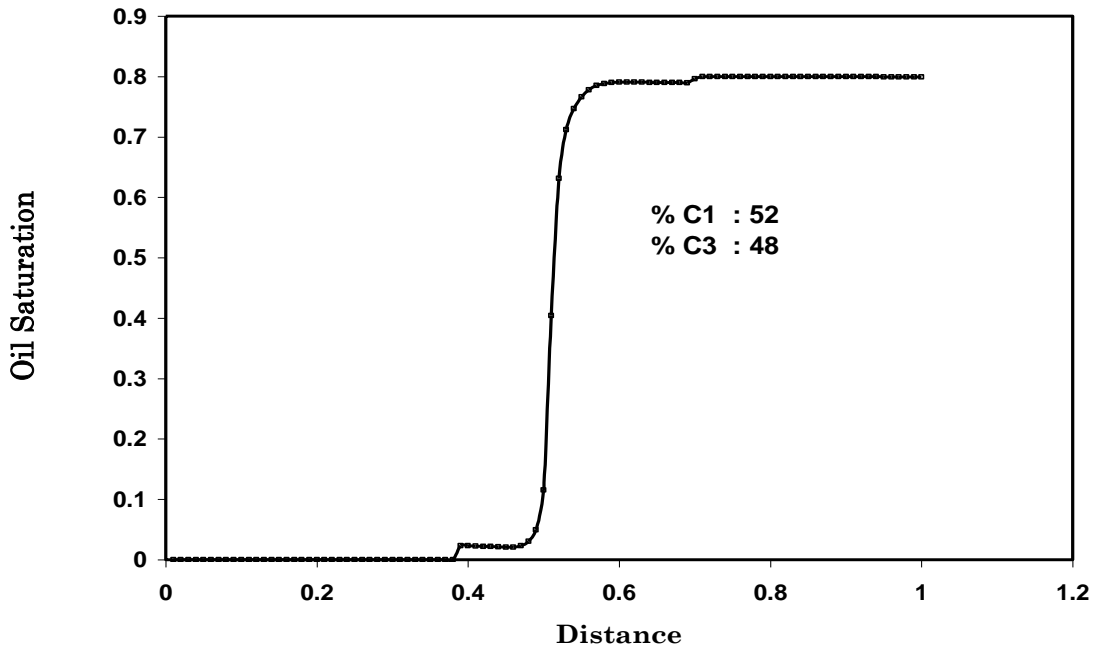
Fig. 37a - Oil saturation distribution in 1-D miscible gas injection (with Oil 1)
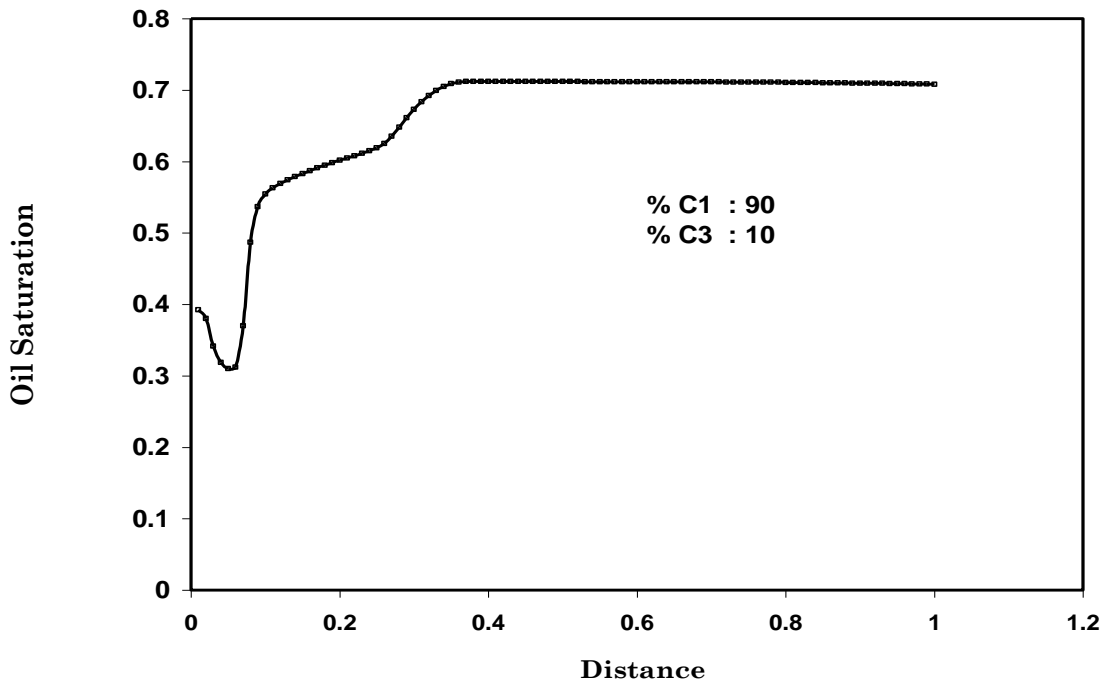
Fig. 37b - Oil saturation distribution in 1-D immiscible gas injection (with Oil 1)

2-D Gas Injection (X-Y Cross-section)

2-D field-scale gas injection simulations are performed on a quarter 5-spot pattern. Simulation model consists of 40 * 40 * 1 cartesian grid blocks with one injector well and one producer well. Homogeneous and heterogeneous (Perm1) permeability fields are used for these field-scale simulations. Both the injector and producer wells are set at constant bottom hole pressures of 1800 psi and 1100 psi, respectively, i.e., pressure drop between the two wells is kept constant. Initial reservoir pressure is 1500 psi with an initial water saturation of 0.2. Simulations are conducted with miscible (Solvent I) and immiscible solvents (Solvent II) at the reservoir temperature of 140 ^{0}F. All the simulation parameters used in the simulation runs are listed in Table 11.

Simulation Parameter	Value
No.of Gridblocks	40 * 40
Grid Size	10 *10 (ft)
No. of Components	4
No. of Streamlines	200
Initial Pressure	1500 (psi)
Injector Well (BHP)	1800 (psi)
Producer Well (BHP)	1100 (psi)
Oil Viscosity	1 (cp)
Initial Oil Sat.	0.8

Table 11 - Simulation parameters for 2-D gas injection (X-Y)

Fig. 38 shows the pressure profile at 0.10 PV injected as predicted by streamline simulator and finite difference simulator. Pressure contours are not circular because of the heterogeneous permeability field of Perm 1. It can be observed that the most of the pressure drop is near the production well because of the converging flow of the viscous oil towards the production well. Fig. 39 compares the concentration profile of methane at 0.10 PV injected as predicted by streamline simulator and finite difference simulator.

There are slight differences in the concentration contours, but in general results from both the simulators are in good agreement. Oil saturation maps are also compared in Fig. 40 at different time instants. Fluids follow the path of high permeability streaks resulting in unsymmetric and wavy fronts. Oil saturation profile clearly shows that heterogeneity is an important factor that affects the sweep efficiency of any process. Viscosity ratio (oil to gas viscosity) is another important factor in determining the sweep efficiency of displacement. The high viscosity ratio between oil and gas along with permeability heterogeneity leads to the formation of viscous fingers along high permeability channels and adversely affects the areal sweep. Simulations are conducted with different oil viscosities to understand the formation and propagation of these viscous fingers in gas injection process. Oil viscosity is varied by adjusting the critical volumes without altering the phase behavior of the fluid system. Fig. 41 shows the methane concentration distribution for three different oil viscosities at 0.16 PV injected during a continuous gas injection. Severity of viscous fingering increases as the oil viscosity is increased. Better areal sweep can be observed for 1 cp oil as compared to 15 cp oil.

Streamline   Finite Difference

1250   1130   1380   1450   1520   1590   1660   1730   1800
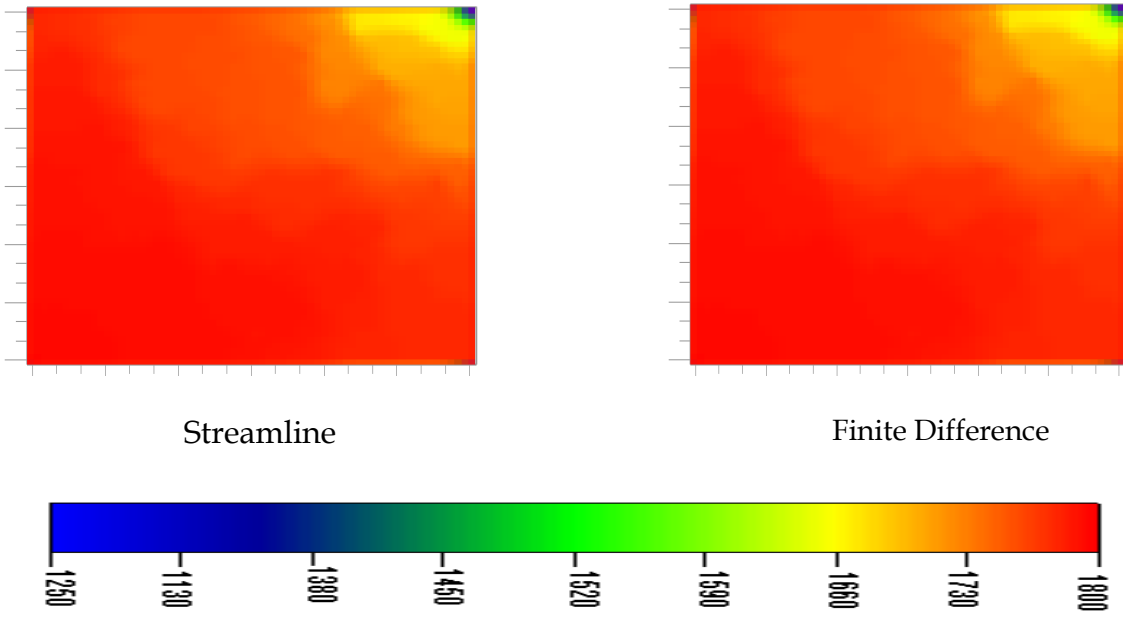
Fig. 38 - Pressure contours @ 0.10 PVI for 2-D (X-Y) gas injection - heterogeneous
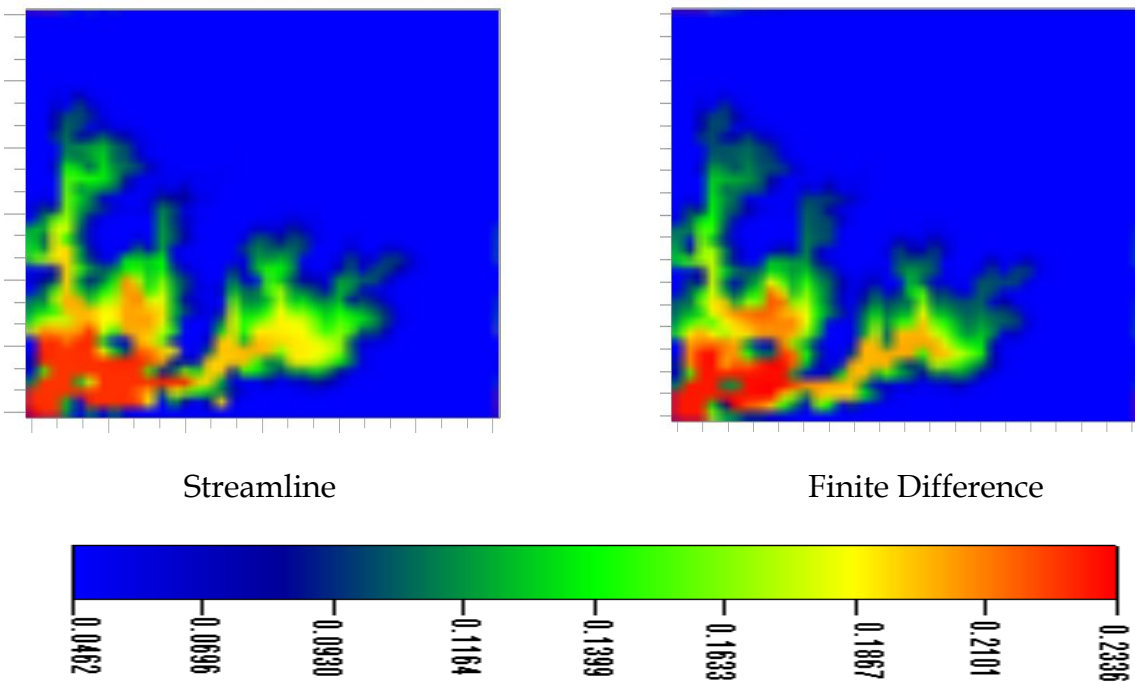
Streamline   Finite Difference

0.0462   0.0696   0.0930   0.1164   0.1399   0.1633   0.1867   0.2101   0.2336

Fig. 39 - Methane concentration @ 0.10 PVI for 2-D (X-Y) gas injection - heterogeneous

Streamline @ 0.05 PVI

Finite Difference @ 0.05 PVI

Streamline @ 0.10 PVI

Finite Difference @ 0.10 PVI

Streamline @ 0.17 PVI

Finite Difference @ 0.17 PVI
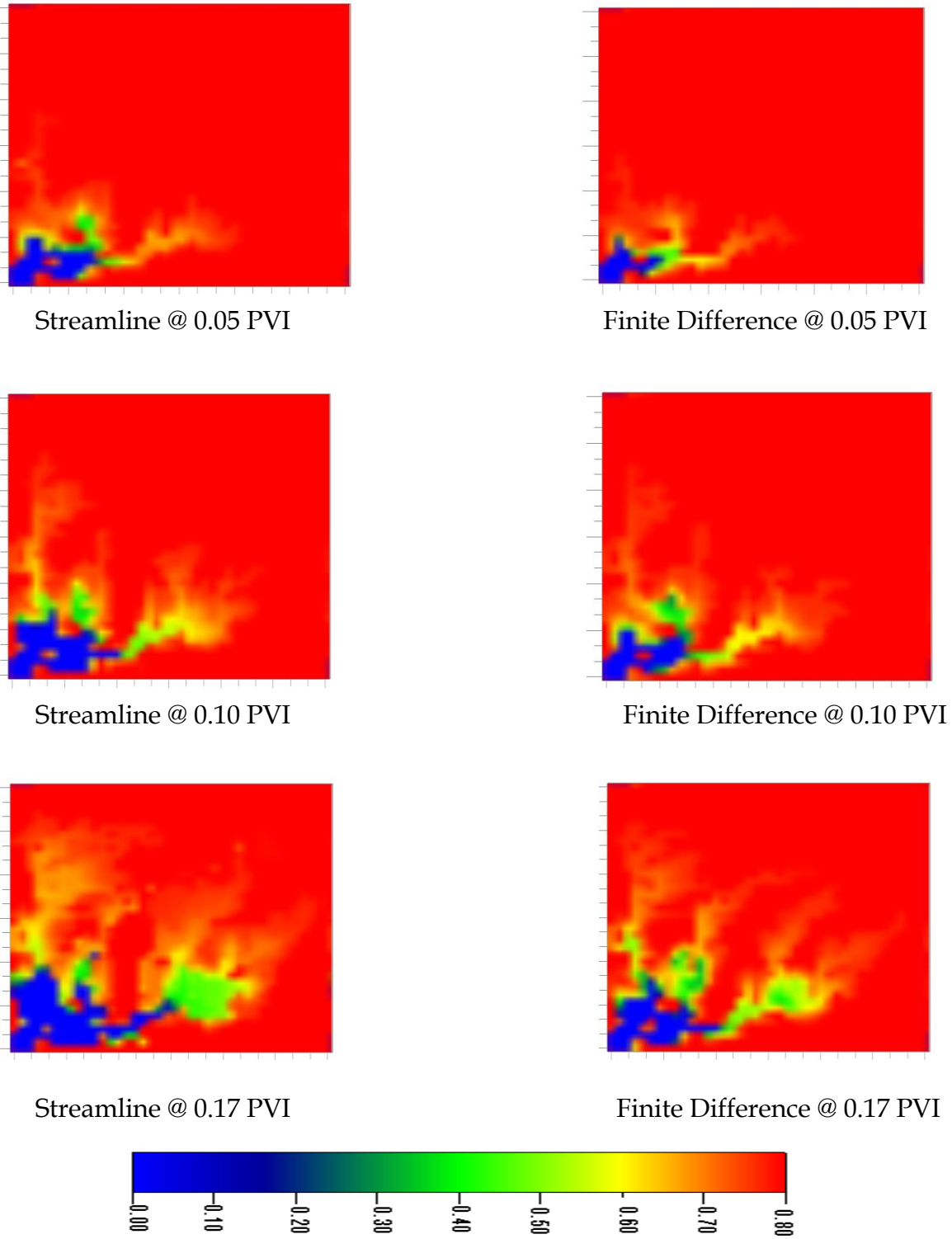
Fig. 40 - Oil saturation distribution for 2-D (X-Y) gas injection - heterogeneous

Oil Viscosity (1 cp)

Oil Viscosity (5 cp)
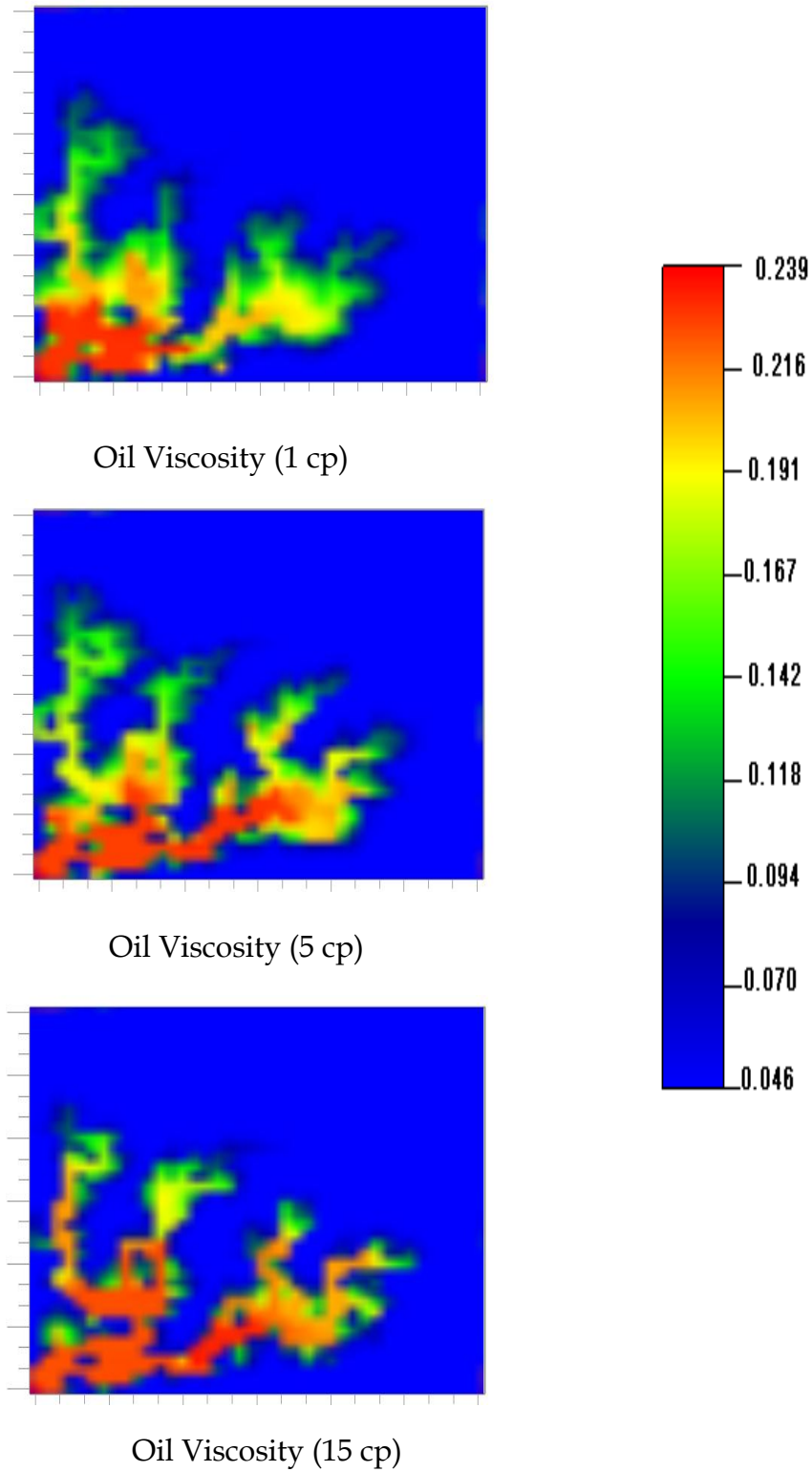
Oil Viscosity (15 cp)

Fig. 41 - Methane concentration @ 0.16 PVI for 2-D (X-Y) gas injection: effect of oil
viscosity
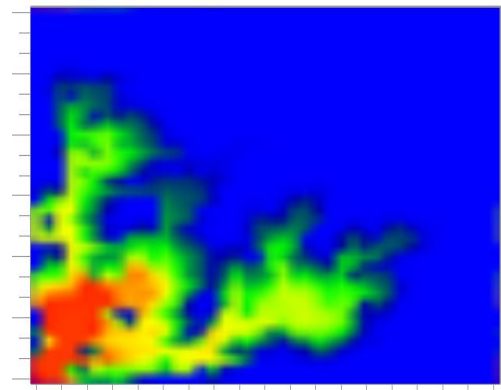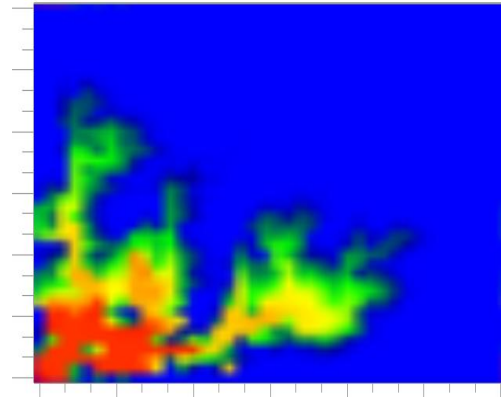
300 Streamlines
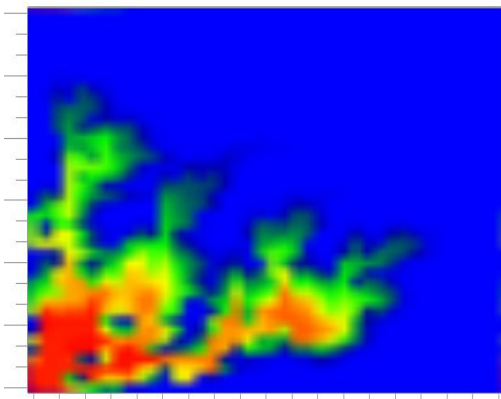
500 Streamlines

Fig. 42 - Methane concentration @ 0.10 PVI for 2-D (X-Y) gas injection: effect of number of streamlines launched

Influence of number of streamlines

Largest computational cost in compositional streamline simulation is associated with the flash calculations at the streamline grid points which increase with the number of streamlines. Therefore optimum number of streamlines should be launched to represent the flow in the reservoir. Simulations are conducted with the same test model as described in the previous example, but streamline density is varied. Three cases are considered in which 200, 300, and 500 streamlines are launched from the injector well to study the effect of streamline density on the resolution of saturation/concentration profiles. Methane concentration profile is plotted for all three cases at 0.10 PV injected as shown in Fig. 42. The results from these simulations look similar with minor differences.

Effect of numerical dispersion

For accurate prediction of in-situ saturation profiles with minimal numerical dispersion, higher order numerical schemes are implemented in the streamline simulator and tested for different scenarios. Two different test cases are considered with homogeneous and heterogeneous permeability field (Perm1). For the homogeneous permeability field, a permeability of 300 md is used in the simulation. All the simulation parameters are listed in Table 11. Both miscible (solvent I) and immiscible (solvent II) solvents are used as injectants to study the effect of miscibility behavior on numerical dispersion. Fig. 43 shows the oil saturation profile at 0.16 PV, injected as predicted by streamline simulator and finite difference simulator for miscible gas injection simulation with solvent I in a homogeneous five spot pattern. Saturation contour is nearly flat in the case of streamline simulation with the use of single point upstream weighting scheme (SPU). The saturation distribution derived from finite difference simulation shows a concave trend, which is

inconsistent with the velocity and pressure field. This unusual trend obtained with SPU scheme is a consequence of the high degree of numerical dispersion due to truncation errors in single point approximation. This truncation error feeds into the flash calculation (which is performed every local time step) and alters the composition path. This effect is more prominent in miscible displacements than immiscible displacements particularly near the displacement fronts. The oil saturation distribution as predicted by streamline simulation with the use of higher order TVD schemes is more accurate and consistent with the velocity contours. Displacement front is circular (away from injection well) as expected, due to reduced numerical dispersion in the TVD schemes by addition of anti-diffusion term, which cancels the effect of local truncation error to some extent. Saturation map predicted by finite difference simulator with TVD scheme still shows considerable amount of numerical dispersion.
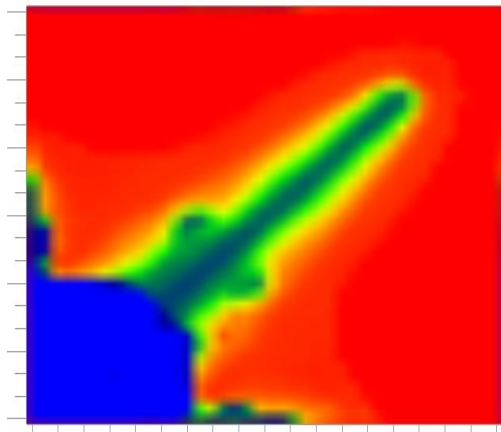
Streamline - TVD
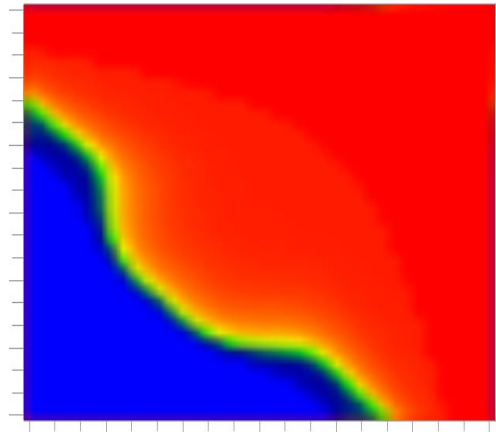
Streamline - SPU
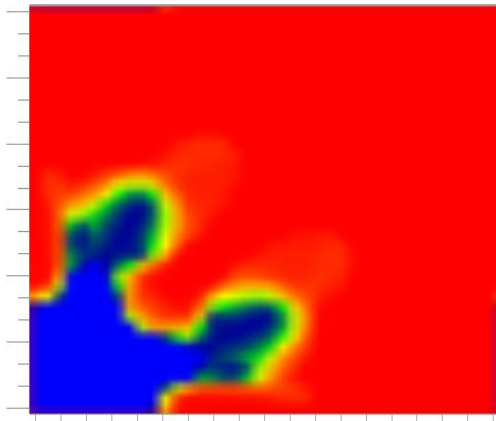
Finite Difference - TVD
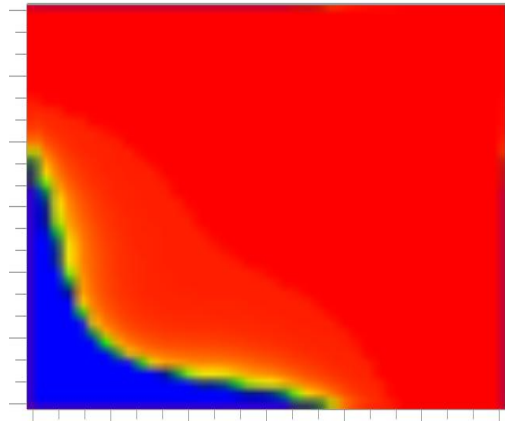
Finite Difference - SPU
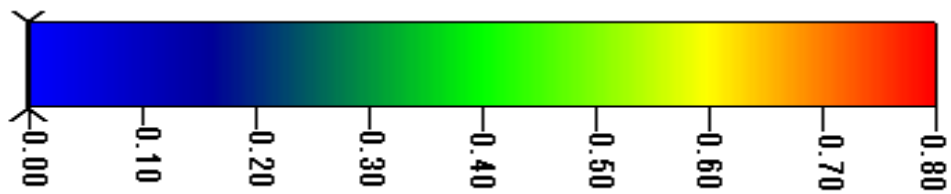
Fig. 43 - Comparison of oil saturation contours @ 0.16 PVI in homogeneous 2-D

(X-Y) *miscible* gas injection simulation: effect of numerical schemes

Streamline - SPU

Streamline - TVD

Finite Difference - SPU

Finite Difference - TVD

0.272 0.338 0.404 0.470 0.536 0.602 0.668 0.734 0.80
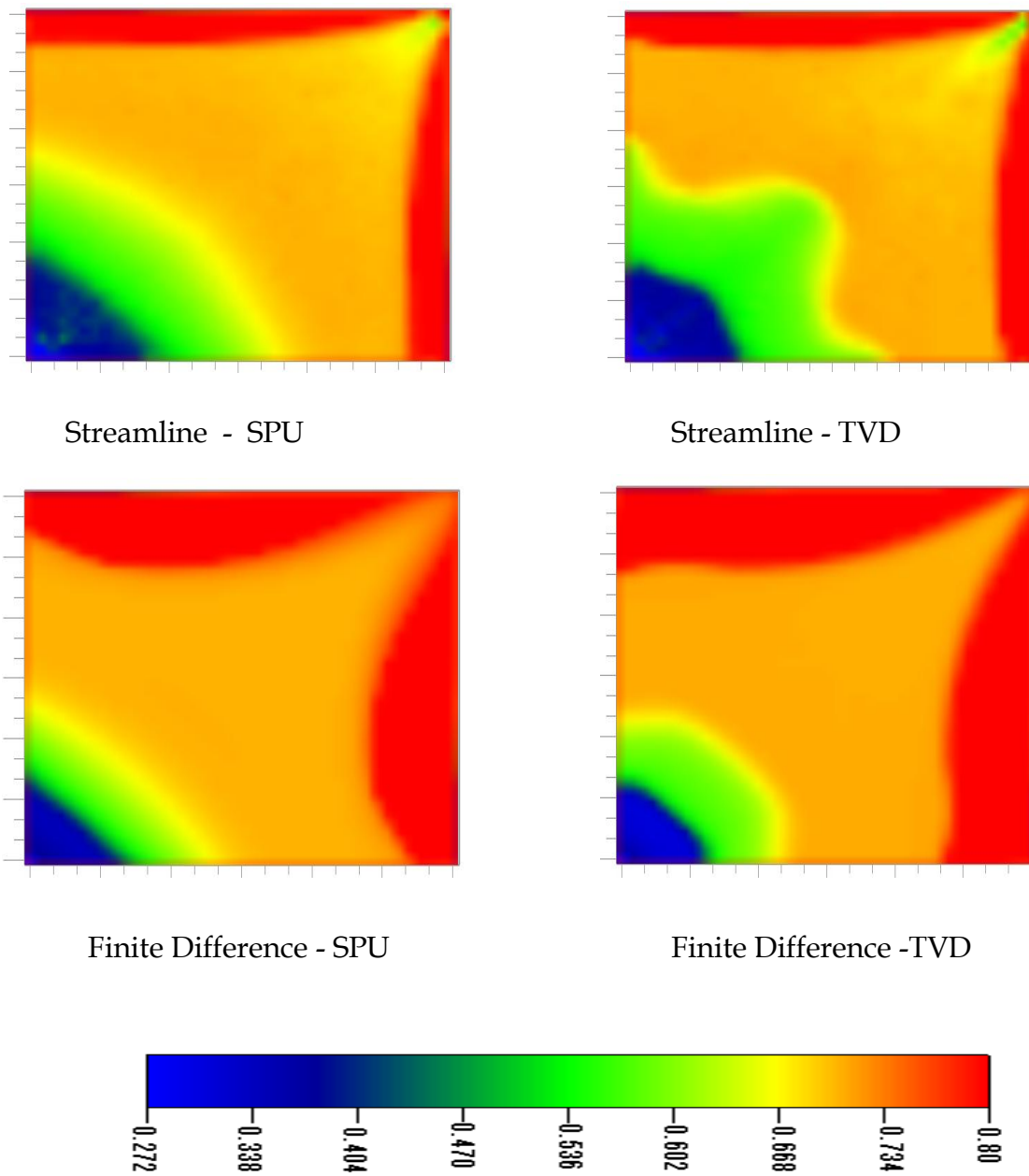
Fig. 44 - Comparison of oil saturation distribution @ 0.17 PVI in homogeneous 2-D

(X-Y) *immiscible* gas simulation: effect of numerical schemes

Streamline (SPU)   Streamline (TVD)

0.046 0.069 0.093 0.117 0.141 0.164 0.188 0.212 0.236
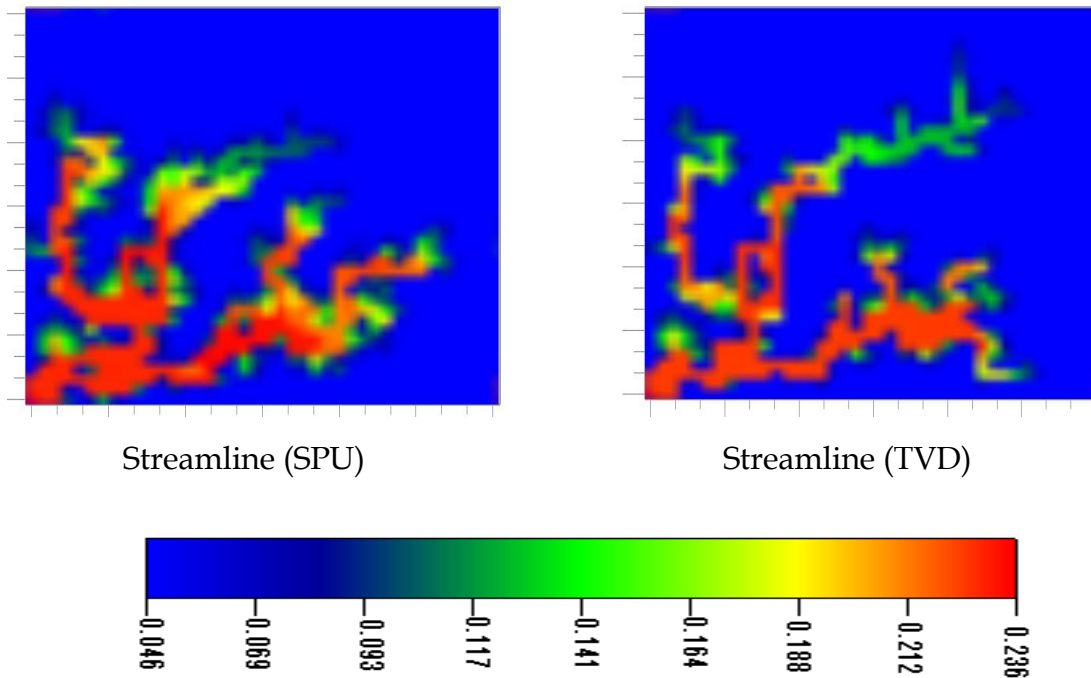
Fig. 45 - Comparison of methane concentration distribution @ 0.20 PVI in

2-D (X-Y) heterogeneous miscible gas simulation: effect of numerical schemes

To further emphasize the effect of numerical dispersion with the use of lower order numerical schemes, an immiscible displacement is simulated with solvent II in a homogeneous quarter five spot pattern. Oil saturation contours at 0.17 PVI injected are shown in Fig. 44 and compared with those from the finite difference simulations. The shape of saturation profile obtained with SPU scheme in streamline simulation shows a slight upward curve (convex) as compared to the one obtained with finite difference simulation which is flat near the injection well. Again the use of higher order TVD scheme results in more accurate description of saturation distribution. Although there is some inconsistency in the saturation maps obtained with the SPU scheme in the immiscible case, it is still less diffused and more accurate when compared with the saturation fronts obtained during miscible injection with the SPU scheme.

Another simulation run is conducted with heterogeneous permeability distribution (Perm1). Solvent I is injected into the reservoir oil 1. Oil viscosity is increased to 15 cp by adjusting critical volumes of few components. Methane concentration profile at 0.20 PVI are shown in Fig. 45. As expected, results predicted by the TVD scheme produces less numerical dispersion compared to the SPU scheme. Sharp and less diffused viscous fingers are captured more accurately with the use of the higher order TVD scheme.

2-D Gas Injection (X-Z Crossection)

Homogeneous Permeability Field

1600 grid blocks are used in a Cartesian X-Z plane with 80 grids in the X-direction and 20 grids in the Z-direction. A homogeneous permeability field with K_h=300 md and K_v=15 md is used in these simulations. Both injector and producer wells are vertical and set at constant bottom hole pressures of 1800 psi and 1100 psi, respectively. Pressure drop between the two wells is kept constant. Both the wells are completed in all 20 layers. Distance between the wells is 800 ft and thickness of the reservoir is 50 ft. The corresponding gravity number is 0.186. Initial reservoir pressure is 1500 psi with an initial water saturation of 0.20. Solvent I (miscible injectant) is injected into the reservoir with oil 1 (with a viscosity of 1 cp) at the reservoir temperature of 140 ^{0}F. Table 12 lists the details of the simulation model used in the field case study.

Simulation Parameter	Value
No. of Grid Blocks (X-Z)	80 * 20
Grid Size	10 * 2.5 (ft)
Horizontal Permeability (K_x)	300 (md)
Vertical Permeability (K_z)	15 (md)
Injector Well (BHP)	1800 (psi)
Producer Well (BHP)	1100 (psi)
Initial Pressure	1500 (psi)
Reservoir Temp.	140 (^{0}F)
Oil Viscosity	1 (cp)
Initial Oil Saturation	0.8
Initial Water Saturation	0.2
No. of Streamlines	200

Table 12 - Simulation parameters for 2-D gas injection (X-Z)

Fig. 46 shows oil saturation profiles of the X-Z cross-section at different pore volumes of gas injected. Effect of gravity is clearly shown in the contours. Gas, being lighter than oil, moves up as the displacement fronts propagate and forms a gravity tongue. Oil gets displaced miscibly on the top portion of the reservoir. The lower portion of the reservoir is not swept by gas properly; hence the oil recovery is low in the lower portion of the reservoir. This gravity tongue propagates with time and breaks through the production well early, which results in lower sweep and oil recovery. The gravity number, N_g is 0.186 for this example which is in the transition regime between viscous and gravity dominated regimes.

@ PVI = 0.13

@ PVI = 0.25

@ PVI = 0.37

@ PVI = 0.46
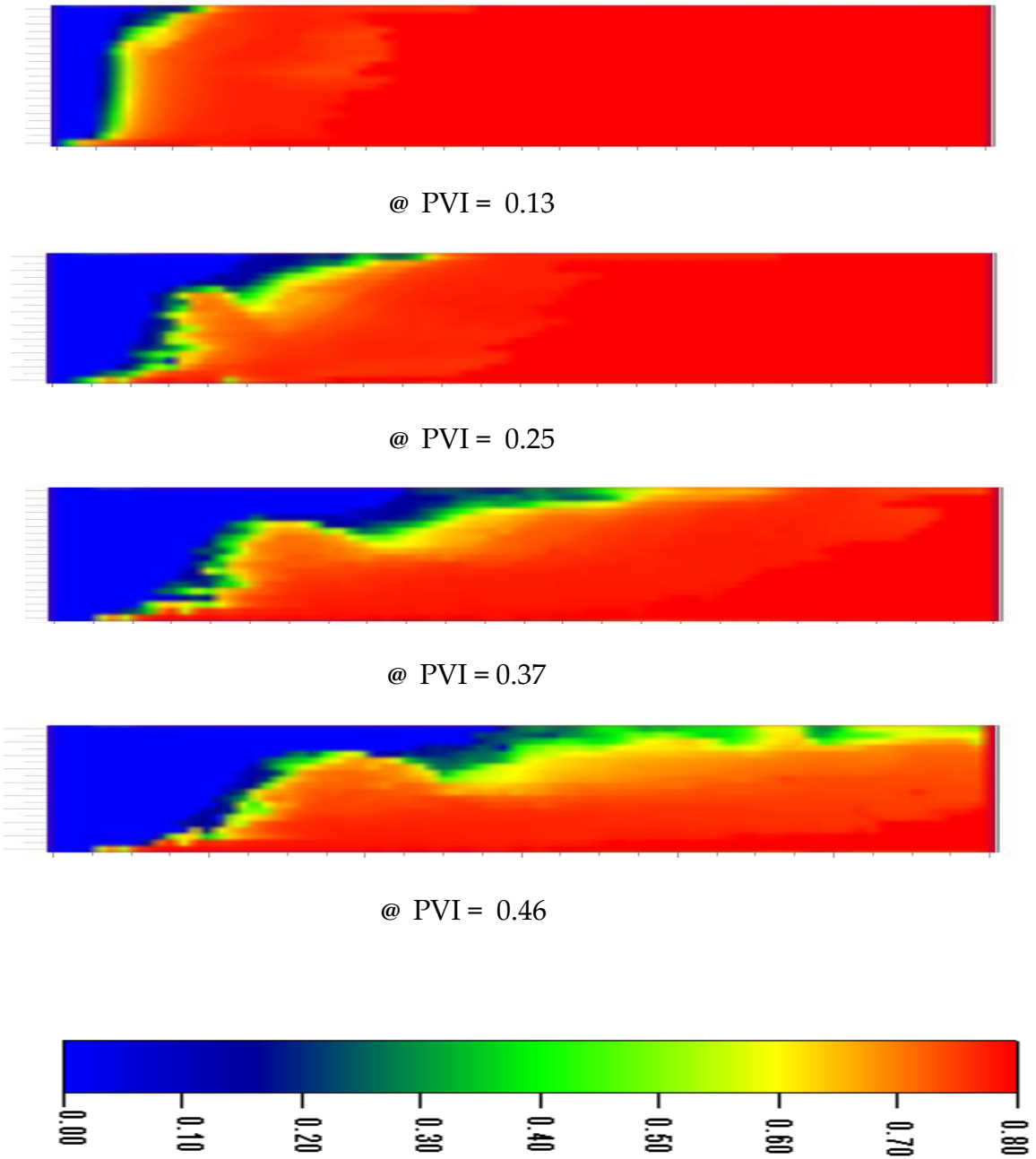
Fig. 46 - Oil saturation profile for 2-D homogeneous (X-Z) gas injection (N_g =0.186)

Sensitivity to number of grids in z direction

Grids = 80 * 10 (X-Z)

Grids = 80 * 20 (X-Z)

Grids = 80 * 40 (X-Z)
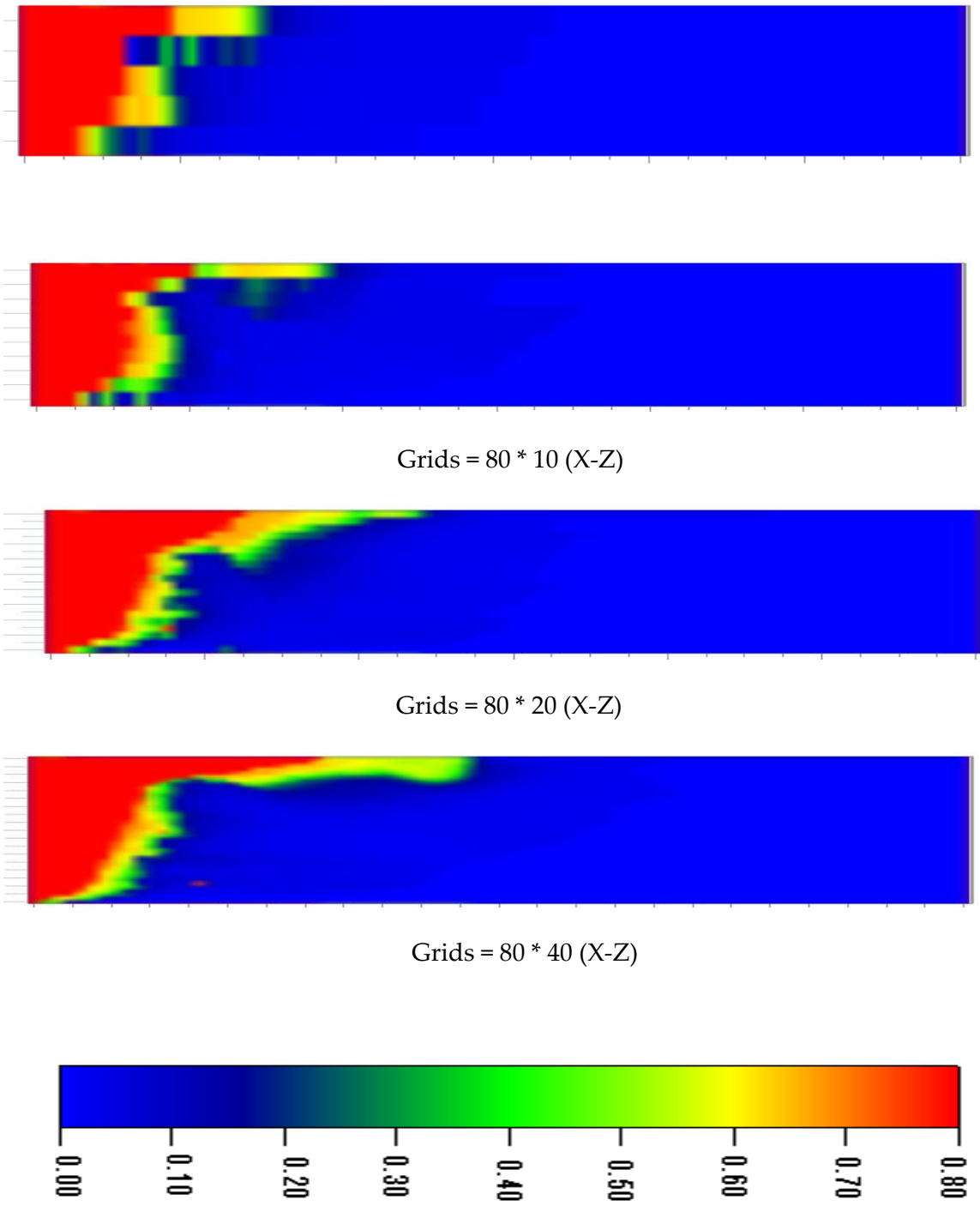
Fig. 47 - Gas saturation profile @ 0.25 PVI for 2-D homogeneous (X-Z) gas injection:
effect of number of grids in the vertical direction (N_g =0.186)

To accurately predict the breakthrough time and capture the formation of the gravity finger, fine gridding is required in the vertical direction. Simulations are conducted by varying the number of grid blocks in z direction to see the effect of numerical dispersion on thickness and resolution of the gravity finger at the top of the reservoir. Four cases with different number of grids (80 *5, 80 *10, 80 *20, and 80*40) are considered. Gas saturation contours are plotted at 0.25 PV of solvent injected as shown in Fig. 47. The difference in saturation contours is due to insufficient resolution of the tongue in the vertical direction. It can be observed that as we increase the number of grid blocks in the vertical direction, shape and position of gravity finger is represented more accurately. Models with only five and ten grids in the z direction fail to capture the shape of the segregated tongue.

Effect of vertical to horizontal permeability (K_v/K_h) ratio

Gravity number, N_g is varied by changing vertical to horizontal permeability ratio (K_v/K_h) and its effect is studied on gravity override. The simulation model used in this study is the same as the one described in the previous example. Horizontal permeability is kept at 300 md. The value of K_v/K_h is set to 0.01, 0.05 and 0.2. The predicted distribution of gas at 0.37 PVI for all the three cases is shown in Fig. 48. As the ratio of vertical to horizontal permeability is increased from 0.01 to 0.2, N_g varies from 0.037 to 0.74 and gravity forces become more dominant. It is observed that gravity segregation is most prominent in the third case with K_v/K_h equal to 0.2 ($N_g = 0.74$) while not much effect of gravity override is observed in the first case with K_v/K_h equal to 0.01 ($N_g = 0.037$).

91
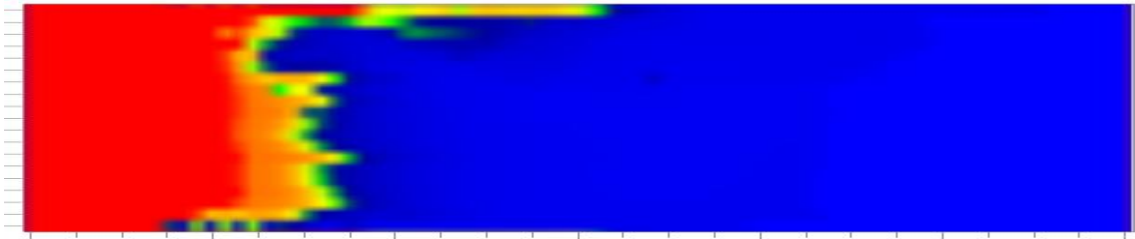
$K_v /K_h =0.01$ $(N_g =0.037)$
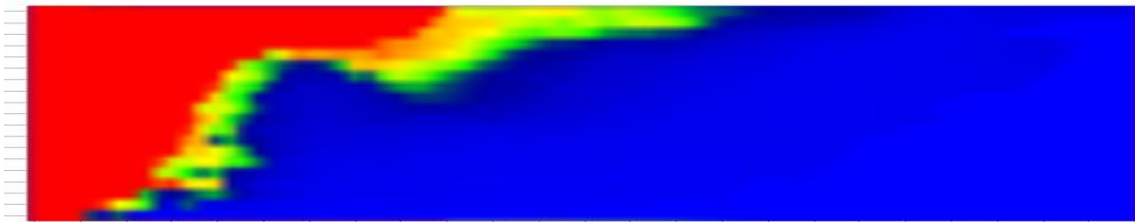
$K_v /K_h =0.05$ $(N_g =0.186)$
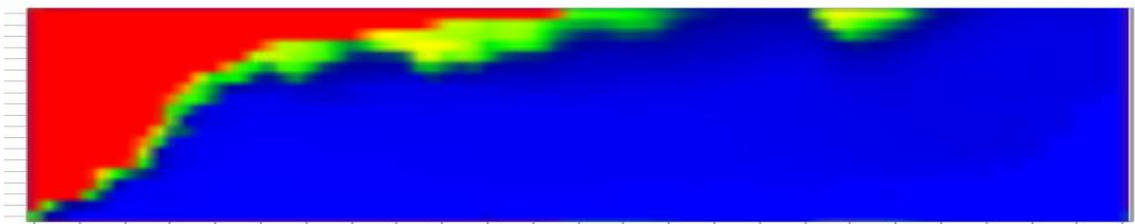
$K_v /K_h =0.2$ $(N_g =0.74)$
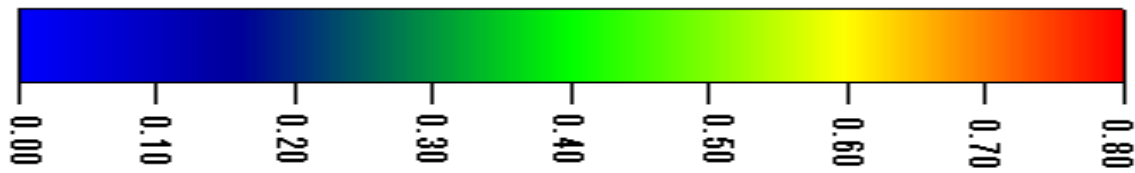
Fig. 48 - Gas saturation profile @ 0.37 PVI for 2-D homogeneous (X-Z) gas injection:
effect of K_v/K_h
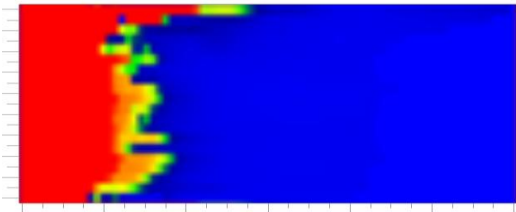
Well Distance (L) = 400   (N_g = 0.046)
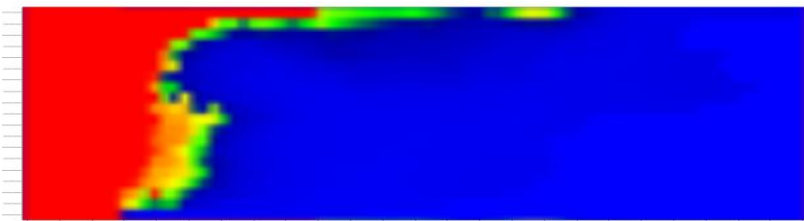
Well Distance (L) = 600 ft   (N_g = 0.1049)
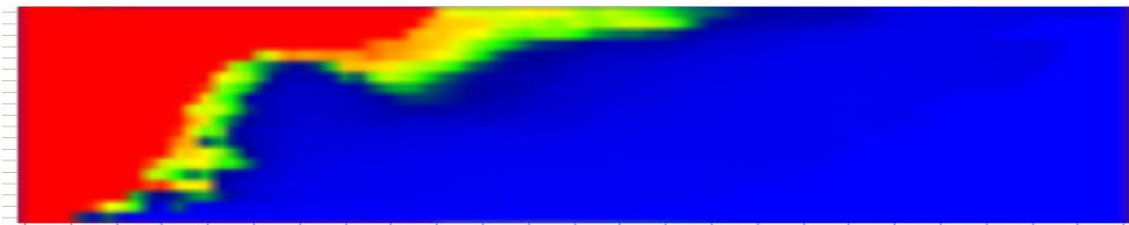
Well Distance (L) = 800 ft   (N_g = 0.1866)
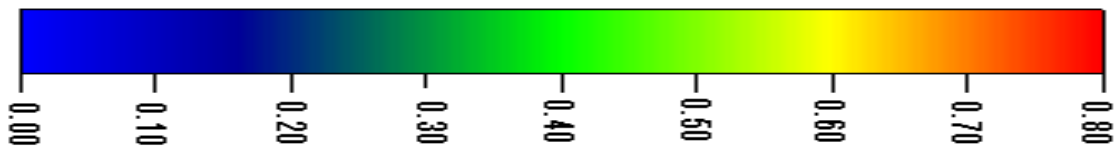
Fig. 49 - Gas saturation profile @ 0.37 PVI for 2-D homogeneous (X-Z) gas injection:
effect of well-to-well distance

Effect of well-to-well distance (L)

Gravity number is also varied by changing the well distance, keeping other parameters constant. Simulation model constructed in these runs is the same as the one described in Table 12. Fig. 49 shows the gas saturation maps at 0.37 PVI for well distance of 400ft, 600ft, and 800ft. The corresponding gravity numbers are 0.046, 0.1049, and 0.1866 respectively. The saturation map for well distance of 400 ft is a piston like displacement as compared to the third gas saturation map for well distance of 800 ft where gravity override is very significant. As the well distance (*L*) is increased, there is sufficient time for the solvent to rise up and segregate before it is taken out from the production well. Low density gas rises up leaving significant amount of oil unswept in the lower portion of reservoir.
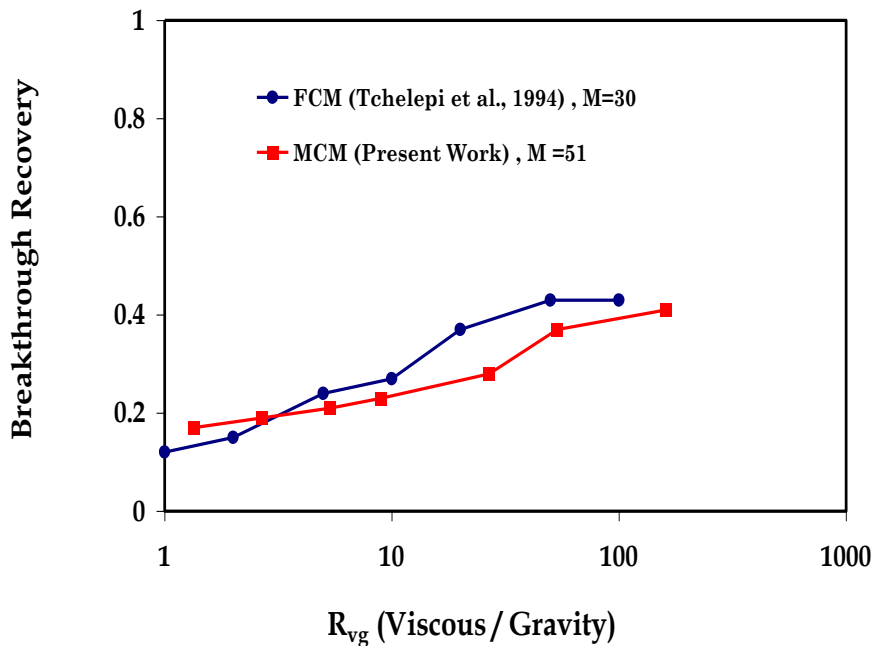
Fig. 50 - Effect of viscous-to-gravity ratio (R_{vg}) on breakthrough recovery
for 2-D MCM and FCM displacements

Effect of R_{vg} (viscous-to-gravity ratio) on breakthrough recovery

From the examples discussed in the last few sections, there is little gravity segregation for gravity numbers below 0.02. Above N_g of 0.5, the gravity tongue is well developed. Viscous-to-gravity ratio, R_{vg} is often used in the literature to correlate with vertical sweep efficiency of first contact miscible floods.[5,31] We plot our multicontact miscible injection data in terms of R_{vg} (inverse of N_g) to show the correspondence with the literature data. R_{vg} varies from 1.33 to 161; mobility ratio is 51 for our data. Breakthrough recovery is plotted against R_{vg} in Fig. 50. It can be observed that breakthrough recovery increases with an increase in R_{vg}. Gravity forces are more dominant at lower values of R_{vg}, resulting in the formation of gravity tongue and early breakthrough as observed in the previous examples. Simulation results for our multi-contact miscible case (M=51, *L/H*=16) are compared with the breakthrough recovery curve generated by Tchelepi and Orr (1994) for a 2-D homogeneous first contact miscible case (M=30, *L/H*=4). Our simulations were run at constant pressure drop; the literature data was from constant injection rate simulations. The breakthrough recoveries cannot be compared quantitatively because of the differences in parameter values, but it can be concluded that both the simulations show the transition regime at R_{vg} between 1 and 100.

Simulation Parameter	Value
No. of Grid Blocks (X-Z)	100 * 20
Grid Size	4 * 2.5 (ft)
Injector Well (BHP)	1800 (psi)
Producer Well (BHP)	1100 (psi)
Initial Pressure	1500 (psi)
Reservoir Temp.	140 (^{0}F)
Oil Viscosity	1 (cp)
Initial Oil Saturation	0.8
Initial Water Saturation	0.2
No. of Streamlines	300

Table 13 - Simulation parameters for 2-D (X-Z) gas injection with heterogeneous permeability field.

Heterogeneous permeability field

This model has a 2-D vertical cross-sectional geometry with 100 grid blocks in x-direction and 20 grid blocks in z-direction. The reservoir is 400 ft long and 50 ft thick. Geostatistically generated heterogeneous permeability field (Perm2) is used. Vertical injection and production wells are located on left and right side of the model and completed in all 20 layers. Both the wells are set at constant bottom hole pressures and are 400 ft apart. The parameters of this model are listed in Table 13. A mixture of (52 %) methane and (48 %) propane is injected into the reservoir Oil 2 (as described in Table 1).

300 streamlines are launched from the injection well. Fig. 51 shows the gas saturation at different pore volume injected. The distribution of gas is governed by the combination of

gravity forces and heterogeneity effects. At early times, injected gas follows the path of high permeability layers and also rises up in the reservoir due to density contrast. At later times, gas present in the top layers start moving down towards the high permeability region. N_g is 0.018 because effective K_v/K_h is 0.02. Heterogeneity slows down gravity override.

PVI =0.30

PVI =0.48
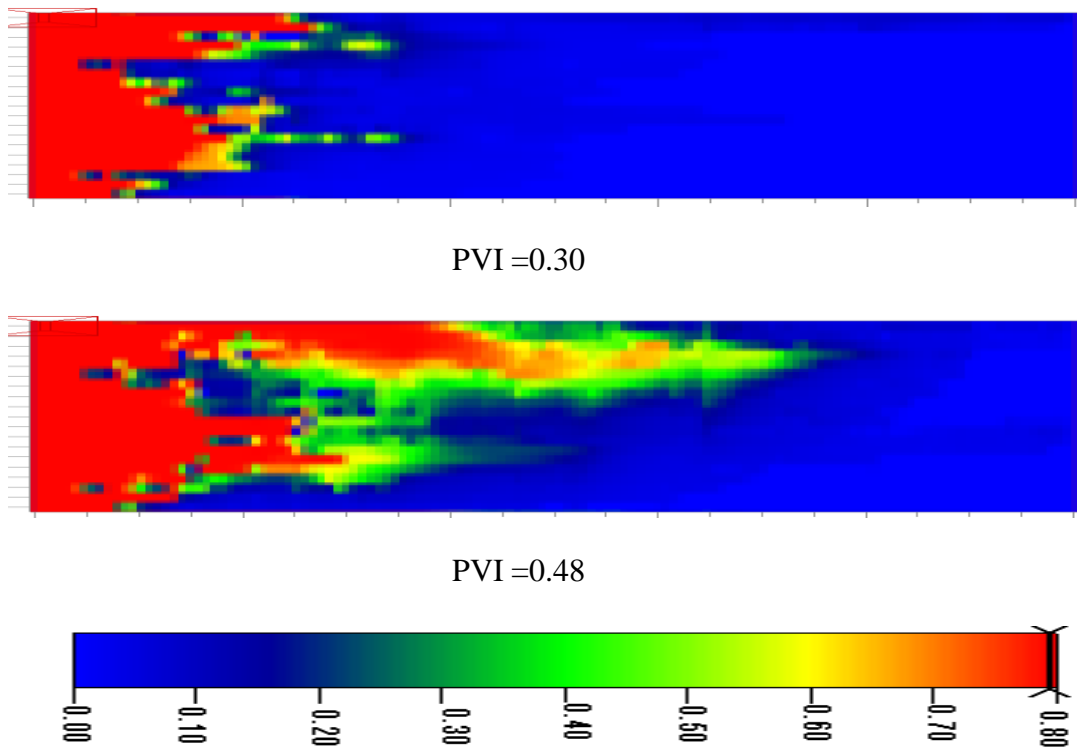
Fig. 51 - Gas saturation distribution for 2-D (X-Z) gas injection simulation with heterogeneous permeability field Perm2 (N_g = 0.018)

Layer 1 (From Top)

Layer 4 (From Top)

Layer 5 (From Top)
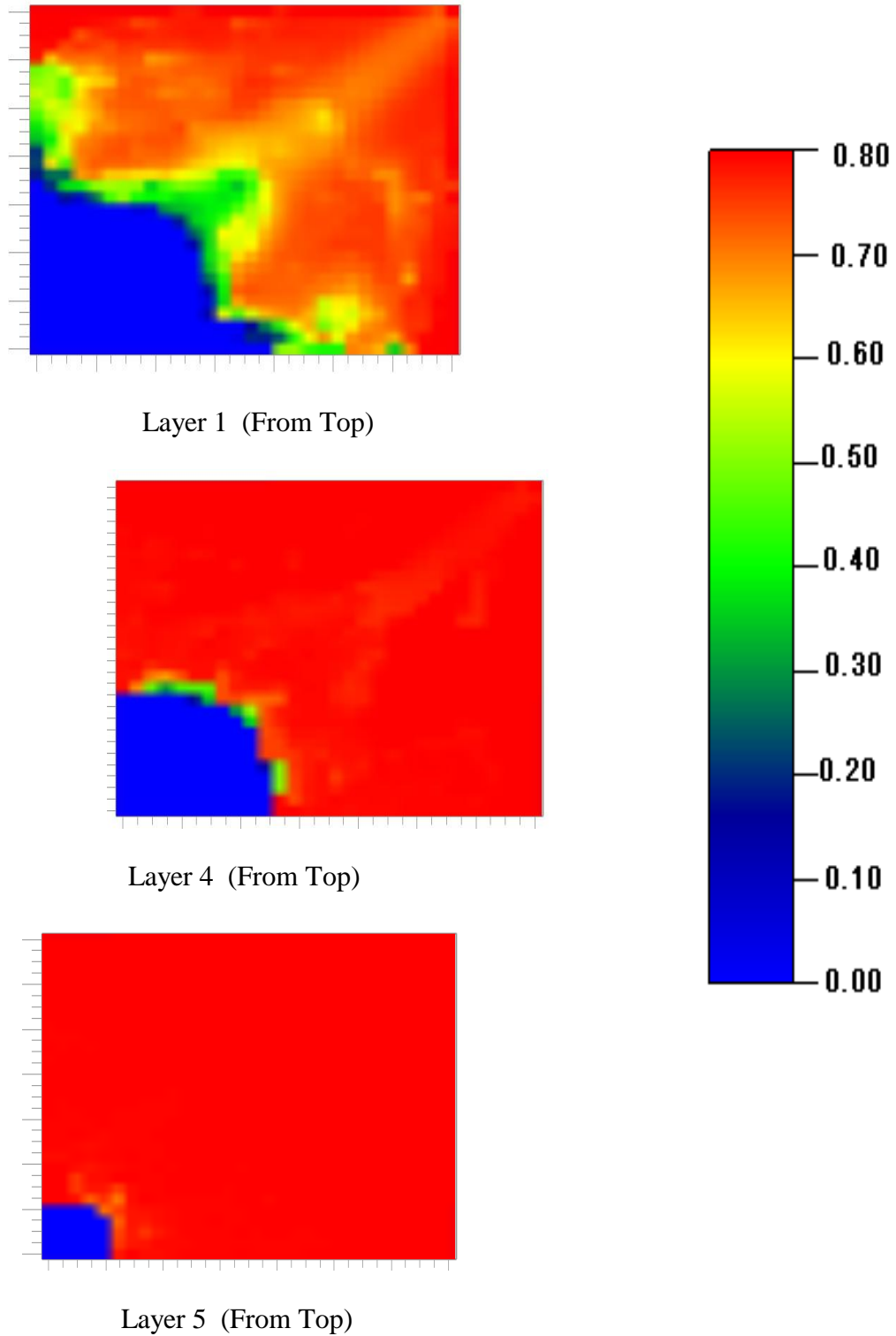
Fig. 52 - Oil saturation profiles @ 0.45 PVI for 3-D gas injection (N_g =0.46)

3-D Gas injection in a homogeneous quarter five spot

Gas injection into a 3-D reservoir block is simulated. The same oil (oil 1) and miscible injectant (solvent I) as the last example have been used. 4500 grid blocks are used to represent a 3-dimensional reservoir block with 30 grids in x-direction, 30 grids in y-direction, and 5 grids in z-direction. Reservoir size is 750 ft * 750 ft * 50 ft. Homogeneous permeability field is used with vertical to horizontal permeability ratio of 0.07. Injector and producer wells are vertical and completed in all 5 layers. Injector and producer well are set at constant bottom hole pressures of 1800 psi and 1100 psi respectively. Initial reservoir pressure is 1500 psi. The corresponding gravity number is 0.46. Table 14 lists the parameters used in these simulations.

Oil saturation profile for several layers (X-Y plane) is plotted at 0.45 PVI as shown in Fig. 52. Gas being lighter moves up, displacing very little oil in the bottom most layer (layer 5). Layer 4 which is above layer 5 has a slightly better sweep pattern than layer 5. Oil saturation distribution for layer 2 at the same time instant shows that due to gravity override, injected solvent is close to the producer in the top layers and is about to break through. Dispersion is observed in the saturation distribution partly due to the time step selection and operator splitting approximation in convective and gravity steps.

Simulation Parameter	Value
No. of Grid Blocks (X-Z)	30 * 30 * 5
Grid Size	25 * 25 * 10 (ft)
Horizontal Permeability (K_h)	425 (md)
Vertical Permeability (K_z)	30 (md)
Injector Well (BHP)	1800 (psi)
Producer Well (BHP)	1100 (psi)
Initial Pressure	1500 (psi)
Oil Viscosity	1 (cp)
Initial Oil Saturation	0.8
Initial Water Saturation	0.2

Table 14 - Simulation parameters for 3-D gas injection

Three hydrocarbon phase system

1- D Gas Injection

One-dimensional slim-tube simulations are performed with 100 grid blocks to investigate the miscibility behavior of oil 2 with different solvents and determine the minimum miscibility enrichment of carbon dioxide with NGL. Recovery at 1.2 PV for different mixtures of NGL and carbon dioxide is shown in Fig. 53. It can be observed that pure CO_2 is immiscible with oil 2. Recovery goes up as carbon dioxide is enriched with NGL. Recovery is around 0.99 at 20 % NGL which is the MME of CO_2 with NGL. Two different solvents 100 % CO_2 (solvent III) and 75 % CO_2 with 25 % NGL (solvent IV) are selected for 2-D field-scale simulations. Oil saturation during 1-D simulations of oil displacement by gas is plotted in **Fig. 54** for both the solvents. It clearly indicates that

solvent III (100 % CO_2) is immiscible and solvent IV (75% CO_2 -25% NGL) is multi-contact miscible with the reservoir oil 2.
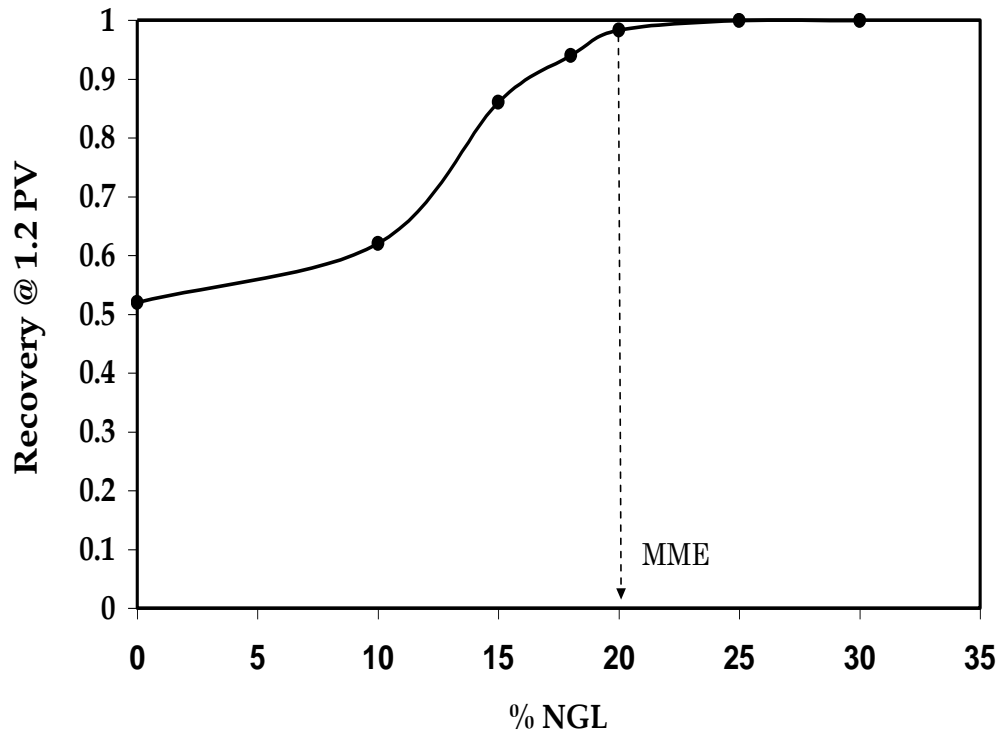
Fig. 53 - Minimum miscibility enrichment (MME) of CO_2 with NGL (Oil 2)
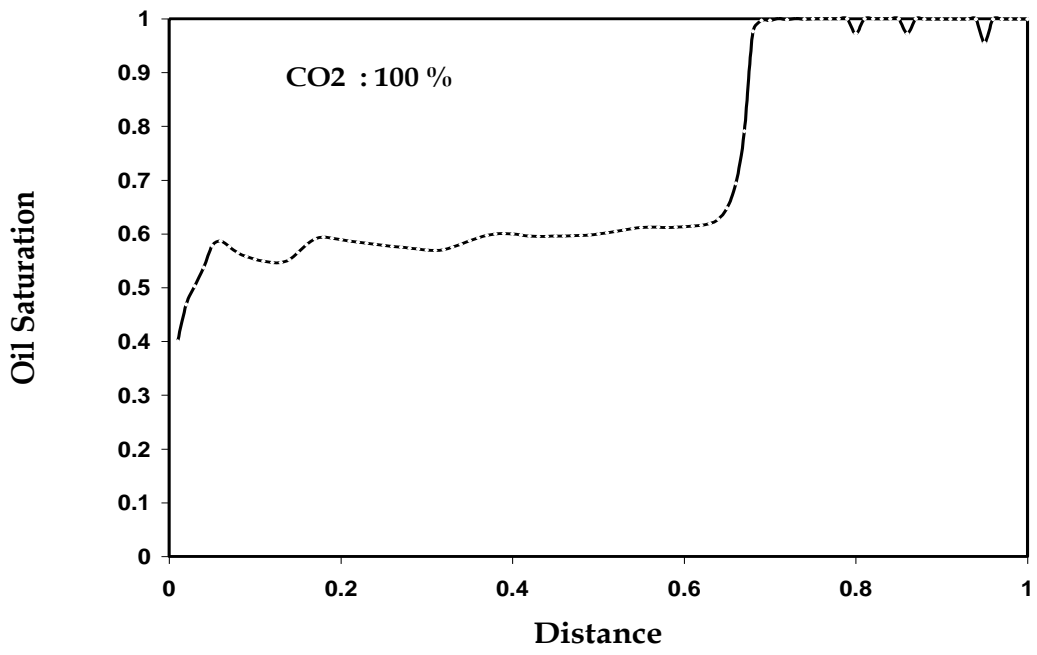
Fig. 54a - Oil saturation distribution in 1-D immiscible gas injection (with Oil 2)
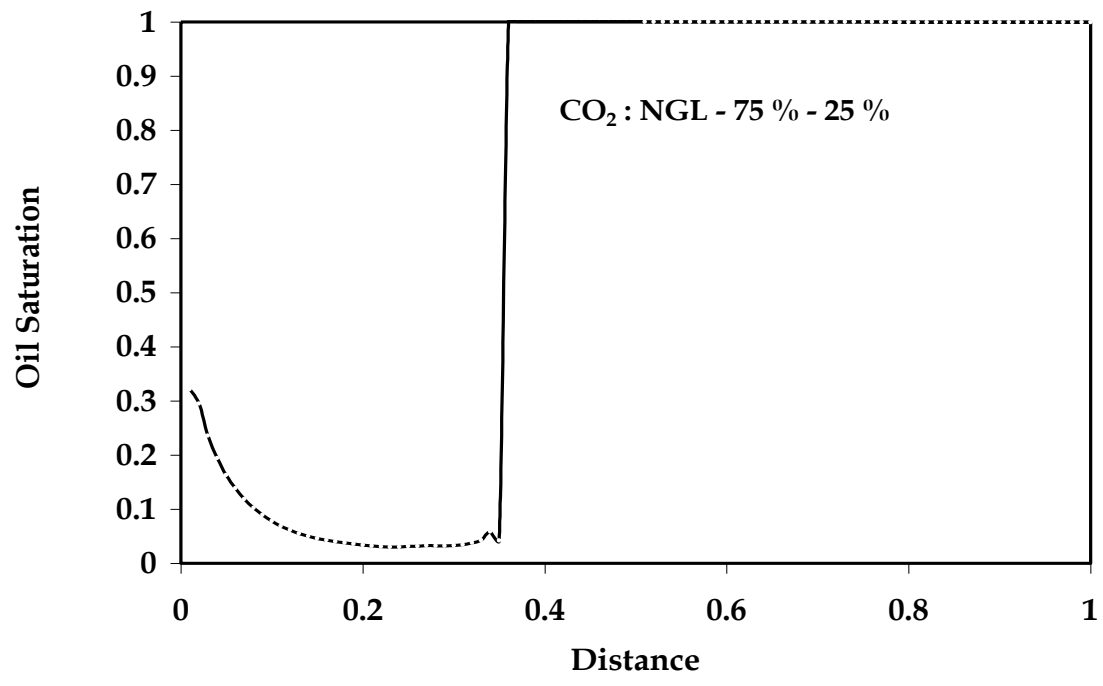
Fig. 54b - Oil saturation distribution in 1-D miscible gas injection (with Oil 2)

2-D Gas Injection (X-Y Cross-section)

Homogeneous Permeability Field

2-D simulation is conducted for gas injection into a quarter five spot pattern. The simulation model consists of case is 20 * 20 * 1 cartesian grid blocks with one injector well and one producer well. The boundaries of the square region are no flow boundaries. Simulation details and oil composition (Oil 2) used in this study are listed are in Table 15 and Table 8, respectively. Solvent III (pure CO_2) is injected into the reservoir as an immiscible injectant. Reservoir temperature is set at 82 ^{0}F. A homogeneous permeability field with 300 md permeability is used in this case. Initial reservoir pressure is 1500 psi. Injector and producer wells are kept at constant bottom hole pressures of 1800 psi and 1100 psi, respectively. Initial oil saturation at the reservoir pressure and temperature is 0.75.

Figs. 55-57 provide the oil, gas, and second liquid phase distribution, respectively, at 0.13 PV of solvent injected. Saturation contours obtained from streamline simulator are compared to the saturation maps derived from finite difference simulator. Results seem to be in very good agreement except for small differences. Oil phase is continuously displaced by gas; oil saturation profile decreases monotonically along the diagonal joining the injector and the producer. The second liquid phase is present in a lot of grid blocks swept by gas with saturation values as high as 0.51. Gas phase exists in only a few grid blocks, with very low saturation values. Most of the grid blocks with non-zero gas phase saturation are near the displacement front. Fig. 58 shows the oil viscosities of oil, gas, and second liquid phase at 0.13 PVI. Due to the dissolution of injected carbon dioxide, oil viscosity decreased from 1 cp to 0.29 cp in some grid blocks.

Simulation Parameter	Value
No. of Grid Blocks (X-Y)	20 * 20
Grid Size	20 * 20 (ft)
Horizontal Permeability (K_x)	300 (md)
Injector Well (BHP)	1800 (psi)
Producer Well (BHP)	1100 (psi)
Initial Pressure	1500 (psi)
Reservoir Temp.	82 (^{0}F)
Oil Viscosity	1.0 (cp)
Initial Oil Saturation	0.75
Initial Water Saturation	0.25
No. of Streamlines	200

Table 15.   Simulation parameters for 2-D, three HC phase gas injection (X-Y)

(Homogeneous Case)
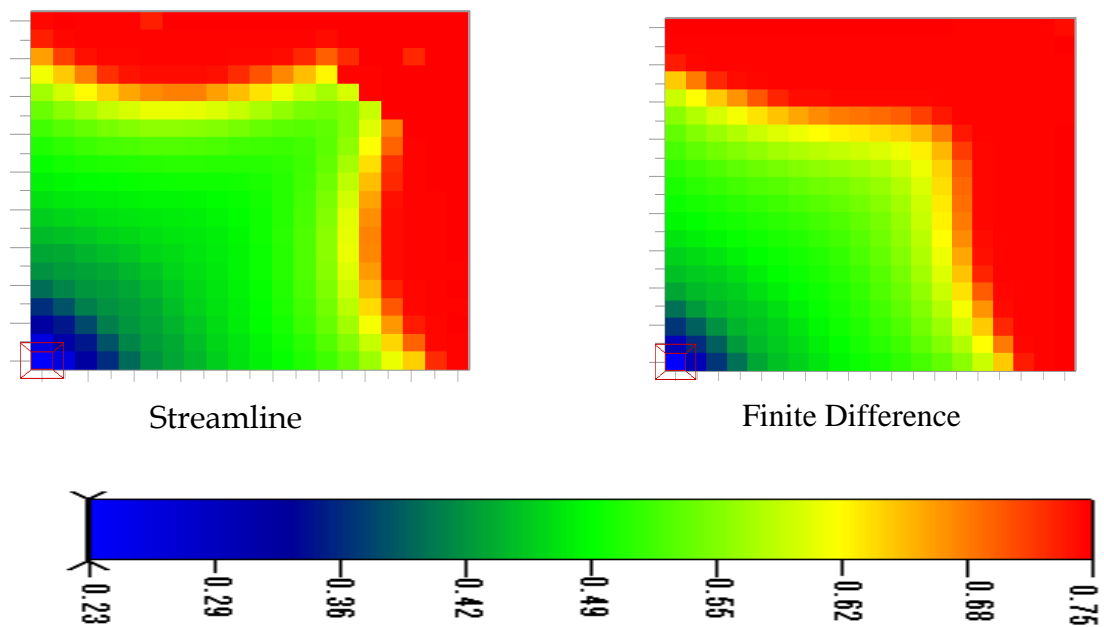
Streamline   Finite Difference

0.23   0.29   0.36   0.42   0.49   0.55   0.62   0.68   0.75

Fig. 55 - Oil saturation profiles @ 0.13 PVI for 2-D (X-Y) immiscible gas injection

(3 HC phase system)

Streamline   Finite Difference

Fig. 56 - Gas saturation profiles @ 0.13 PVI for 2-D (X-Y) immiscible gas injection

(3 HC phase system)

Streamline   Finite Difference
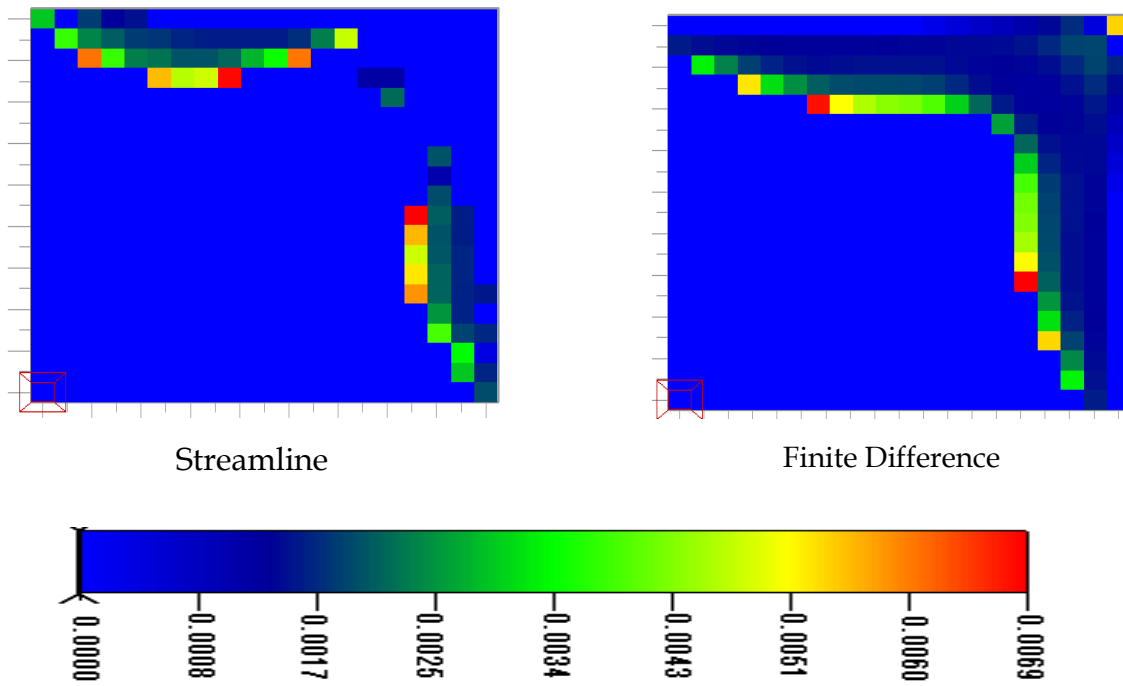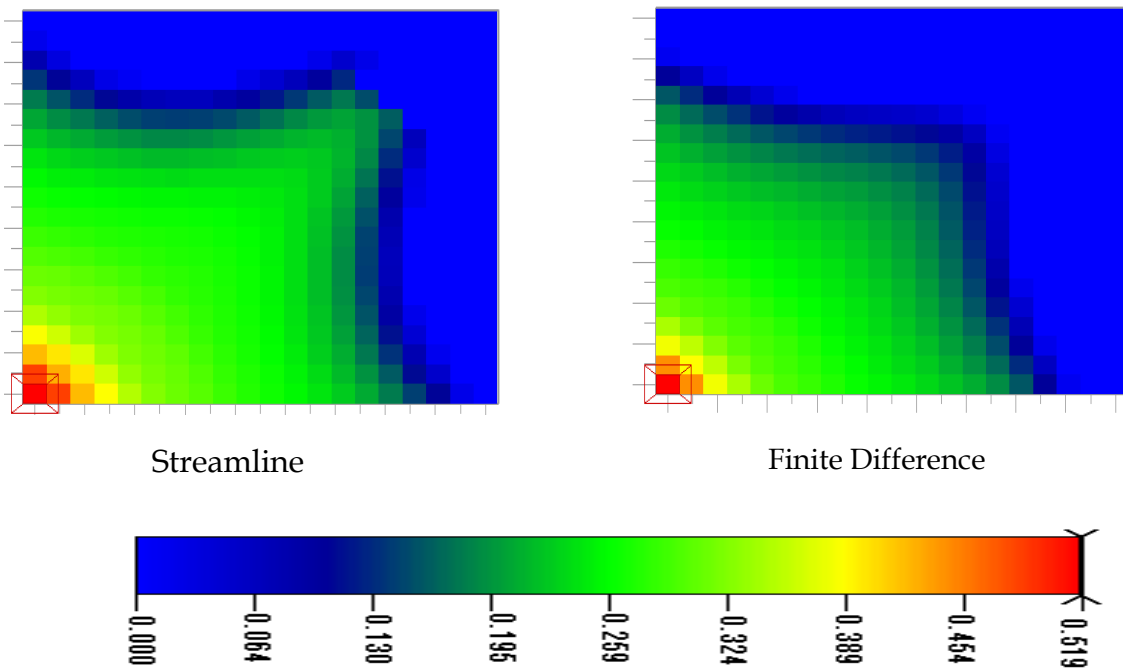
Fig. 57 - Second liquid phase saturation profiles @ 0.13 PVI for 2-D (X-Y) immiscible

gas injection (3 HC phase system)
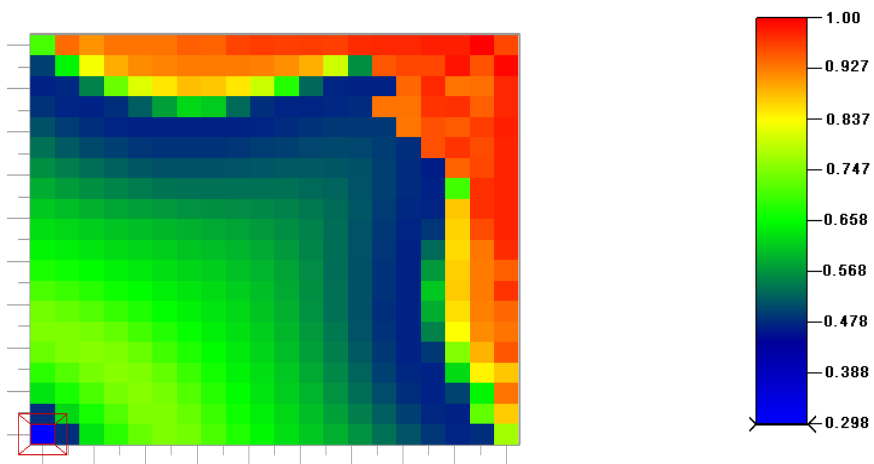
Oil Viscosity
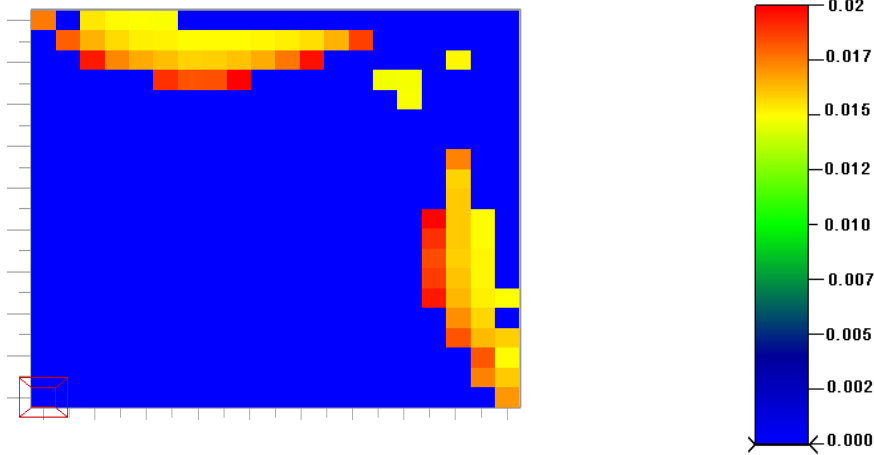
Gas Viscosity
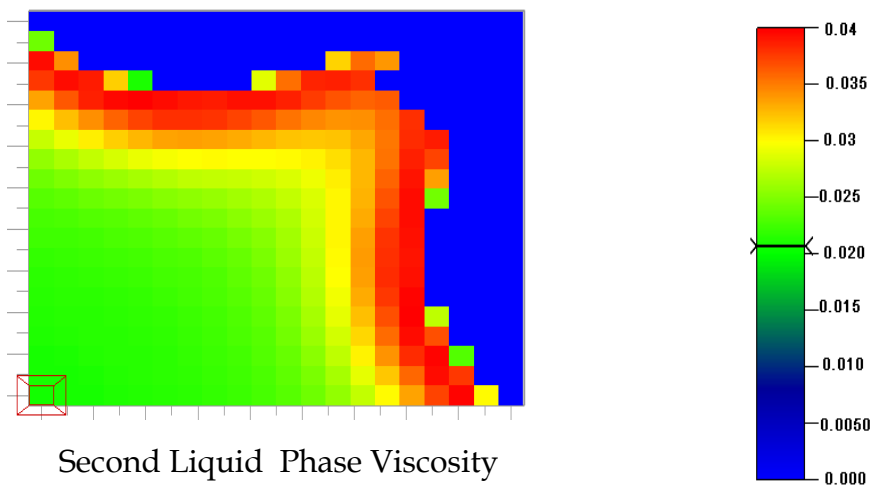
Second Liquid Phase Viscosity

Fig. 58 - Phase viscosities at 0.13 PV injected in 2-D gas injection (3 HC phase system)

106

Heterogeneous Permeability Field

A heterogeneous permeability field (Perm 1), is used in this case. The oil composition is the same as the one described in previous example (Oil 2). Solvent IV, which is a mixture of 75 % CO_2 and 25 % NGL is injected into the reservoir oil as a miscible injectant. 40 *40 *1 grid is used to represent the reservoir geometry in X-Y plane. Reservoir is 400 ft long and 400 ft wide with one vertical injection well and production well located at the corner. Both the wells are set at constant bottom hole pressures of 1800 psi and 1100 psi respectively. Simulation parameters used in this simulation are listed in Table 16.

Fig. 59 shows the pressure distribution at 0.27 PVI. Pressure contours are asymmetric due to the heterogeneous permeability field. Oil and second liquid phase saturation contours are shown in Figs. 60 and 61, respectively. The solvent follows the path of high permeability region; low permeability areas remain unswept. Second liquid phase is present in most of the grid blocks swept by the gas with the saturation as high as 0.67.

Simulation Parameter	Value
No. of Grid Blocks (X-Y)	40 * 40
Grid Size	10 * 10 (ft)
Injector Well (BHP)	1800 (psi)
Producer Well (BHP)	1100 (psi)
Initial Pressure	1500 (psi)
Reservoir Temp.	82 (^{0}F)
Oil Viscosity	1.0 (cp)
Initial Oil Saturation	0.75
Initial Water Saturation	0.25
No. of Streamlines	200

Table 16 - Simulation parameters for 2-D, three HC phase gas injection (X-Y)

(Heterogeneous Case)
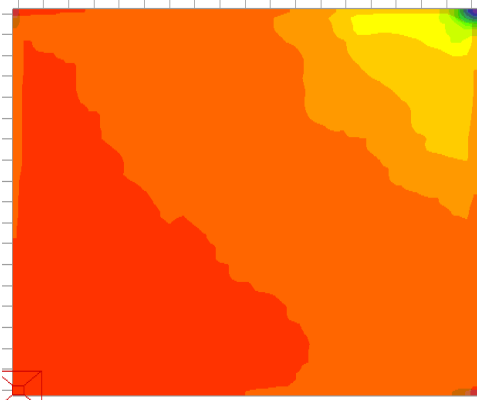
Fig. 59 - Pressure profile @ 0.27 PVI for 2-D (X-Y) heterogeneous reservoir

simulation (3 HC phase system)
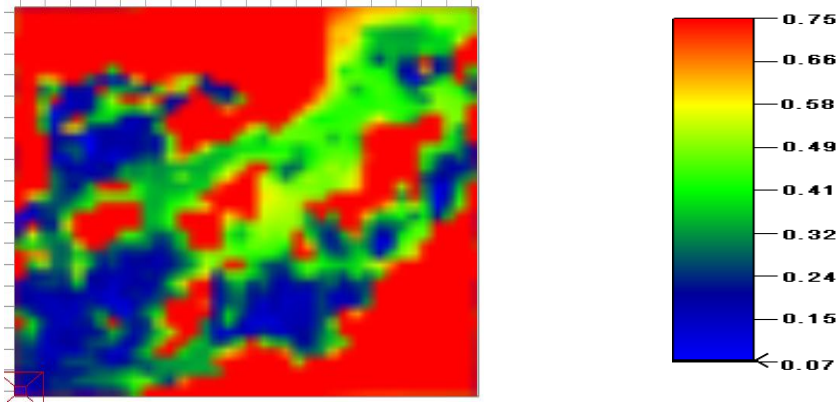
Fig. 60 - Oil saturation @ 0.27 PVI for 2-D (X-Y), heterogeneous reservoir simulation (3 HC phase system)
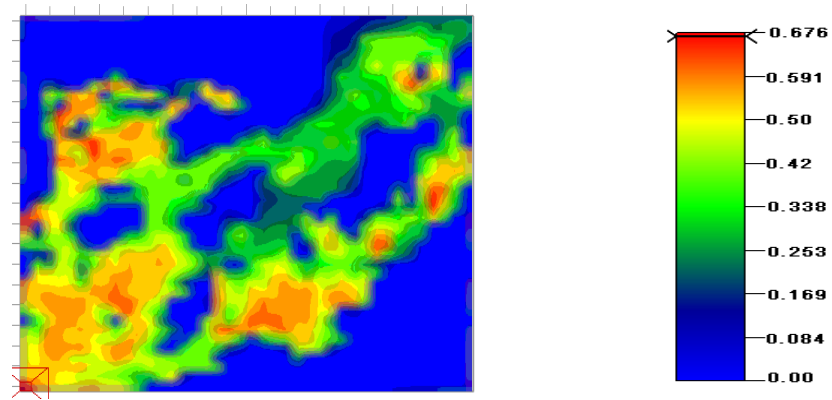
Fig. 61 - Second liquid. phase saturation @ 0.27 PVI for 2-D (X-Y) heterogeneous reservoir simulation (3 HC phase system).

Parallelization

Example 1: 2-D Gas Injection (Efficiency of Parallelization)

A test case is run in sequential and parallel mode to investigate the CPU time distribution of streamline computations. The simulation model used in this case consists of 40 * 40 * 1 cartesian grid blocks with one injector well and one producer well, as described in Table 11; results have been discussed in Fig. 38. The computational time is discussed below.

CPU Time Distribution: Sequential Run

CPU time distribution of this test case is shown in **Fig. 62**, in the form of pie charts. Total simulation time is around 15,264 s. It can be seen (Fig. 62a) that streamline computations (14379 s) consume a large part of the total execution time as compared to finite difference calculations (648 s). Fig. 62b shows further breakdown of streamline CPU time. It is clearly evident that flux calculation accounts for more than 95 % of the CPU time taken by streamline calculations (14,379 s). Other streamline operations (streamline launching, streamline tracing, mappings, etc) consume very small amount of CPU time (237 s) as compared to one-dimensional solver where fluxes are evaluated at all streamline points. For better understanding, CPU time for each part of flux calculation procedure is recorded as shown in Fig. 62c. It is observed that flash calculation (10,584 s) is the most time consuming step in flux estimation. Flash procedure consumes 75 % of the total CPU time for flux evaluation. Other steps involved in the flux estimation (3,795 s) are updating phase saturations, densities, viscosities, relative permeabilities, and fractional flow. All these account for 25 % of the flux CPU time.

FD
(648 sec)

Streamline
(14616 sec)

Flux Calculations :   14379 secs

Other Computations: 237 secs
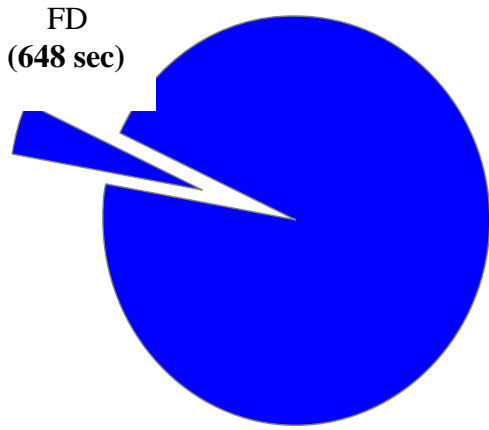
Total Simulation Time : **15264 sec**

Fig. 62b.   Execution time breakdown of
streamline computations.

Fig. 62a. CPU time breakdown of
gas injection case.

3795 secs

Flash Calculations
10584 sec
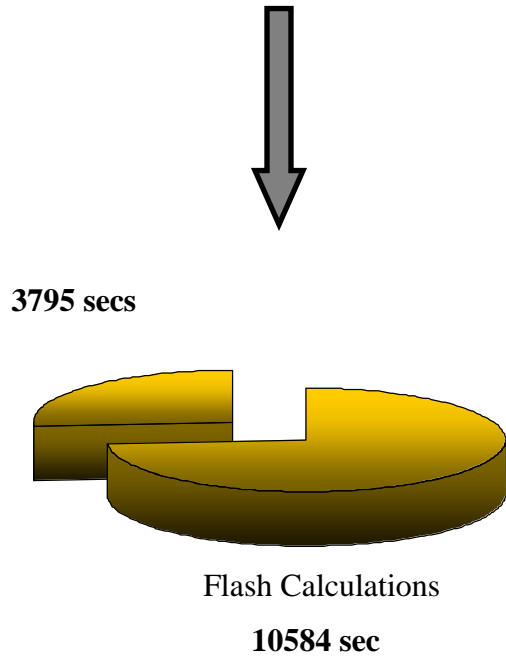
Fig. 62c. CPU time breakdown of
flux calculations.

Fig. 62 - CPU time distribution of 2-D gas injection case

While updating the component fluxes, flash calculations are conducted at streamline points in the region behind the front where more than one hydrocarbon phases exist. All the streamline points lying in the interior of the single-phase region are skipped, i.e., no phase equilibrium calculations are performed at these points. Fig. 63 shows the plot of CPU time taken by flash calculation per global time step. It indicates that the time spent in flash calculations at the streamline points increases with the simulation time. This is mainly because as the front propagates, more streamline points are enclosed in the two or three hydrocarbon phase region where flash procedure needs to be performed. In compositional streamline simulation, longest computational tasks are flash procedures and flux estimation at streamline points while updating compositions along the streamlines. Therefore it is important to launch an optimum number of streamlines while representing the flow in the reservoir.
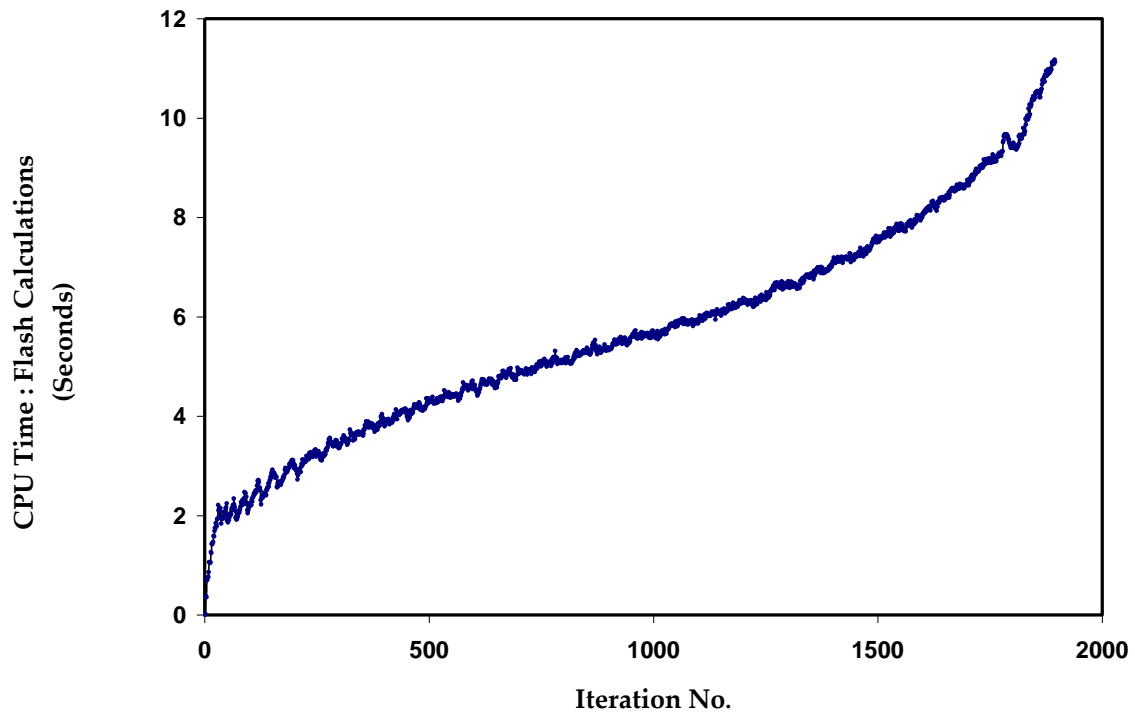
Fig. 63 - CPU time spent in flash calculations per global time step

CPU Time Distribution: Parallel Run

All the simulation cases presented in this work are carried out on a HP Itanium2 based Atlantis cluster at the Texas Learning and Computation Center (TLC2), University of Houston. The cluster runs RedHat Enterprise Linux 3 for the ia64 architecture. The cluster has 152 nodes with 4 GB memory and 1.4GHz processors. A Myrinet switch is used to interconnect the nodes. Four different examples are simulated on this cluster to examine the efficiency of parallelization of this streamline simulator.

Example 1 is simulated in both serial and parallel mode using different number of processors. 200 streamlines are launched to represent the flow. Identical results are obtained for serial and parallel simulations. For parallel mode, simulation is conducted on two, four, five, eight, ten, twenty, and twenty-five processors. Execution times for

different number of processors are plotted in Fig. 64. It is clearly evident that the CPU time is significantly reduced as we increase the number of processors. This is because of the fact that the largest computational task (flux evaluations along streamlines) is performed by multiple processors. It took around 4.24 hrs to run the test case on a single processor. The same problem can be run in approximately 0.5 hrs on 20 processors. To measure the efficiency of parallel processing, speed up is studied as a function of number of processors. Speed up is defined as the ratio of CPU time of the serial execution (T_s) to the CPU time of parallel execution (T_n).

Ideal speed up should be equal to the number of processors (n) used in the parallel run. In this example, ideal speed up is never achieved and is lower than n as we increase the number of processors. Fig. 64 illustrates the speed up for different number of processors. Although a good speed up is obtained for the test case described above, minimal CPU time reduction is observed beyond 20 processors. Speed up does not follow a linear trend as the number of processors is increased. The inefficiency in speed up is discussed below.
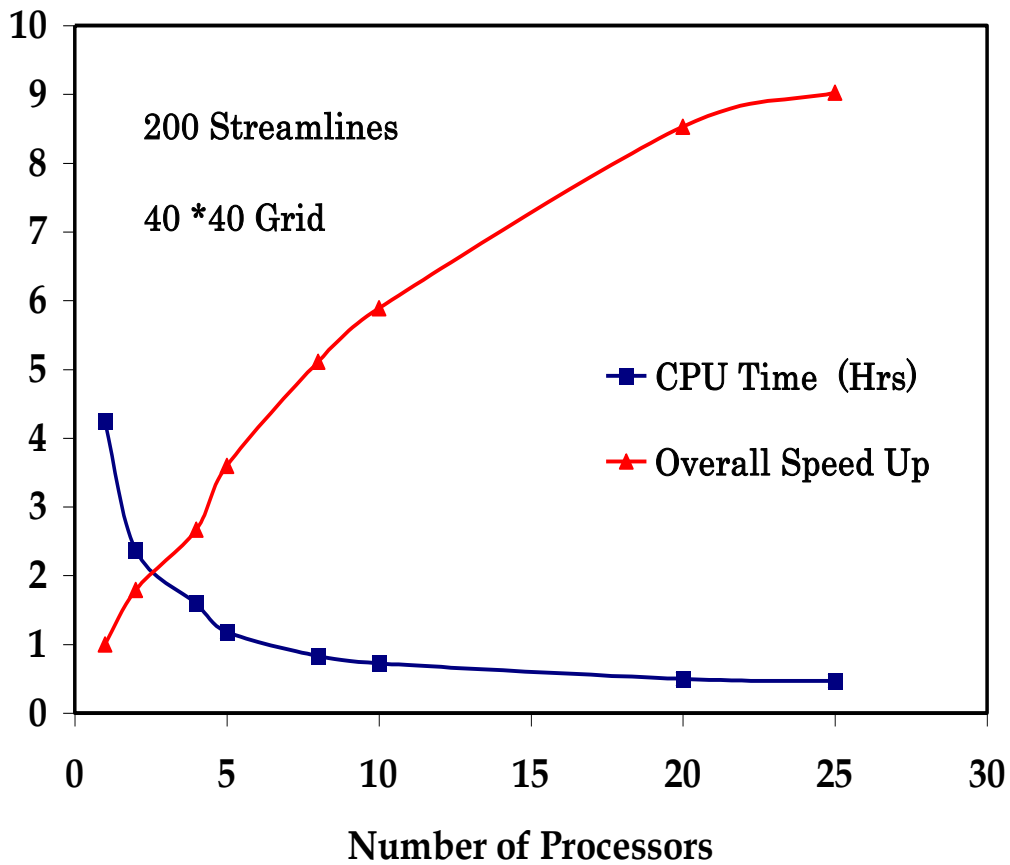
Fig. 64 - CPU time and overall speed up vs. number of processors for 200 streamlines

The total execution time is the sum of the CPU time in performing the finite difference operations, streamline operations, and the inter processor communication time spent in gathering all the updated information along the streamlines. After gathering all the streamline data (in the form of one dimensional arrays) on a single processor, the updated compositions are rearranged to original three-dimensional arrays. Therefore, this gathering time includes the inter processor communication time and the time spent in copying and rearranging the arrays. As an illustration, the break up of total CPU times for multiple processors is shown in Figs. 65 and 66. The finite difference computation time is about ~ 650 s (Fig. 65) which remains constant with increase in number of processors.

This is because finite difference part of the simulator is not parallelized and all the finite difference calculations are performed on a single processor. The inter processor communication time is about 250 ± 40 s (Fig. 65) and does not increase with number of processors. Fig. 66 indicates that computational load in performing all the streamline computations decreases in proportion to the number of processors; the parallelization is quite efficient. When the number of processors gets to about 20, the streamline computation time gets down to 864 s, less than the time for finite difference calculation and communication ($\sim$ 650 s + 250 s). Thus, the overall speed up does not increase linearly. To obtain higher speed up, the finite difference calculation would need to be parallelized.
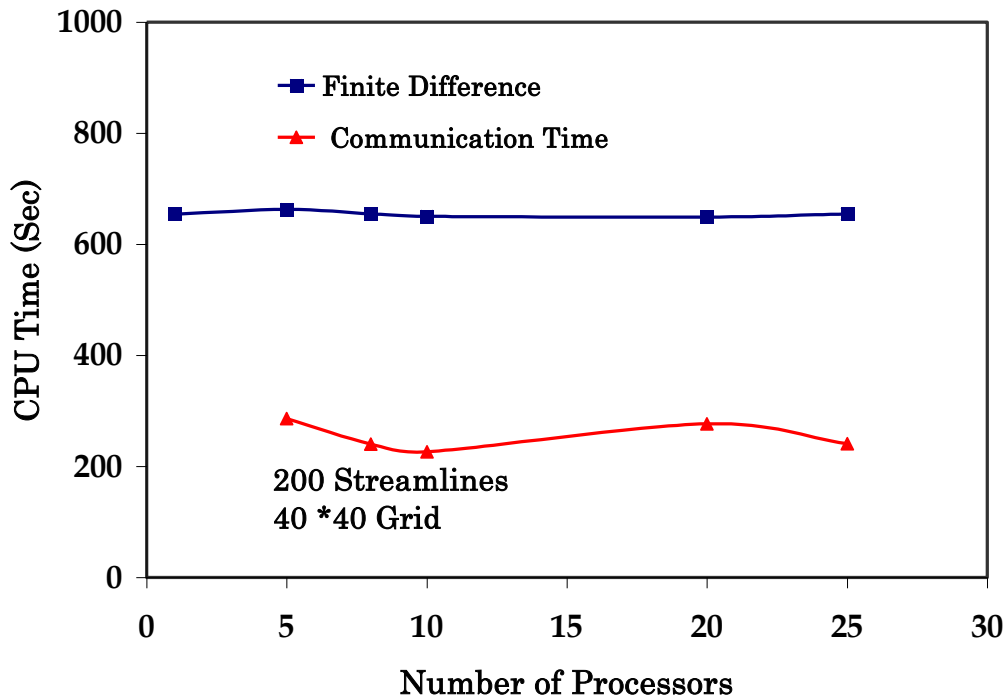
Fig. 65 - Finite difference and communication time vs. number of processors
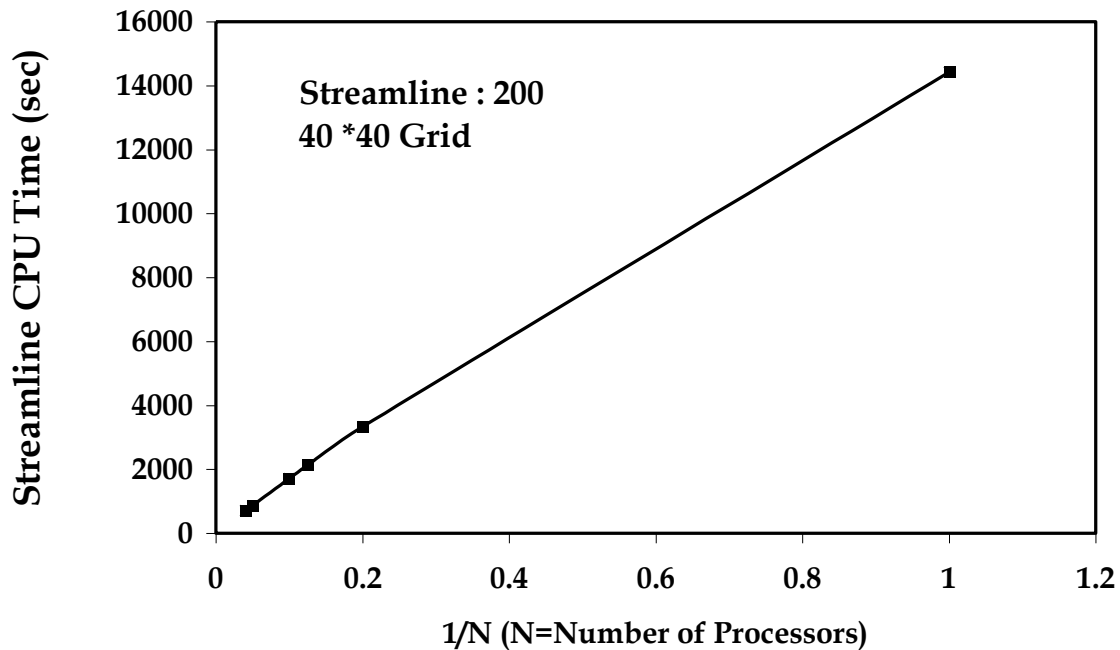
Fig. 66 - Streamline CPU time vs. (1 / Number of Processors)

Load Balancing

Load balancing refers to the distribution of task among different processors to minimize waiting time for processors. If some processors have more work assigned as compared to other processors, then the simulation time will be determined by the time taken by the busiest processor. This will increase the waiting/idle time of other processors and decrease the efficiency of simulation. Performance can be increased if work can be evenly distributed. If there are many tasks of varying sizes, it may be more efficient to maintain a task pool and distribute to processors as each finishes.

In the example described above, 200 streamlines are evenly distributed on n (1-25) processors. Although each processor operates on equal number of streamlines, CPU load on each processor may differ due to different number of multiphase points along

117

streamlines. More CPU time is spent in processing the streamlines with large number of multiphase grid points primarily due to flash calculations. To demonstrate the load balancing associated with our simulations, CPU load for streamline calculations is recorded for each processor in a 20 processor run, as shown in Fig. 67. It can be observed that CPU load distribution is non-uniform with some processors doing more work compared to others. Processor 1 and processor 11 handled streamlines near the edge of the five spot model and had least computational task to perform as compared to processor 10 and 20 which consumed the maximum CPU time in performing streamline operations along the diagonal of the five spot model. This non-uniform CPU load distribution clearly suggests that processors 1-5 and 11-15 had to sit idle, waiting for other processors to finish their task before all the streamlines are gathered on a single processor.
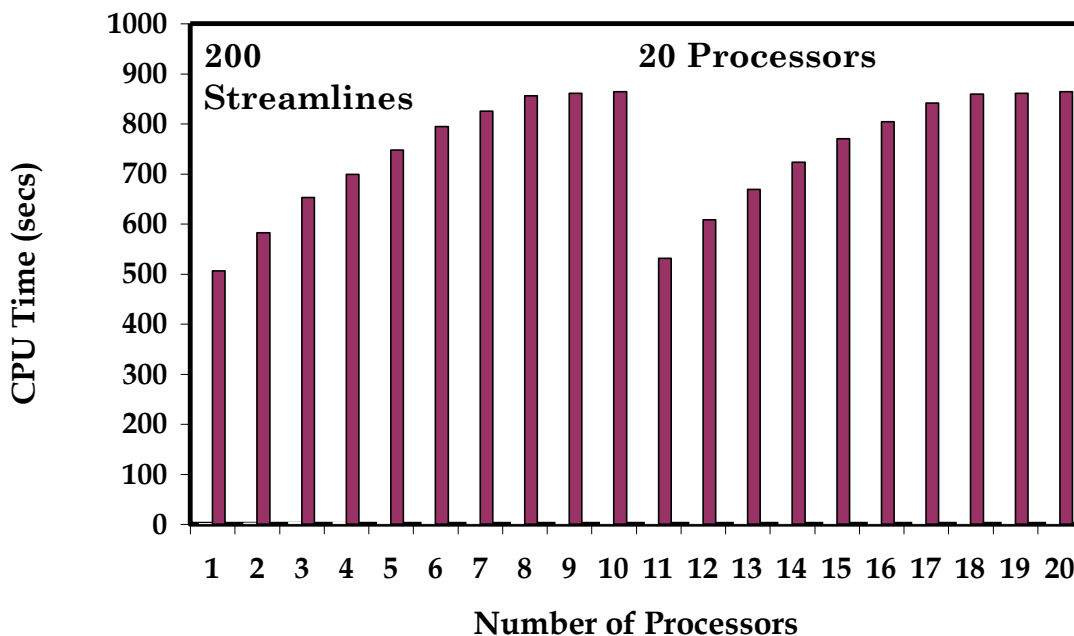
Fig. 67 - CPU load distribution for a 20 processor run on 40 *40 grid and 200 streamlines

118
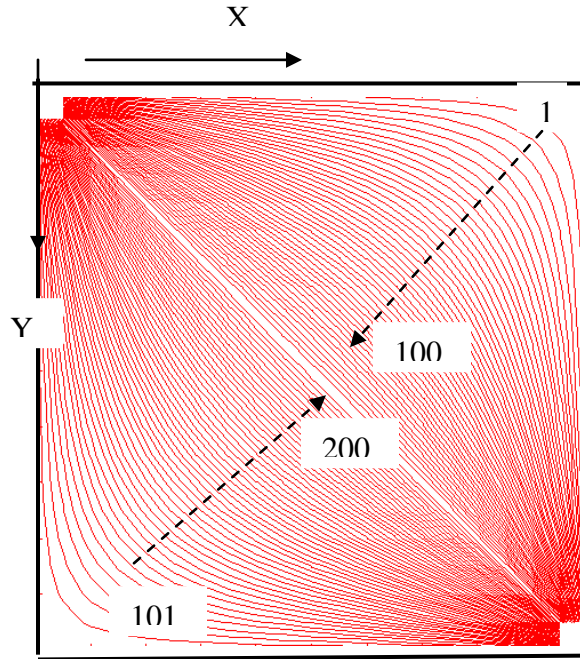
Fig. 68 - Streamlines in 2-D homogeneous gas injection (200 streamlines)

Another interesting observation is that the CPU load distribution is symmetric with respect to processors 1-10 and processors 11-20. This can be explained due to the homogeneity and symmetry of the model which generated a symmetric pattern of streamlines as shown in Fig. 68. Streamline 1-100 are launched from the X face and 101-200 are launched from the Y face. Each processor operates on a set of (200/20) 10 streamlines assigned to it. Streamlines 1-10 which are close to the edges of the domain are assigned to processor 1 where as streamlines 90-100 which are close to the diagonal are processed by processor 10. Similar pattern is obtained for streamlines 101-110 which belong to processor 11 and streamlines 190-200 on processor 20. As mentioned previously, flash calculations are performed at streamline points with multiphase fluids. According to the geometry of pattern, more points are enclosed in the two/three hydrocarbon phase region along the streamlines, which are close to the diagonal as

compared to the streamlines which are away from the diagonal. Therefore the processors (10 and 20), which operate on the streamlines close to the diagonal, are overloaded and have to perform flash procedure at more number of points. At any point of simulation, processor 1 and 11 contain minimum number of streamline points where flash calculations are needed and hence consume least amount of CPU time. The scenario will be completely different for a heterogeneous permeability field or irregular well pattern, where streamline paths are dictated by heterogeneities and well locations. Load balancing can be improved by assigning streamlines to nodes on the basis of the multiphase points instead of just the number of streamlines.

Example 2: 2-D Gas Injection (Effect of number of streamlines)

Simulations are conducted with the same example problem as described in the previous example but with different streamline density. Three cases are considered with 200, 300, and 400 streamlines launched from the injector well. Fig. 69a shows the total run time on a single processor for different number of streamlines. An increase in total execution time is observed with an increase in streamline density. By doubling the streamline density, CPU time is almost doubled. Fig. 69b shows the total flash computation time for different number of streamlines. As the number of streamlines is increased from 200 to 400, flash computation time is also doubled. As discussed in the previous sections, the largest computational cost is associated with the flux (flash) calculations, which increases with the number of streamlines.
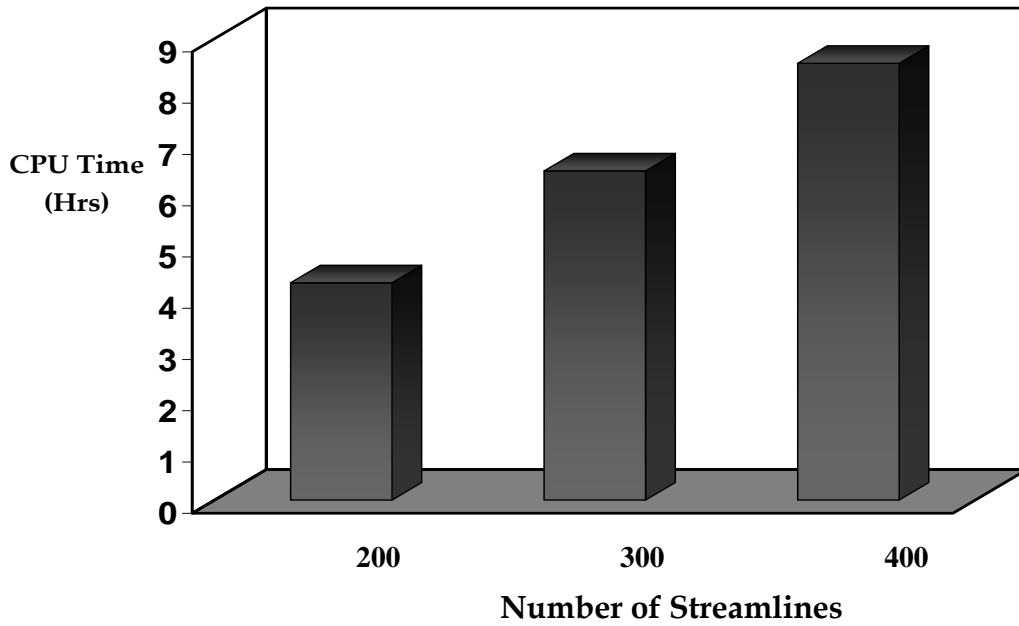
Fig. 69a - Total CPU time on a single processor for different number of streamlines
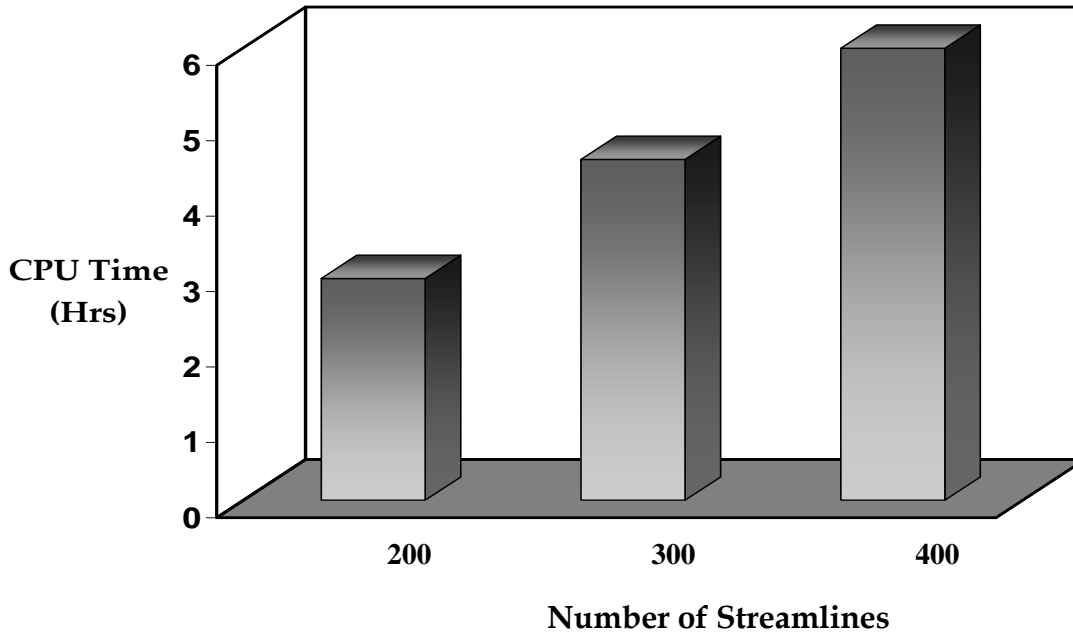
Fig. 69b - Flash calculation time on a single processor for different number of streamlines
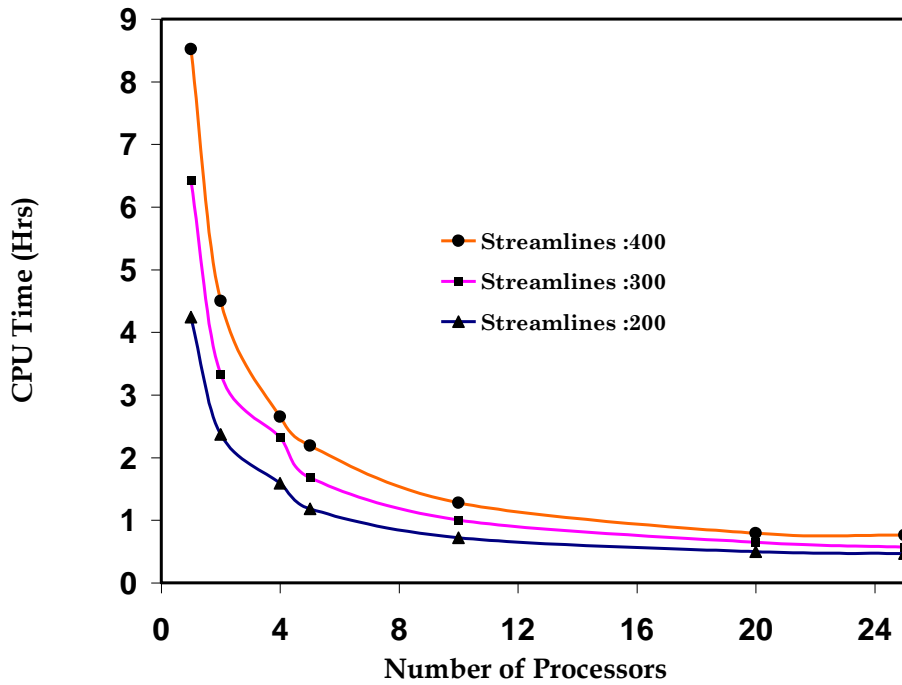
Fig. 70 - Run time vs. number of processors with different number of streamlines
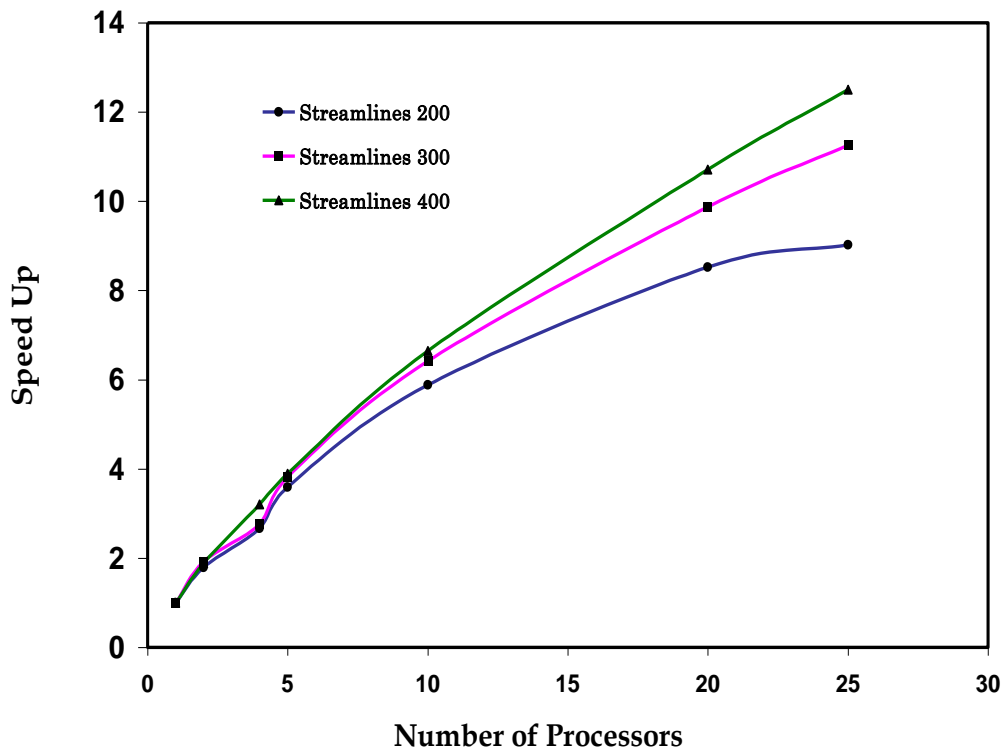
Fig. 71 - Speed up vs. number of processors with different number of streamlines

This simulation model for both the cases is tested on different number of processors and CPU time is recorded. Fig. 70 shows the total CPU elapsed time for different number of processors. As expected, there is a significant reduction in computation time with increase in number of processors. A single processor took approximately 8.5 hrs to run the test case with 400 streamlines. With 25 processors we are able to bring down the computation time to 0.70 hrs. Speed up factors are compared for all the three cases as shown in Fig. 71. Speed-ups of 12.5 and 10.7 is obtained for twenty and twenty five processors for 400 streamlines where as the speed up of 11.3 and 9.9 is recorded for twenty and twenty five processors for 300 streamlines. Though speed up curve deviates from the linear trend on addition of more number of processors but higher speed up factors is observed for the case of 400 streamlines than for 200 streamlines. Again, speed up is limited by the finite difference and communication times. By increasing the problem size we are essentially increasing the ratio of streamline computation time to finite difference and communication time, which in turn enhances the speed up factor.

Example 3: 2-D Gas Injection (X-Z Cross-section – Homogeneous Perm)

This problem uses 3200 grid blocks in a cartesian X-Z plane with 80 grids in the X-direction and 40 grids in the Z-direction. A homogeneous permeability field with k_x=300 md and k_z=15 md is used in the simulation. Both the injector and producer wells are vertical and operated at a constant bottom hole pressure of 1800 psi and 1100 psi, respectively. Both the wells are completed in all 40 layers in z direction. Distance between the wells is 800 ft and thickness of the reservoir is 50 ft. Initial reservoir pressure is 1500 psi with an initial water saturation of 0.2. A mixture of (52 mole %) methane and

123

(48 mole %) propane is injected into the reservoir oil (as described in Table 2) at the reservoir temperature of 140 ^{0}F. Table 12 lists the details of the simulation model used in this case study; the results of the sequential simulation are discussed earlier in Fig. 46.

200 Streamlines

80 * 40 Grid
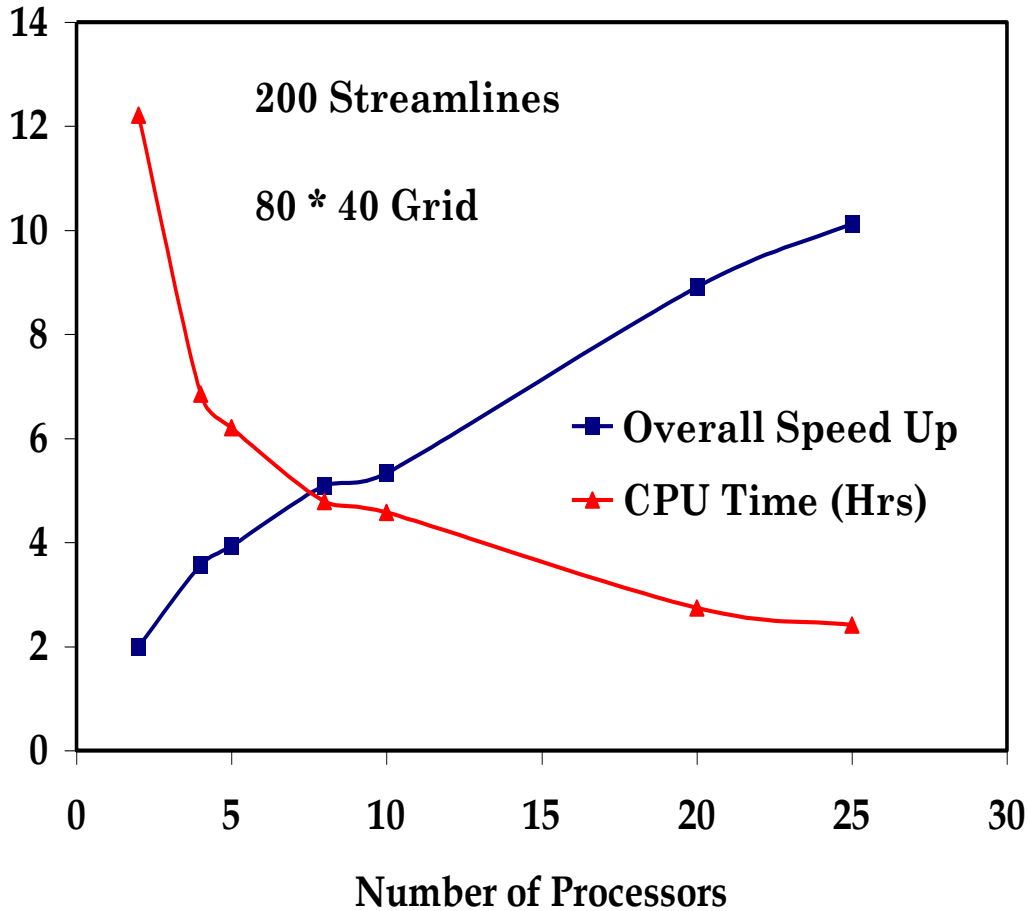
Fig. 72 - Run time and overall speed up vs. number of processors for 2-D
gas injection simulation (X-Z)

Simulation runs are conducted on the same cluster (Atlantis) with 2, 4, 5, 8, 10, 20, and 25 processors. CPU times are recorded for different number of processors as shown in **Fig. 72**. As expected, the execution time is significantly reduced as the number of processors is increased from 2 to 25. Run time is decreased to 2.41 hrs with 25 processors in the work pool from 12.21 hrs when the model was run on only 2 processors.

Two-processor run is used as a base case to estimate the speed up factors (assuming 100 % efficiency from one to two processor run time). Fig. 72 shows the speed up curve for different number of processors. Speed up is almost linear as the number of processors is increased from 2 to 4 but deviates from the linear trend as the number of processors are increased. Speed up of 10.13 is recorded by increasing the number of processors to 25. Again, this decrease in efficiency is due to the increased importance of finite difference calculation and inter-processor communication overhead with the increase in number of processors.

Field-Scale Study

WAG injection was compared with continuous gas injection followed by water on a field scale. A simple 2-D case was constructed first followed by a 3-D, symmetrical quarter five-spot pattern model. In the 2D case, a horizontal permeability field similar to that given in Rathman et al. [2006] was taken as an example for shallow, thin reservoir possibly encountered in North Slope Alaska. A 2D model may only accurately represent one vertical cross-sectional part of this type of reservoir. Some attempt was made here to assess whether the 2D models used here can yield accurate results as compared to the 3D models. CMG's fully compositional simulator, GEM was used in these computations. Displacement of viscous oils by relatively low viscosity solvents, while efficient on a pore scale, is frequently subject to bypassing and channeling effects due to viscous and gravity forces and heterogeneity. A fluid model representing a fairly viscous oil (50cP) was used to show how WAG can improve vertical and horizontal sweep efficiency on a field scale over straight injection of solvent. The fluid model was taken from a typical Alaskan North Slope (West Sak region) oil characterization reported in McGuire et al. [2005].

2D Reservoir Model

Two types of horizontal permeability (k_h) fields were created for the 2D WAG/Continuous Gas study. The first contains a region of high k_h along the bottom of the model from injector to producer and in the second, a high k_h region across the top of the model (see **Fig. 73**). These 2 models will be referred to as model Type A and Type B. The color bars indicate horizontal permeability in the x and y directions in millidarcies. Vertical permeability (k_v) was varied in some cases to study the effect of k_v/k_h. Using k_v/k_h values of 0.05 and 0.5, which are thought to be lower and upper bound averages for typical reservoir conditions, oil recovery and in-situ saturation distributions were studied for continuous gas injection simulations in 2D.

Model Type A
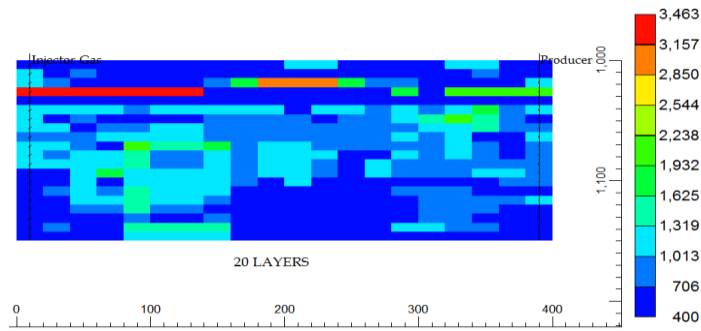
Model Type B
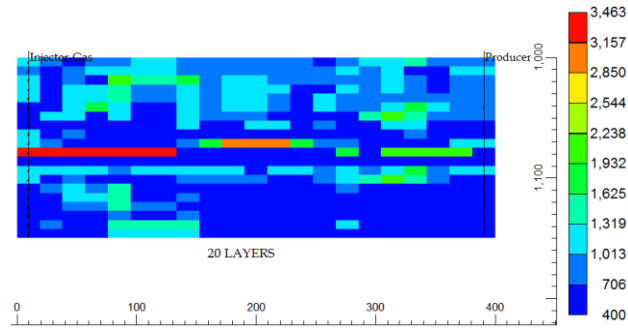
Fig. 73 - Horizontal permeability fields (Type A, B Models)

Following is a description of the fluid models used and model reservoir properties. Each model represents a 400 ft. long, 150 ft. thick prototype heterogeneous reservoir. For simplicity, porosity was assigned a constant value of 18%. Initial pressure was 2000 psi and uniform throughout the grid. A 10% PV (4536 res ft^3 / 9713 res bbl) initial water saturation (S_{wi}) was used to simulate a secondary recovery process. **Table 17** lists these parameters and others. A list of the pseudo-components and initial overall compositions (mole fractions) of the oil and solvent is given in **Table 18**.

Parameter	Value
L ft	400
H ft	150
φ	0.18
PV_{tot} res ft^3 (res bbl)	5.4536E+5 (9.7133E+4)
μ_o cP*	50
μ_s cP*	0.01
$\rho_o{}^*$ lb/ft^3 (kg/m^3)	48.5 (775.3)
$\rho_s{}^*$ lb/ft^3 (kg/m^3)	11.5 (184.2)
S_{wi}	0.1 (most cases)

Table 17 - Model properties

Component	z_{oil}	$z_{solvent}$
CO2	0.0022	0.0155
C1	0.2747	0.7806
C2	0.0066	0.0893
C3	0.0015	0.0588
C4	0.0027	0.0424
C5	0.0019	0.011
C6	0.0029	0.0024
C7-9	0.032	0
C10-24	0.1795	0
C15-18	0.1321	0
C19-23	0.1091	0
C24-27	0.0584	0
C28-33	0.066	0
C34-40	0.0442	0
C40+	0.0859	0

Table 18 - Pseudo-components and initial composition

Constant reservoir volumetric flow rates were imposed at the injection boundary condition and corresponded to 1 PV injection in 5 years (213.3759 res ft^3/D; 53.2236 res bbl/D). Production boundary condition was set to 1,900 psi constant bottom hole pressure (BHP). In the continuous gas simulations, solvent is injected for 2.5 years for a total of 0.50 PV (106.6880 res ft^3 / 26.1118 res bbl) and then water is injected for a period of 17.5 years. In WAG runs, solvent and gas slugs are injected alternately until a total of 0.50 PV solvent is

injected. At that point, water is injected for the remaining time up to 20 years. The base solvent and water slug volumes in WAG cases were 1% PV. In some runs, the volume of the solvent/water slug is varied relative to the 1% PV base volume. For example, in one case the water slug is 1% PV while the solvent slug is 2% PV. This is commonly referred to as the WAG ratio (WR), or the ratio of the water slug volume to the solvent slug volume. A continuous gas run corresponds to a WR=0; a water flood (no solvent) corresponds to a WR=∞. A WR of 1 indicates equal volume slug sizes (1%PV). A WR of 2 indicates a water slug of 2% PV and solvent slug of 1% PV. In this study, WR of 0.5, 1, and 2 were used. In all cases, the solvent slug was injected first.

Continuous Gas Injection followed by Water

Fig. 74 shows in-situ saturation distribution (oil, gas, water) after 0.5 PV solvent injection (total solvent slug) in the Type A model with $k_v/k_h = 0.5$. Solvent flows preferentially along the top of the grid and somewhat into the high permeability streak. The regions where solvent has invaded are more obvious when observing the in-situ oil viscosity (**Fig. 75**). Oil viscosity is greatly reduced, in some places 1-5 cP (top regions of the model). These diagrams show the in-situ oil viscosity for the $k_v/k_h = 0.5$ and 0.05 cases. When the k_v is lower for a given k_h, the less dense solvent does not migrate as quickly to the top of the model, but instead flows through the high permeability streak in the middle of the grid. More oil is contacted when k_v/k_h is 0.05 as opposed to 0.50 and recovery at the end of gas injection is higher (0.14 PV vs. 0.075 PV) (**Fig. 76**). Water injection begins at this point (0.50 PVI) and although water density is higher than that of both oil and solvent, water follows in the path invaded by solvent and reaches the producer well for both cases (**Fig. 77**). Oil production drops off severely after solvent reaches the producer, (see Fig. 76) but begins to increase again some time after water injection begins. Oil production is approximately 0.59

PV when k_v/k_h is 0.05 after 2.0 PV total injection and 0.54 PV when k_v/k_h is 0.50.
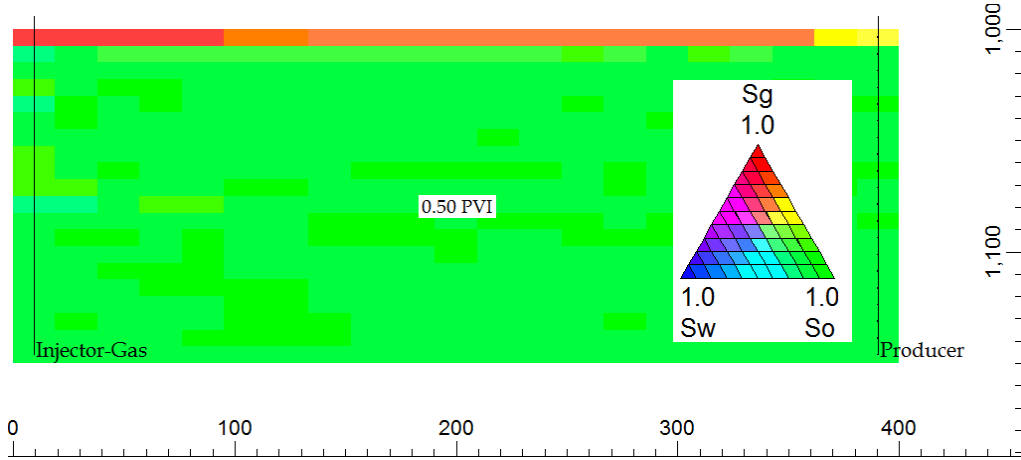
Fig. 74 - In-situ saturation distribution @ ~0.50 PVI (k_v/k_h = 0.50)
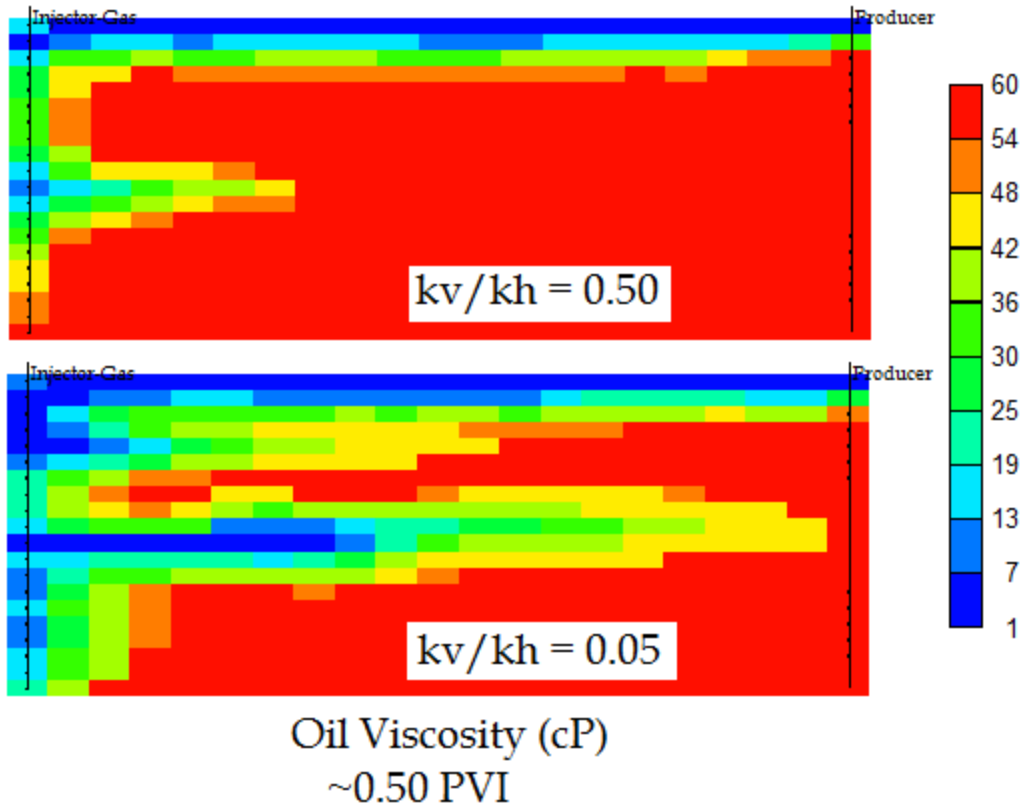
Fig. 75 - In-situ oil viscosity @ ~0.50 PVI ($k_v/k_h = 0.50$)
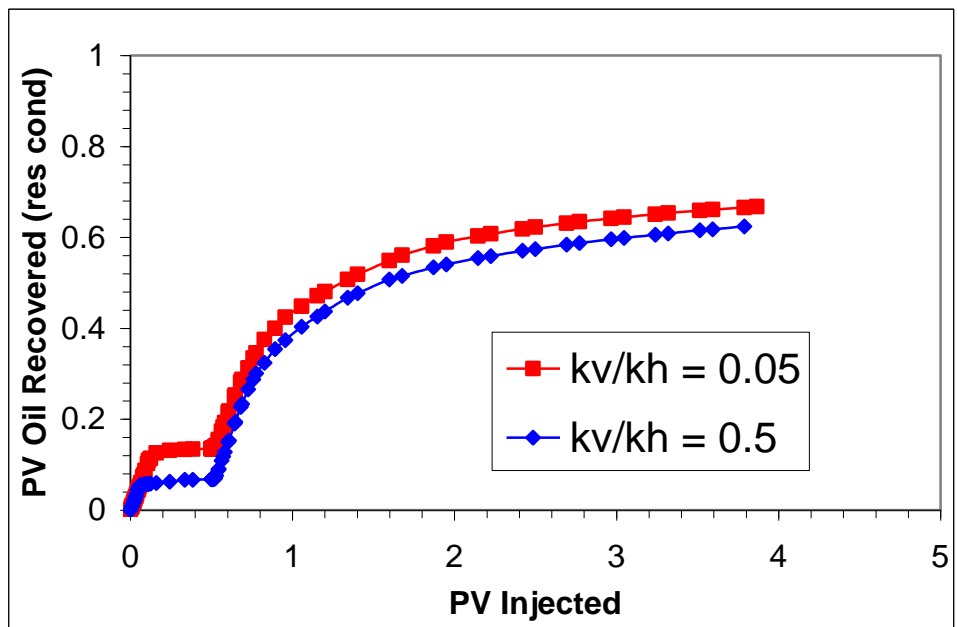
Fig. 76 - Cumulative oil recovery in the field 2D example
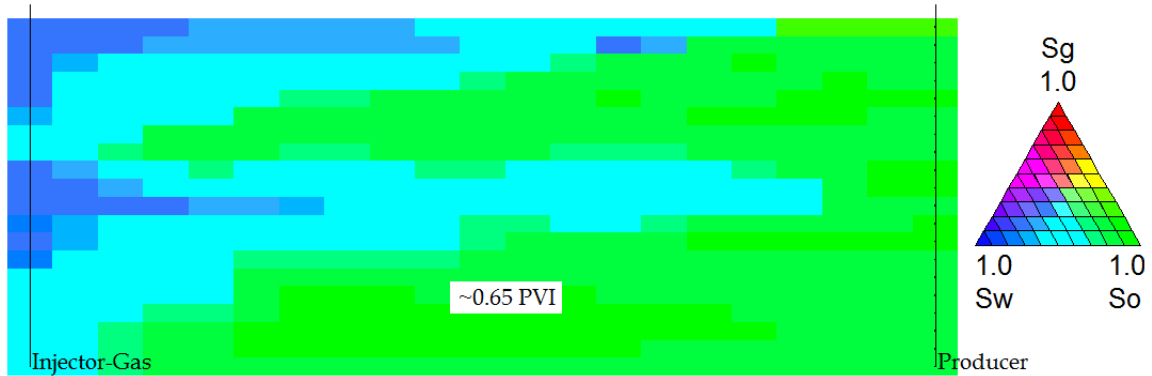
Fig. 77 - In-situ saturation distribution ~0.65 PVI ($k_v/k_h = 0.50$)

Type A vs. Type B Reservoir Models

Continuous gas injection simulations were run using type A and type B models with 20 layers (see Fig. 73). In type A models, a high k_h region is located along the bottom half of the grid, while the high k_h region in type B models is along the top half of the grid. More oil is recovered when the high permeability region is at the bottom half of the grid (**Fig. 78**). This is expected because a high permeability region along the top allows the gas to travel with a higher velocity and reach the producer more quickly, reducing oil production when it does.
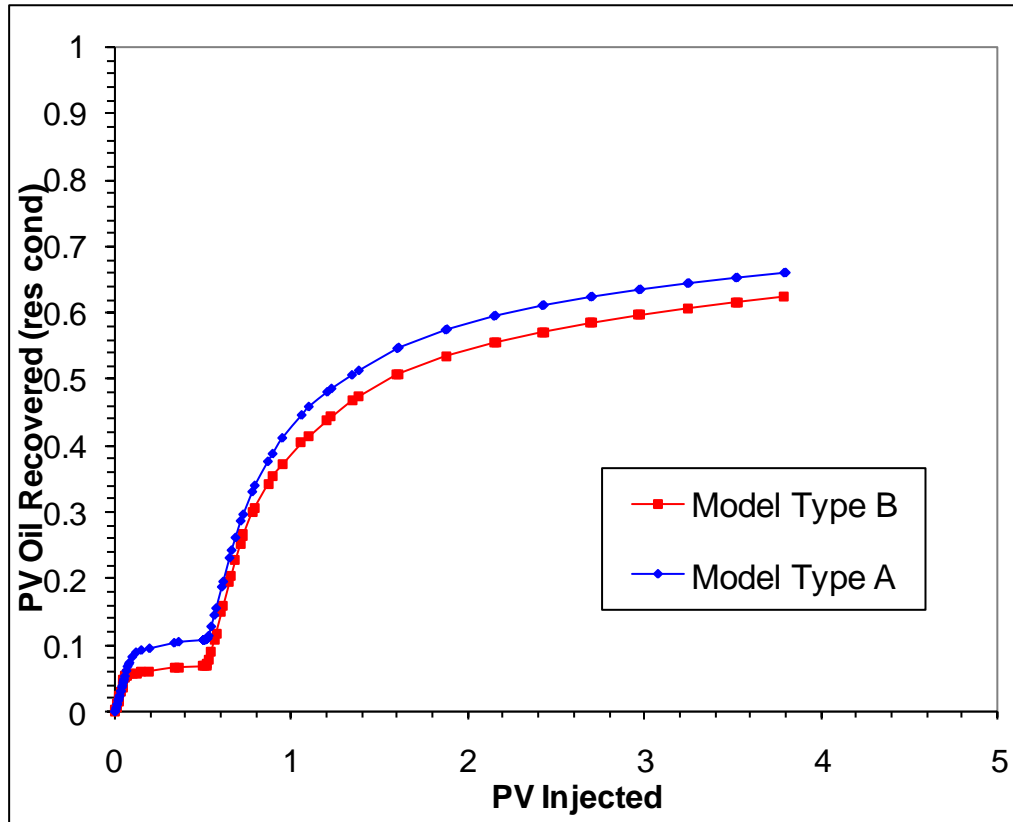
Fig. 78 - Oil Recovery A & B models, $k_v/k_h = 0.5$

Water-alternating gas (WAG) Injection

WAG injection was simulated using the 2D Type B model grid with 20 layers. Oil recovery and in-situ saturation distributions were studied for WAG vs. continuous gas injection cases using the same grid models. **Fig. 79** shows oil recovery in dimensionless pore volumes for continuous gas and WAG injections with varying WAG ratios (1% PV slugs, WR = 0.5, 1 and 2). Oil recovery rates are similar in all cases for some time before oil production in the continuous gas simulation drops off due to solvent break through at the producer. Oil recovery at 0.5 PV throughput for WAG cases are much higher than for the continuous gas injection case. Cumulative oil recovery was approximately 0.624 PV after 4.0 PVI for continuous gas injection, 0.646 PV for WR=0.5 and 0.651 and 0.656 PV for WR=1 and WR=2, respectively (see **Table 19**).
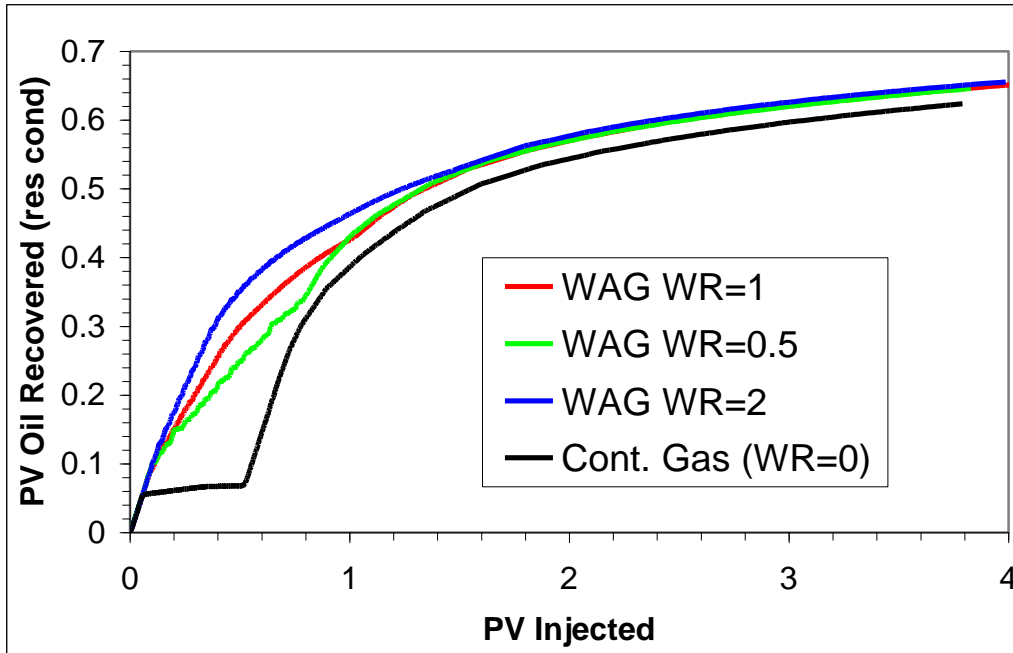
Fig. 79 - Continuous gas vs. WAG oil recovery

Injection Method	PV Oil Recovered @ 2.0 PVI	PV Oil Recovered @ 4.0 PVI
Continuous Gas	54.9%	62.4%
WAG WR=1	57.5%	65.1%
WAG WR=0.5	57.5%	64.6%
WAG WR=2	58.2%	65.6%

Table 19 - Cumulative oil recovery (res cond) WAG, continuous gas 2D runs

3D Reservoir Model

A 3-dimensional reservoir model was developed as an extension of the 2-dimensional model. The 3D model was 20 layers thick and 21x21 grids in the x and y directions, respectively. The length along the diagonal was 400 ft. Reservoir and fluid properties were

135

the same as in the 2D model (see Tables 17 & 18) and so the total PV was 2.18638E+6 res ft^3

(3.8941E+5 res bbl). To construct the horizontal permeability field, k_h values from the 2D

model were varied in the y directions according the following equation.

$$k_x = k_y = k_{h,2D} * (1 + (0.1 * mult))$$

where k_x and k_y are the permeabilities in the x and y-directions, respectively. $k_{h.2D}$ is the

horizontal permeability assigned to each grid in the 20-layer, 2D model and *mult* is a

randomly generated multiplier between -1 and 1.

The grid simulates a quarter of a five spot pattern with a ¼ injector at one corner and

¼ producer at the opposite corner. To minimize grid orientation effects the entire grid was

oriented along the general flow direction, from injector to producer (see **Fig. 80**). Injector

and producer were modeled as point sources in each block along the vertical as in the 2D

model. Injection boundary conditions were set to 1 PV injection in 5 years at a constant

reservoir volumetric rate (1198.01672 res ft^3/D; 213.5789 res bbl/D). Producer boundary

condition was 1,900 psi constant bottom hole pressure.
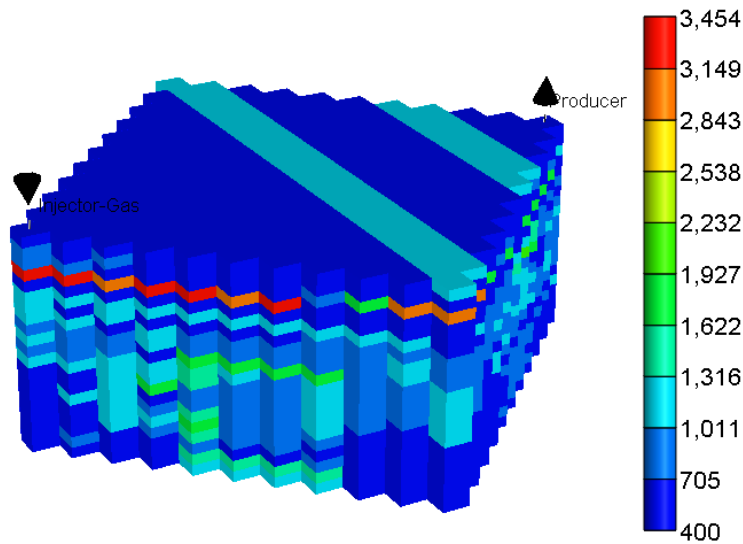
Fig. 80 - 3D simulation grid

Both continuous gas and WAG injection was simulated using the 3D model similarly to the
2D cases described above. The parameter k_v/k_h was set to 0.5 and 0.05 in two continuous gas
runs (**Fig. 81**). Cumulative oil recovery was better when the vertical permeability was lower
($k_v/k_h = 0.05$). Decreasing k_v slows solvent migration to the top of the grid and results in
higher oil recovery. The same trend in cumulative oil recovery with this parameter is
observed in WAG simulations (**Fig. 82**).
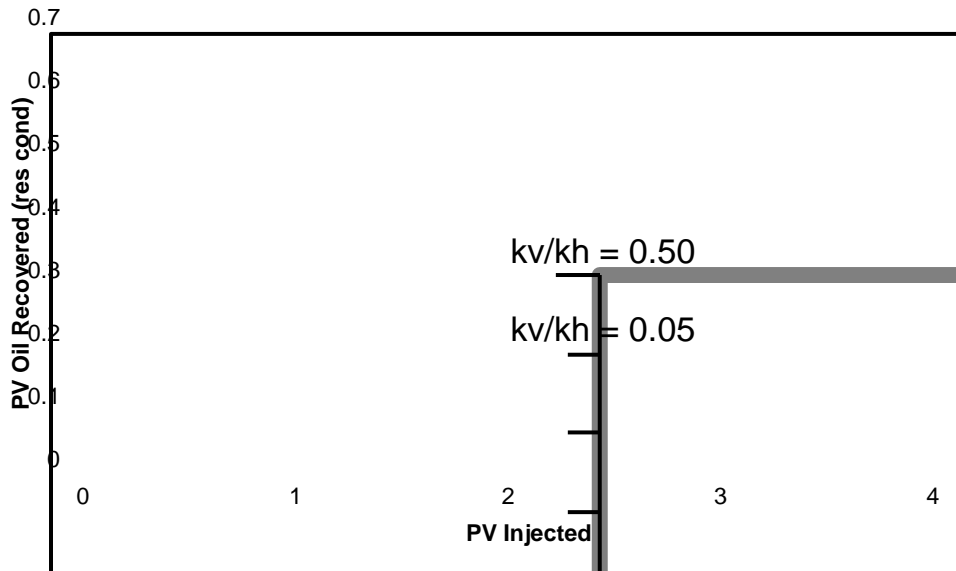
Fig. 81 - 3D continuous gas simulations ($k_v/k_h = 0.05, 0.5$)
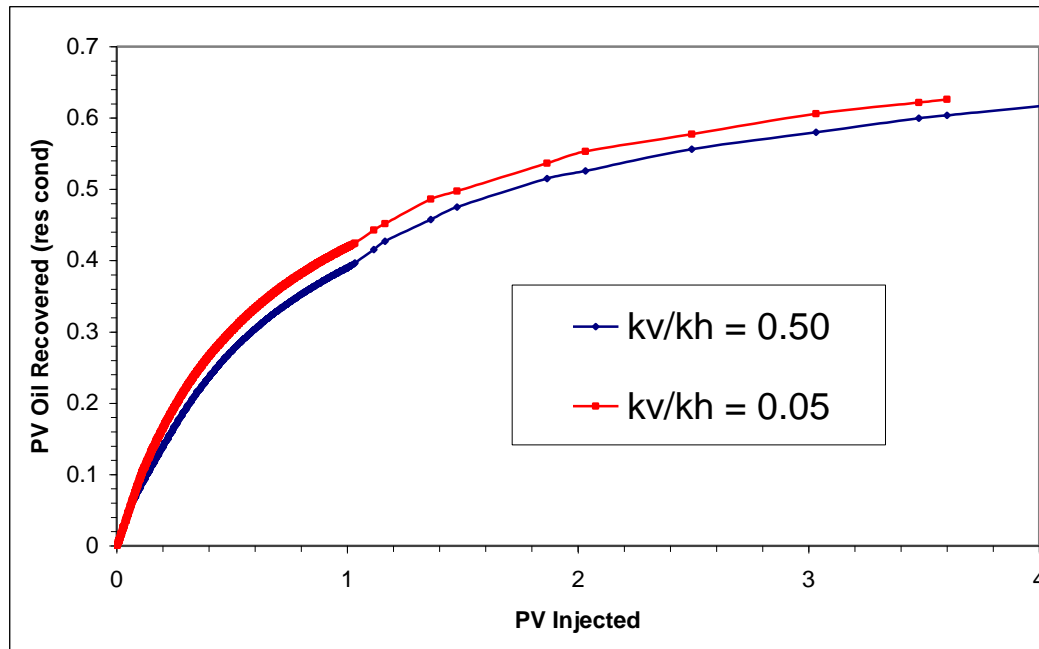
Fig. 82 - Effect of k_v/k_h on recovery in 3D WAG simulations

Cumulative oil recovery for continuous gas injection and WAG runs was very similar for the 2D and 3D models, however the difference in recovery between WAG cases is less pronounced in 3D (**Fig. 83**). At 0.5 PV injection, oil recovery increases with WAG ratio. Approximately 0.586 PV oil was recovered for gas injection followed by water injection at 4 PVI, where as 0.617 PV was recovered at 4.0 PVI for WAG with WR=1 and the other cases (WR = 0.5, 2) predicted similar oil recovery. In-situ oil/gas/water saturations are shown in **Fig. 84**. In **Fig. 84**, an areal (x,y) view of the top of the grid at the end of solvent injection in both the continuous gas (0.50 PVI) and WAG WR=1 (1.0 PVI) cases shows that more solvent remains at the top of the model for continuous gas. This is evidence that WAG helps to limit the rate of solvent migration to the top of the model and helps to reduce oil bypassing.
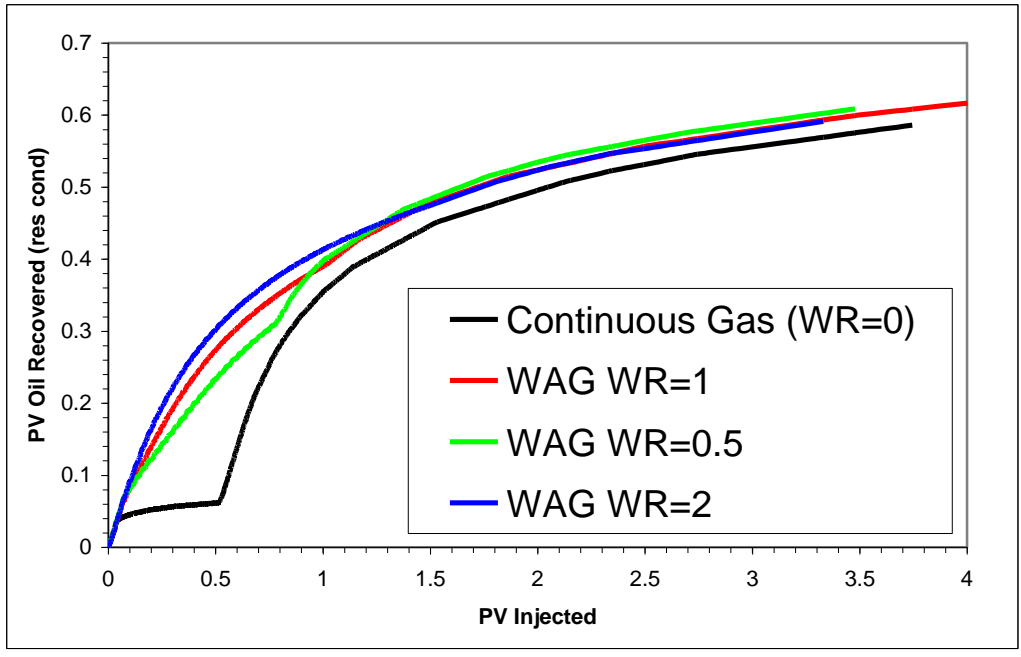
Fig. 83 - Continuous gas vs. WAG injection
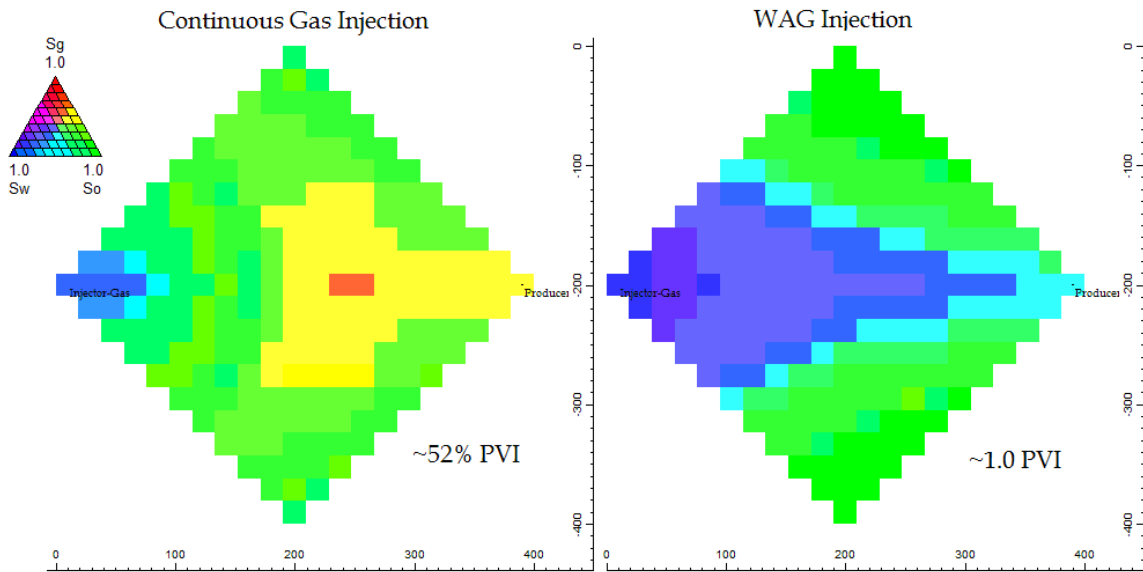
Fig. 84 - In-situ saturation distribution; continuous gas vs. WAG (x-y view)

Conclusions

- Equimolar mixture of NGL and lean gas is multicontact miscible with oil A at 1500 psi. Ethane is a multicontact miscible solvent for oil B at pressures higher than 607 psi. Slimtube oil recovery at 1.2 PV increases with pressure, sharply at ~607 psi and slowly at higher pressures. (Task 1)

- WAG improves the microscopic displacement efficiency (~100%) over continuous gas injection followed by waterflood (~67%) in corefloods. Recovery at 2 PV throughput seems to decreases with WAG ratio. Optimum WAG ratio is 0.5 for this oil and rock. (Task 1)

- During gasflood in cores pressure drop decreases sharply indicating no injectivity problems with this solvent. Pressure drop fluctuates during WAG injections and generally higher than gasfloods. (Task 1)

- Gasflood followed by waterflood improves the oil recovery (~0.55 PV) over just waterflood (~0.48 PV) in the quarter 5-spot cell. Above the MMP, as the pressure increases, the gasflood oil recovery decreases slightly in the pressure range of 4.344 and 9.515 MPa (630 and 1380 psi) for this undersaturated viscous oil. (Task 2)

- WAG improves the oil recovery (~0.68 PV) in the quarter 5-spot over the continuous gas injection followed by waterflood (~0.55 PV). WAG injection slows down gas breakthrough. Estimated sweep improves from 20.5% to 61.5% (for 1:1 WAG). As the WAG ratio increases from 1:2 to 2:1, the sweep efficiency in the 5-spot increases, from 39.6% to 65.9%. (Task 2)

- A decrease in the solvent amount lowers the oil recovery in WAG floods, but significantly higher amount of oil (~0.55 PV) can be recovered with just 0.1 PV solvent injection over just waterflood (~0.48 PV). (Task 2)

- Use of a horizontal production well lowers the oil recovery over the vertical production well during WAG injection phase (from 0.56 PV to 0.46 PV), in this homogeneous 5-spot model. Estimated sweep efficiency decreases from 61.5% to 50.5%. Bypassing is enhanced by the decrease in the distance between injection well and production well tips. (Task 2)

- Estimated gasflood sweep efficiency in the inverse 9-spot model is slightly higher than that in the 5-spot (23.1% vs. 20.5%). (Task 2)

- The oil recovery in the 5-spot due to C2 foam injection depends on surfactant-alternating-gas (SAG) ratio. As SAG ratio increased from 1:10 to 1:1, oil recovery increased. At high SAG ratio, foam behaved like continuous gas injection. Gas stored at the end of these floods increases with SAG ratio. (Task 2)

- In continuous gasflood VAPEX processes, as the distance between the injection well and production well decreases, the oil recovery and rate decreases in continuous gasflood VAPEX processes. (Task 2)

- Continuous gasflood in the VAPEX mode at 200 psi recovers about 0.62 PV of oil in about 2 PV ethane injection. This recovery is higher than waterflood recovery (~0.48 PV) and gas injection followed by water injection (~0.55 PV) in the quarter 5-spot mode. More experiments would be conducted to understand this process. (Task 2)

- Streamline-based simulators can be used for compositional simulations of up to three hydrocarbon-phase systems. 2-D and 3-D simulations of gas injections have been demonstrated. (Task 3)

- To reduce the impact of numerical dispersion, TVD schemes are included in the streamline simulator. Because three-hydrocarbon phase flash calculation is expensive, the number of grids/streamlines needs to be minimized, where use of higher order schemes such as TVD

becomes more important. Use of lower order difference schemes produces more error in miscible displacement problems than in immiscible displacement problems. (Task 3)

- Gravity override is observed for gas injection simulations in vertical (X-Z) cross-sections and 3-D quarter five spot patterns. Breakthrough recovery efficiency increases with the viscous-to-gravity ratio in the range of 1-100. There is little gravity segregation for gravity numbers below 0.02. Above N_g of 0.5, the gravity tongue is well developed. (Task 3)

- Gas injection simulation of the reservoir oil indicates that three hydrocarbon phases exist near the gas-oil displacement front. The second liquid phase is present in many grid blocks under the conditions studied; the gas phase exists in a few grid blocks. (Task 3)

- A detailed analysis of the CPU time distribution clearly indicates that flash calculations along streamline points consume a large part of the total execution time in compositional streamline simulators. A parallel version of a compositional streamline simulator is developed to run large problems on multiple processors. (Task 3)

- The speed up for the streamline calculations alone is almost linear with the number of processors. The overall speed up factor is sub-linear because of the overhead time spent on the finite-difference calculation, inter-processor communication, and non-uniform processor load. (Task 3)

- Field-scale pattern simulations showed that recovery from gas and WAG floods depends on the vertical position of high permeability regions and k_v/k_h ratio. As the location of high permeability region moves down and k_v/k_h ratio decreases, oil recovery increases. There is less gravity override. (Task 3)

- WAG helps in minimizing gravity override over continuous gas injection. The oil recovery at about 0.5 PVI is dramatically higher for WAG floods (about 0.3 PV) than for gas injection

142

(0.07 PV). The oil recovery at 0.5 PVI increases with WAG ratio. At 4 PV total injection, the differences between WAG floods are smaller, but better than gas injection followed by water flood. The recovery from the field model is lower than that from the lab 5-spot model, but the effect of WAG ratio is similar. (Task 3)

List of Graphical Materials

References

1. Moritis, G., "EOR Survey," Oil & Gas J., 39 (April 12, 2004).

2. McGuire, P.L., Redman, R.S., Jhaveri, B.S., Yancey, K.E., and Ning, S.X., "Viscosity Reduction WAG: An Effective EOR Process for North Slope Viscous Oils," SPE 93914, SPE Western Regional meeting, 30 March-1 April, 2005.

3. Dindoruk, B., Johns, R.T., and Orr, F. M., Jr., "Analytical Solution for 4-component Gas Dislacement with Volume Change on Mixing," 3rd European Conf. on Math. Of Oil Recovery, Delft, Holland, June, 1992.

4. Wang, Y. and Peck, D.G., "Analytical Calculation of MMP," SPE 59378, SPE/DOE IOR Symposium, Tulsa, 3-5 April, 2000.

5. Stalkup, F. I., Jr., *Miscible Displacement*, Monograph Series, Volume 8, SPE, Richardson, TX (1983).

6. Zick, A. A., A Combined Condensing/Vaporizing Mechanism in the Displacement of Oil by Enriched Gases," SPE 15493, SPE ATCE, New Orleans, 5-8 Oct., 1986.

7. Campbell, B. T. and Orr Jr., F. M., "Flow Visualization of CO2/Crude Oil Displacements," SPEJ, 25, 665-78 (Oct. 1985).

8. Mohanty, K. K. and Johnson, S. W., "Interpretation of Lab Gasfloods with Multidimensional Compositional Modeling", SPERE, 8, 59-66 (Feb. 1993).

9. Habermann, B., "The Efficiencies of Miscible Displacement as a Function of Mobility Ratio," Trans. AIME, 219, 264 (1960).

10. Mahaffey, J. L., Rutherford, W. M., and Matthews, C. S., "Sweep Efficiency by Miscible Displacement in a Five-Spot," SPEJ, 6, 73-80 (1966).

11. Craig, F. F., Jr., *The Reservoir Engineering Aspects of Waterflooding*, Monograph Series 3, Richardson, TX (1971).

12. Cinar, Y., Jessen, K., Berenblyum, R., Juanes, R., and Orr, F. M., Jr., "An Experimental and Numerical Investigation of Crossflow Effects in Two-Phase Displacements," SPE 90568, SPE ATCE, Houston, TX, 26-29 Sept., 2004.

13. Craig F. F. Jr. et al., A lab study of gravity segregation in Frontal Drives," Trans. AIME, 210, 275-82 (1957).

14. Spivak, A. "Gravity Displacement in Two-Phase Displacement Processes, SPEJ, 14, 619-32 (Dec. 1974).

15. Withjack, E.M. and Akervoll, I., "Computed-Tomography Study of 3D Miscible Displacement Behavior of a Laboratory Five-Spot Model," SPE 18096, SPE ATCE, Houston, TX, 2-5 Oct., 1988.

16. Pozzi, A. L. and Blackwell, R. J., "Design of Laboratory Models for Study of Miscible Displacement," SPEJ, 3, 28-40 (March 1963).

17. Koval, E. J., A Method for Predicting Performance of Unstable Miscible Displacement in Heterogeneous Porous Media," SPEJ, 3, 145-154 (June 1963).

18. Fayers, F.J., Blunt, M.J., Christie, M.A., "Comparisons of Empirical Viscous-Fingering Models and Their Calibration for Heterogeneous Problems" SPERE, 195-203 (1992).

19. Haajizadeh, M., Fayers, F.J. and Cockin, A. P., "Effects of Phase Behavior, Dispersion and Gridding on Sweep Patterns for Nearly Miscible Gas Displacement," SPE 62995, SPE Annual Technical Conference and Exhibition, Dallas, TX, 1-4 October, 2000.

20. Jackson, D. D. and Claridge, E., "Optimum WAG Ratio vs. Rock Wettability in CO_2 Flooding," SPE 14303, SPE ATCE, Las Vegas, 22-25 Sept., 1985.

21. Vives, M. T., Chang, Y. C. & Mohanty, K. K., "Effect of Wettability on Adverse Mobility Immiscible Floods," SPE J., 260-267 (September 1999).

22. Lin, E.C. and Poole, E.S., "Numerical Evaluation of Single Slug, WAG, and Hybrid CO2 Injection Processes, Dollarhide Devonian Unit, Angrews County, TX," SPERE, 6, 415-420 (Nov. 1991).

23. Shan, D. and Rossen, W. R., "Optimal Injection Strategy for Foam IOR," SPE 75180, SPE/DOE Symposium on Improved Oil Recovery, Tulsa, OK, 13-17 April, 2002.

24. Xu, J., Wiascin, A. and Enick, R. M., "Thickening Carbon Dioxide with the Fuoroacrylate-Styrene Copolymer," SPEJ, 85-91 (2003).

25. McGuire, P. L., Redman, R. S., Mathews, W. L., and Carhart, S. R., "Unconventional Miscible EOR Experience at Prudhoe Bay," SPE 39628, SPE/DOE Symposium on Improved Oil Recovery, Tulsa, OK, 19-22 April, 1998.

26. Dao, E.K., Lewis, E., and Mohanty, K.K., "Multicontact Miscible Flooding in High-Pressure Quarter 5-Spot Model," SPE 97198, SPE Annual Technical Conference and Exhibition, Dallas, TX, 9-12 October, 2005.

27. Pollock, D.W.: 1988, Semi analytical computation of path lines for finite difference models, *Ground Water*, **26** (6).

28. Chang, Y.B.: 1990, Development of an equation of state compositional simulator, PhD Thesis, U. of Texas, Austin.

29. Lohrenz, J., Bray, B.G., and Clark, C.R.: 1964, Calculating viscosities of reservoir fluids from their compositions, *J. Petroleum Technology*, 1171-1176.

30. Li, D., Kumar, K., and Mohanty, K.K.: 2003, Compositional simulation of WAG processes for a viscous oil, Paper SPE 84074 presented at SPE Annual Technical Conference and Exhibition, Denver, CO, Oct 5-8.

31. Tchelepi, H.A and Orr, F.M. Jr.: 1994, Interaction of viscous fingering, permeability heterogeneity, and gravity segregation in three dimensions, *SPERE*, **9**, 266-271.

32. Blunt, M.J., Lui, K, and Thiele, M.R.: 1996, A generalized streamline method to predict reservoir flow, *Petroleum Geoscience*, **2**, 259-269.

33. Jessen, K., and Orr, F.M.: 2004, Gravity segregation and compositional streamline simulation, Paper SPE 89448 presented at SPE/DOE Symposium on Improved Oil Recovery, Tulsa, OK, April 17-21.

34. Douglas, J., Peaceman, D. W., and Rachford, H. H., "A Method for Calculating Multi-Dimensional Immiscible Displacement, Petroleum Transactions AIME, 216, 297 (1959).

35. Ning, S.X. and McGuire, P.L., "Improved Oil Recovery in Under-Saturated Reservoirs Using the US-WAG Process," SPE 89353, SPE/DOE 14th Symposium on Improved Oil Recovery, Tulsa, OK, 17-21 April 2004.

National Energy Technology Laboratory

626 Cochrans Mill Road
P.O. Box 10940
Pittsburgh, PA 15236-0940

3610 Collins Ferry Road
P.O. Box 880
Morgantown, WV 26507-0880

One West Third Street, Suite 1400
Tulsa, OK 74103-3519

1450 Queen Avenue SW
Albany, OR 97321-2198

539 Duckering Bldg./UAF Campus
P.O. Box 750172
Fairbanks, AK 99775-0172

Visit the NETL website at:
www.netl.doe.gov

Customer Service:
1-800-553-7681